Generation, characterization and application of infrared few-cycle light pulses

Sytcevich, Ivan

2022

Document Version:
Other version

Generation, characterization and application of infrared few-cycle light pulses

IVAN SYTCEVICH
FACULTY OF ENGINEERING | LUND UNIVERSITY

Generation, characterization and application of infrared few-cycle light pulses

Generation, characterization and application of infrared few-cycle light pulses

by Ivan Sytcevich

LUND
UNIVERSITY

Thesis for the degree of PhD in Physics
Thesis advisors: Dr. Cord L. Arnold, Prof. Anne L'Huillier, Dr. Fabian Langer
Faculty opponent: Dr. Cristian Manzoni

To be presented, with the permission of the Faculty of Engineering, LTH of Lund University, for public criticism in Rydberg lecture hall at the Department of Physics on Friday, the 30th of September 2022 at 09:15.

Organization
LUND UNIVERSITY
Atomic Physics
Box 118
SE–221 00 LUND
Sweden

Document name
DOCTORAL DISSERTATION

Date of disputation
2022-09-30

Sponsoring organization

Author(s)
Ivan Sytcevich

Title and subtitle
Generation, characterization and application of infrared few-cycle light pulses

Abstract

In recent decades, laser systems emitting pulses of light containing only a few electric field oscillations under their envelope have become common in many ultrafast optics laboratories. Owing to unique temporal characteristics and achieving extreme field strengths, these so-called few-cycle pulses have been instrumental in unlocking new regimes of light-matter interaction.

The work presented in this thesis is focused on mastering the techniques to generate and characterize few-optical-cycle light pulses in the near- and short-wave infrared spectral regions. Two systems based on optical parametric chirped pulse amplification (OPCPA) are presented. Derived from the same laser front-end, they both deliver sub-2.5-cycle pulses at high repetition rate (200 kHz) with a stable electric field waveform. The first laser source is a near-infrared OPCPA delivering 6 fs pulses at a carrier of 850 nm which was upgraded during this thesis. The upgrade resulted in a boost of the output pulse energy from 8 µJ to 15 µJ without loss in pulse quality. The second laser source is a few-cycle OPCPA around 2 µm, emitting <16 fs pulses with 13 µJ of pulse energy, which was developed entirely during the thesis. We tested the capabilities of this system by driving high-order harmonic generation (HHG) in argon gas.

As a promising alternative route for few-cycle pulses, nonlinear pulse post-compression based on multipass cells (MPCs) was investigated. It is an efficient way of reducing the pulse duration of high-power Ytterbium (Yb) lasers. In this thesis, two MPC-based compression experiments are presented. Firstly, 1.2 ps pulses from a mJ-level Yb amplifier were compressed to 13 fs with two consecutive gas-filled MPCs. Secondly, the output of another Yb amplifier was compressed from 300 to 31 fs using a bulk MPC while preserving high beam quality.

Successful development of such systems is impossible without careful characterization of the output pulses. Throughout the thesis, we relied on the extensive use of the dispersion scan (d-scan) pulse characterization technique. We demonstrate the powerful capabilities and versatility of the second-harmonic d-scan by measuring pulses of different durations and central wavelengths in scanning and single-shot configurations.

Lastly, the few-cycle light pulses were applied to two-color photoionization experiments and the study of lightwave-driven currents in semiconductors at high repetition rates.

Key words
Few-cycle pulses, pulse characterization, optical parametric amplification.

Classification system and/or index terms (if any)

Supplementary bibliographical information

Language
English

ISSN and key title
0281-2762

ISBN
978-91-8039-315-7 (print)
978-91-8039-314-0 (pdf)

Recipient's notes

Number of pages
180

Price

Security classification

Signature  Date 2022-08-22

Generation, characterization and application of infrared few-cycle light pulses

by Ivan Sytcevich

LUND
UNIVERSITY

A doctoral thesis at a university in Sweden takes either the form of a single, cohesive research study (monograph) or a summary of research papers (compilation thesis), which the doctoral student has written alone or together with one or several other author(s).

In the latter case the thesis consists of two parts. An introductory text puts the research work into context and summarizes the main points of the papers. Then, the research publications themselves are reproduced, together with a description of the individual contributions of the authors. The research papers may either have been already published or are manuscripts at various stages (in press, submitted, or in draft).

Cover illustration front: HHG dispersion scan in argon driven by the short-wave infrared light source.

Cover illustration back: Various glass wedges used for dispersion scan measurements.

Funding information: The thesis work was financially supported by the Swedish Research Council, the European Research Council, infrastructure support by LTH, Crafoord Foundation, and the Knut and Alice Wallenberg Foundation.

Faculty of Engineering, LTH, Atomic Physics

ISBN: 978-91-8039-315-7 (print)
ISBN: 978-91-8039-314-0 (pdf)
ISSN: 0281-2762

Printed in Sweden by Media-Tryck, Lund University, Lund 2022

Abstract

In recent decades, laser systems emitting pulses of light containing only a few electric field oscillations under their envelope have become common in many ultrafast optics laboratories. Owing to unique temporal characteristics and achieving extreme field strengths, these so-called few-cycle pulses have been instrumental in unlocking new regimes of light-matter interaction.

The work presented in this thesis is focused on mastering the techniques to generate and characterize few-optical-cycle light pulses in the near- and short-wave infrared spectral regions. Two systems based on optical parametric chirped pulse amplification (OPCPA) are presented. Derived from the same laser front-end, they both deliver sub-2.5-cycle pulses at high repetition rate (200 kHz) with a stable electric field waveform. The first laser source is a near-infrared OPCPA delivering 6 fs pulses at a carrier of 850 nm which was upgraded during this thesis. The upgrade resulted in a boost of the output pulse energy from 8 µJ to 15 µJ without loss in pulse quality. The second laser source is a few-cycle OPCPA around 2 µm, emitting <16 fs pulses with 13 µJ of pulse energy, which was developed entirely during the thesis. We tested the capabilities of this system by driving high-order harmonic generation (HHG) in argon gas.

As a promising alternative route for few-cycle pulses, nonlinear pulse post-compression based on multipass cells (MPCs) was investigated. It is an efficient way of reducing the pulse duration of high-power Ytterbium (Yb) lasers. In this thesis, two MPC-based compression experiments are presented. Firstly, 1.2 ps pulses from a mJ-level Yb amplifier were compressed to 13 fs with two consecutive gas-filled MPCs. Secondly, the output of another Yb amplifier was compressed from 300 to 31 fs using a bulk MPC while preserving high beam quality.

Successful development of such systems is impossible without careful characterization of the output pulses. Throughout the thesis, we relied on the extensive use of the dispersion scan (d-scan) pulse characterization technique. We demonstrate the powerful capabilities and versatility of the second-harmonic d-scan by measuring pulses of different durations and central wavelengths in scanning and single-shot configurations.

Lastly, the few-cycle light pulses were applied to two-color photoionization experiments and the study of lightwave-driven currents in semiconductors at high repetition rates.

Popular Science Summary

"What comes to your mind when you hear the word laser?" When I started writing my thesis, I asked this question to several of my non-science friends and relatives. "Isn't it what they use when they scan your stuff in the grocery store?"; "For me it is the laser cutter, I really want the laser cutter". One of the younger participants of my survey excitedly exclaimed: "Laser swords from Star Wars!". Lasers have become truly integral parts of our everyday life, and it is hard to imagine our world without them. Nowadays we can make big lasers, small lasers, high power lasers, low power lasers, lasers that shoot continuously, and the ones that shoot in pulses (see Figure 1).

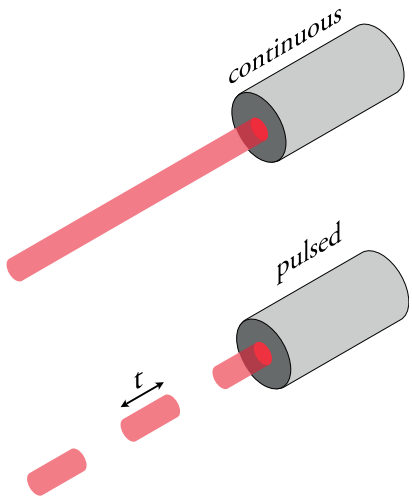

Figure 1: Two modes of laser operation, continuous beam (top) and the pulsed beam (bottom) with the pulse duration t.

Actually, the first laser ever built was pulsed and emitted a series of flashes with a deep red color. Since then, the scientific community has been captivated with the idea of making such lasers that shoot the shortest pulses in time (the smallest possible t in my drawing) and, in my opinion, were quite successful: the pulse of light is now one of the shortest events ever created by humanity. But *what* exactly is a short pulse, *how* do you make it short and *why* do you want to make it short?

The answer to the first question is quite subjective. As laser technology developed over the years, the minimum achievable duration of laser pulses went down dramatically. People in the field of ultrafast optics now typically call pulses of light *few-cycle* if their duration is on the order of several femtoseconds (1 femtosecond is a millionth of a billionth of a second, or 10^{-15} s). This is already so short that we have to use the pulse itself in order to determine

if it is 5 or 10 fs long. No electronic device is quick enough to do this!

Secondly, how do you produce such a short pulse? We know, both from physics and mathematics, that any signal which is short in time must have a broad spectrum. What does that mean? In the case of a light pulse it means that it must contain many different colors: when more and more wavelengths are emitted by the laser, the achievable pulse duration gets shorter and shorter. Certain lasers can produce broad spectra directly, while for others, there are methods to artificially broaden the spectrum, and both types of approaches are investigated in this thesis. However, it is not sufficient to only have a broad spectrum. To actually obtain a short pulse, one must manipulate the timing (or delay) between different wavelengths in the laser spectrum. Scientifically speaking, this timing is called a *spectral phase* and measuring this phase is one of the core procedures in the field of ultrafast optics and also at the core of this thesis.

Finally, why do we care about having short pulses? One particularly scientific example is that we can use them to illuminate (just like a camera flash) and study very fast physical processes inside matter, like the motion of atoms in a molecule. The use of femtosecond lasers, for instance, gave the possibility to capture the time evolution of chemical reactions. This led to the creation of a science field called femtochemistry and resulted in the Nobel Prize to Ahmed Zewail in 1999. Since then, scientists managed to look into even faster events, like the ones that happen inside atoms, and record the movement of electrons with even shorter, attosecond pulses (10^{-18} s).

Now, I have all the tools to explain the essence of my work and decipher the bulky title of this thesis. Over the course of this Ph.D., I spent a significant time in the laboratory trying to build and maintain systems that would shoot the shortest pulses possible in the infrared region of the electromagnetic spectrum. This is what I mean by the word *generation*. Next, I needed to know exactly how short these flashes of light were in order to understand what would I have to do to make them even shorter (not an easy task!). This is the *characterization* step. Finally, I wanted to prove that these pulses were powerful tools that can perform many interesting physics experiments. This is the last step, the *application*.

Populärvetenskaplig Sammanfattning

"Vad tänker du på när du hör ordet laser?" När jag började skriva min avhandling så ställde jag den frågan till många av mina vänner och familj utan naturvetenskaplig bakgrund. "Är det inte sånt man använder i matbutiken för att skanna varor?";"För mig är det laserskäraren, jag vill verkligen ha en laserskärare". En av de yngre deltagarna i min undersökning utbrast upphetsat: "Lasersvärd från Star Wars!" Lasern har blivit en verkligt integrerad del av vårt vardagliga liv, och det är svårt att tänka sig världen utan den. Nu för tiden kan vi göra stora lasrar, små lasrar, hög-effekt lasrar, låg-effekt lasrar, laser som lyser kontinuerligt, och sådana som skjuter i pulser (se Fig. 2).

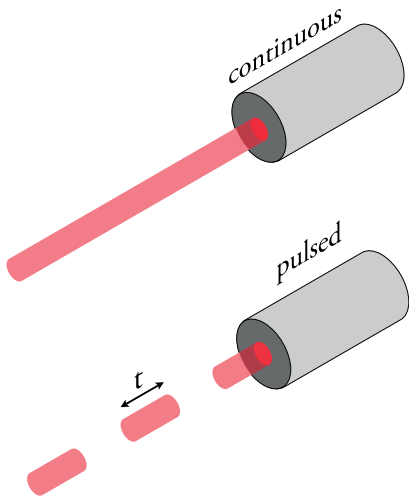

Figure 2: Två typer av laserdrift, en kontinuerlig stråle (topp) och den pulsade strålen (botten) med en pulslängd t.

Faktiskt så var den första lasern som någonsin konstruerades en pulserad laser, och utsöndrade en serie ljusblixtar med en djup röd färg. Sedan dess har det vetenskapliga samfundet varit fascinerat av idén att bygga lasrar som kan skjuta pulser med kortast möjliga varaktighet (minsta möjliga t i min figur) och har, enligt mig, varit framgångsrika: en ljuspuls är nu en av de kortaste tidshändelser som människan skapat. Men exakt *vad* är en kort puls, *hur* kan vi göra den kort, och *varför* vill vi att de ska vara korta?

Det första svaret är subjektivt. Eftersom laserteknologin har utvecklats med tiden, så har den minsta möjliga varaktighet hos en laser puls gått ner dramatiskt. Folk inom fältet ultrasnabb optik kallar nu typiskt ljuspulser *få-cykliga* om deras varaktighet är i storleksordningen femtosekunder, en miljondel av en biljondels sekund (10^{-15} s). Det är redan så kort att vi endast kan använda ljuset självt för att avgöra om den är 5 eller 10 fs lång, ingen

elektronik är tillräckligt snabb för att kunna göra det!

Å andra sidan, hur producerar man en snabb puls? Vi vet, både från fysik och matematik, att en signal som har kort varaktighet i tiden måste ha ett brett energispektrum. Vad betyder det? För en ljuspuls innebär det att den måste innehålla många färger: när fler färger utsöndras från lasern, så blir den möjliga pulslängden kortare och kortare. En del lasrar kan producera ett brett spektrum direkt, medans för andra krävs det metoder för att artificiellt bredda spektrumet, och båda dessa metoder utforskas i avhandlingen. Det är dock inte tillräckligt att bara ha ett brett spektrum. För att faktiskt få en kort puls, så måste man manipulera timingen (eller fördröjningen) mellan olika våglängder i spektrumet. Vetenskapligt talat så kallas denna timing *spektral fas* och att mäta denna fas är en av de grundläggande förfarandena inom fältet ultrasnabb optik, och ämne för denna avhandling.

Slutligen, varför bryr vi oss om att ha korta pulser? Ett specifikt vetenskapligt exempel är att vi kan använda dem för att belysa (precis som med en blixt hos en kamera) och studera väldigt snabba fysikaliska processer inom materia, så som rörelsen hos atomer i en molekyl. Användandet av femtosekundslasrar, till exempel, gjorde det möjligt att fånga tidsevolutionen av kemiska reaktioner. Det ledde till födseln av det vetenskapliga fältet som kallas femtokemi och resulterade i ett Nobel pris år 1999. Sedan dess så har forskare lyckats studera ännu snabbare förlopp, så som de som sker inom en atom, och fånga rörelsen hos elektroner med ännu kortare attosekundspulser (10^{-18} s).

Nu har jag alla de verktyg jag behöver för att beskriva kärnan av mitt arbete och avkoda den otympliga titeln på denna avhandling. Under min tid som doktorand så har jag spenderat mycket tid i labbet med att försöka bygga system som skulle skjuta de kortast möjliga pulserna i den infraröda delen av det elektromagnetiska spektrumet. Det är vad jag menar när jag säger *generation*. Sedan behövde jag veta exakt hur korta dessa ljusblixtar var, för att kunna förstå vad jag behövde göra för att göra dem ännu kortare (inte en enkel uppgift!). Det är *characterization*. Till sist så ville jag visa att de pulser jag jobbat med skulle kunna vara kraftfulla verktyg för att genomföra många intressanta fysikexperiment. Detta är det sista steget, *application*.

List of Publications

This thesis is based on the following publications, referred to by their Roman numerals:

I **Few-cycle short-wave-infrared light source for strong-field experiments at 200 kHz repetition rate**
I. Sytcevich, A.-L. Viotti, C. Guo, J. Vogelsang, F. Langer, A. L'Huillier, and C. L. Arnold
Opt.Express **30**, 27858-27867 (2022)

II **A high-repetition rate attosecond light source for time-resolved coincidence spectroscopy**
S. Mikaelsson, J. Vogelsang, C. Guo, **I. Sytcevich**, A.-L. Viotti, F. Langer, Y.-C. Cheng, S. Nandi, W. Jin, A. Olofsson, R. Weissenbilder, J. Mauritsson, A. L'Huillier, M. Gisselbrecht, and C. L. Arnold
Nanophotonics, **10**, 117-128 (2021)

III **Postcompression of picosecond pulses into the few-cycle regime**
P. Balla, A. Bin Wahid, **I. Sytcevich**, C. Guo, A.-L. Viotti, L. Siletti, A. Cartella, S. Alisauskas, H. Tavakol, U. Grosse-Wortmann, A. Schönberg, M. Seidel, A. Trabattoni, B. Manschwetus, T. Lang, F. Calegari, A. Couairon, A. L'Huillier, C. L. Arnold, I. Hartl, and C. M. Heyl
Opt. Lett, **45**, 2572-2575 (2020)

IV **Multi-gigawatt peak power post-compression in a bulk multi-pass cell at high repetition rate**
A.-K. Raab, M. Seidel, C. Guo, **I. Sytcevich**, G. Arisholm, A. L'Huillier, C. L. Arnold, and A.-L. Viotti
Submitted manuscript

V **Characterizing ultrashort laser pulses with second harmonic dispersion scans**
I. Sytcevich, C. Guo, S. Mikaelsson, J. Vogelsang, A.-L. Viotti, B. Alonso, R. Romero, P. T. Guerreiro, I. J. Sola, A. L'Huillier, H. Crespo, M. Miranda, and C. L. Arnold
J. Opt. Soc. Am. B, **38**, 1546-1555 (2021)

VI **Few-cycle lightwave-driven currents in a semiconductor at high repetition rate**

F. Langer, Y.-P. Liu, Z. Ren, V. Flodgren, C. Guo, J. Vogelsang, S. Mikaelsson, **I. Sytcevich**, J. Ahrens, A. L'Huillier, C. L. Arnold and A. Mikkelsen
Optica, **7**, 4 (2020)

Abbreviations

2/3D	Two/Three Dimensional
APT	Attosecond Pulse Train
ATI	Above-Threshold Ionization
BBO	Beta Barium Borate
BiBO	Bismouth Triborate
CPA	Chirped Pulse Amplification
CEP	Carrier-Envelope Phase
CEO	Carrier-Envelope Offset
DC	Direct Current
DFG	Difference-Frequency Generation
d-scan	dispersion scan
EWP	Electron Wave Packet
FOD	Fourth-Order Dispersion
FROG	Frequency-Resolved Optical Gating
FT	Fourier Transform
FWHM	Full-Width-at-Half-Maximum
GD	Group Delay
GDD	Group Delay Dispersion
GP	Generalized Projections
HCF	Hollow-Core Fiber
HHG	High-order Harmonic Generation
IR	Infrared
MCP	Micro Channel Plate
MIIPS	Multiphoton Intrapulse Interference Phase Scan
MPC	Multipass Cell
NIR	Near-Infrared
NM	Nelder-Mead
NOPA	Noncollinear Optical Parametric Amplification
OAP	Off-axis Parabola
OPA	Optical Parametric Amplification
OPCPA	Optical Parametric Chirped Pulse Amplification/Amplifier
OR	Optical Rectification
PLL	Phase Lock Loop
RABBIT	Reconstruction of Attosecond Beating by Interference of two-photon Transitions
RMS	Root Mean Square
ROC	Radius Of Curvature
SCG	SuperContinuum Generation
SFG	Sum-Frequency Generation
SHG	Second Harmonic Generation
SLM	Spatial Light Modulator
SNR	Signal-to-Noise Ratio

SPIDER	Spectral Phase Interferometry for Direct Electric field Reconstruction
SPM	Self-Phase Modulation
SWIR	Short-Wave Infrared
SXR	Soft X-Ray
THG	Third Harmonic Generation
Ti:Sapphire	Titanium:Sapphire
TOD	Third-Order Dispersion
TSHG	Transverse Second Harmonic Generation
WLG	White-Light Generation
XUV	Extreme Ultraviolet
YAG	Yttrium Aluminium Garnet
Yb	Ytterbium
ZnS	Zinc Sulphide

Contents

Chapter 1

Introduction

1.1 Laser technology and ultrashort light pulses

The ability of lasers to produce spatially and temporally coherent beams of light not only has pushed the boundaries of natural sciences but has significantly changed our everyday life. Optical telecommunication, precision material processing, and semiconductor manufacturing are some of the many industries revolutionized by the progress in laser development. Shortly after the invention of the first Ruby laser by Theodore Maiman [1] which emitted millisecond-long bursts, it was recognized that laser pulses could have very small temporal widths if longitudinal modes of the laser cavity were locked in phase, a technique now known as mode-locking [2, 3]. Over the years, the minimum achievable laser pulse duration decreased dramatically owing to discoveries of new gain media and the development of intricate pulse compression mechanisms. One notable example is the introduction of the titanium-doped sapphire (Ti:Sapphire) crystal as a laser-active material in the 1980's [4]: modern Ti:Sapphire lasers with advanced dispersion compensation can produce near-infrared (NIR) light pulses as short as 5 fs [5]. In this situation, the pulse width is comparable to the temporal period of the electric field oscillation and may contain only a few of these, hence the name "few-cycle pulses"[1]. An example of a few-cycle pulse is sketched in Figure 1.1.

When such a short temporal burst is confined to a small volume in space (i.e., focused), the peak electric field strength E_0 inside this region can take enormous values (with shorter pulses and tighter focusing leading to higher E_0). Even with "very long" pulses from Ruby

[1] The question of what is considered "few" in this context is somewhat philosophical and answering it is beyond the scope of this work. In this thesis, we will call a pulse "few-cycle" if the duration of its intensity profile is less than five optical cycles.

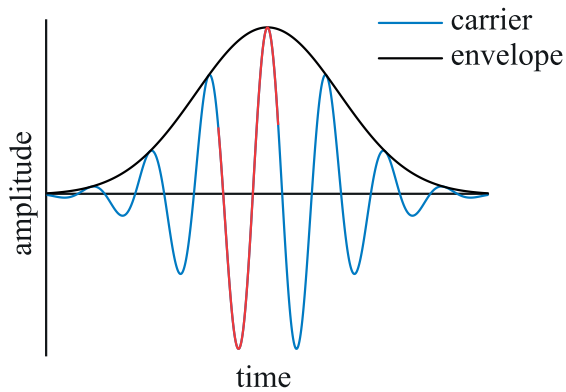

Figure 1.1: A few-cycle pulse, consisting of an oscillating term, called the carrier, modulated by a more slowly-varying term, the envelope. The oscillation cycle is highlighted in red.

laser, the first nonlinear optical effect was demonstrated by Franken *et al.* in 1961: 3 J of energy contained in the pulse were sufficient for the observation of second harmonic generation [6]. Several decades later, energetic nano- and picosecond pulses from Neodymium-ion-doped solid-state lasers paved the way for experimental studies of strong-field laser-matter interaction. Perhaps, one of the most famous examples is high-order harmonic generation (HHG) in noble gases [7, 8]. Focusing the laser into a gas target to intensities of 10^{13} - 10^{15} $\mathrm{W/cm^2}$ leads to the production of a comb of odd-order harmonics of the laser frequency, typically in the extreme ultraviolet (XUV) or soft X-ray (SXR) spectral regions. Furthermore, if the harmonics are phase-locked, the emitted radiation takes the form of a pulse train with individual pulses having durations in the attosecond range [9]. Attosecond pulses produced by HHG have become a unique tool in studies of ultrafast electron dynamics in atoms and molecules and gave birth to the field of attosecond physics [10].

The enabling laser technology behind the majority of compact attosecond light sources is the chirped pulse amplification (CPA) technique [11], awarded the Nobel prize in physics in 2018. A weak ultrashort pulse is stretched in time before amplification, amplified, and later re-compressed close to the original duration. When combined with Ti:Sapphire crystals, CPA allows routine production of high energy (mJ-J per pulse) pulses with tens of femtosecond durations around 800 nm central wavelength, and Ti:Sapphire CPAs have become truly a "workhorse" within attosecond science in most laboratories all over the world. Still, Ti:Sapphire-based amplifiers suffer from several drawbacks. First, the repetition rate (and thus the average power) of such systems is usually limited due to a significant quantum defect and subsequent thermal lensing in the gain medium. Secondly, a short excited state lifetime requires expensive Q-switched pulsed pump lasers and timing electronics. These limitations pushed further the development of a new generation of light sources capable of driving strong-field processes. In the last two decades, Ytterbium (Yb) ion-doped solid-state

and fiber lasers have become increasingly more common. A minor quantum defect (leading to little thermal lensing) and a long storage time (allowing for an inexpensive pumping with powerful diode lasers) are the main ingredients for excellent average power scalability of such sources, and kilowatt-level output powers have been demonstrated with different architectures [12–14]. This makes Yb lasers attractive candidates for pumping broadband optical parametric chirped pulse amplifiers (OPCPAs) [15, 16] or for nonlinear pulse post-compression techniques [17]. This, in turn, opens the route towards the construction of attosecond beamlines that operate at higher repetition rates and photon fluxes.

Another important feature of the HHG process (and many other strong-field phenomena) is that the emission spectrum not only depends on the intensity of the driving pulse but on its central wavelength as well [18]. The maximum photon energy, the harmonic cut-off, scales quadratically with increasing wavelength, allowing for the generation of high-energy photons further in the SXR region. However, the conversion efficiency is reduced [19, 20]. Within the attosecond science community, this constitutes one of the major motivations for the large development effort of high-power ultrashort-pulsed light sources in the short-wave infrared wavelength range (SWIR, $\lambda = 1.3 - 3\,\mu m$) [21–29]. The HHG sources driven by these laser systems not only give access to coherent light in the X-ray "water-window"[2], but increase the overall bandwidth of generated XUV/SXR continua, leading to the production of extremely short attosecond pulses. To give an example, the shortest attosecond pulse to date ($\sim 43\,as$) has been generated from a few-cycle driver centered at $1.8\,\mu m$ [30].

1.2 Scope of this work

The aim of this thesis is to advance the knowledge and gain experience in the design and development of the new generation of ultrashort-pulsed light sources operating in the near- and short-wave infrared wavelength range. For this purpose, two technologies are explored: (1) broadband optical parametric chirped pulse amplification (OPCPA) and (2) nonlinear pulse post-compression based on self-phase modulation in a multipass cell (MPC).

The main project of this doctoral thesis is focused on developing a high repetition rate OPCPA with 2 µm central wavelength. This resulted in the construction of a 2-cycle watt-level SWIR light source, capable of driving a variety of strong-field experiments, thus extending the palette of available intense ultrafast laser systems at the Lund High-Power Laser Facility.

In parallel, nonlinear compression using multipass cells (MPCs) is investigated. This technique emerged as one of the most promising ways to temporally compress the pulses with

[2] A particular region of the X-ray spectrum ($\lambda = 2.33 - 4.35\,nm$) that is of large relevance for bio/medical/chemical spectroscopy applications because biologically active ions (Ca, K, Na) can be distinguished from water and nitrogen.

high average power from Ytterbium (Yb) lasers [17]. Large compression factors and high throughput are demonstrated while preserving the spatial quality of the laser beam.

A significant fraction of the thesis work is dedicated to mastering the techniques of ultrashort pulse characterization, which are essential tools for achieving optimal performance of complex laser systems. We focus mainly on the dispersion scan (d-scan) method [31]. We perform systematic d-scan measurements in different pulse duration regimes in the NIR, recording traces with scanning and single-shot geometries. Based on our findings, we discuss this technique's versatility, advantages, and limitations in a review article.

Lastly, several applications of few-cycle pulses are studied. High-order harmonics are generated from a NIR high repetition rate OPCPA system to perform pump-probe coincidence studies in small atomic systems using a reaction microscope as a detector. Further on, we successfully manage to perform HHG using the 2 µm source, producing photon energies extending to 150 eV. We also observe the generation of lightwave currents in a semiconductor driven by the NIR OPCPA output with almost twice as long pulses as reported previously by other groups.

1.3 Thesis outline

The thesis consists of six articles which can approximately be divided into four distinct topics. The first part deals with the generation of few-optical-cycle pulses in the short-wave and near-infrared spectral regions (**Paper I** and **II**, respectively). **Paper I** provides an overview of the development and characterization of the 200 kHz short-wave infrared light source. It gives a brief technical description of the setup, discusses various properties of the output, and showcases its applicability within strong-field science by demonstrating HHG. **Paper II** presents the established high repetition rate attosecond beamline at the Lund Laser Centre based on the output of the NIR OPCPA. It describes the properties of the driving laser and the design of the vacuum line, including the XUV-IR interferometer and the photoelectron spectrometer as the experimental end station. XUV-IR pump-probe interferometry and single-photon double ionization experiments in helium are demonstrated.

The second part covers various aspects of MPC-based nonlinear post-compression. **Papers III** and **IV** present the work done on compressing the output of Yb laser amplifiers using gas-filled and bulk-based MPCs. **Paper III** presents the results of the compression of picosecond pulses down to four optical cycles via multi-stage gas-filled MPCs. **Paper IV** reports on the development of a space and cost-efficient multipass cell based on thin fused silica plates, achieving high throughput efficiency and a boost of the peak power of an Yb amplifier from 370 MW to 2.5 GW.

The third part focuses on the detailed description of ultrashort pulse characterization based

on the dispersion scan technique. **Paper V** reviews recent developments of the second-harmonic-generation-based d-scan and showcases multi-and single-shot variants of the d-scan, demonstrating its versatility as a convenient and reliable pulse duration measurement technique.

Finally, the fourth part describes applications of few-cycle pulses within nonlinear and strong-field physics. A particular example is the generation of directional currents in the high-bandgap semiconductor gallium nitride at high repetition rate, presented in **Paper VI**.

This thesis is structured as follows: Chapter 2 introduces basic principles of ultrafast and nonlinear optics, required to understand engineering and scientific concepts behind few-cycle OPCPAs and post-compression techniques. Chapter 3 focuses on the methods of pulse characterization, with particular emphasis on the d-scan. Chapter 4 provides a detailed overview of the ultrashort-pulsed light sources developed and characterized during the doctoral studies. Chapter 5 presents various applications of few-cycle pulses explored in this work. Finally, Chapter 6 gives a brief outlook on future developments of ultrafast light sources.

Chapter 2

Fundamentals of ultrafast and nonlinear optics

The operation of complex OPCPA systems, nonlinear post-compression setups, and pulse characterization devices relies on the application and understanding of fundamental physical principles of light propagation and interaction with optical media. This chapter briefly discusses the most important of these principles. First, we introduce core mathematical concepts that help to describe light pulses both in the time and frequency domain and stress the importance of the spectral phase and material dispersion. Later, we cover several important optical nonlinearities, focusing on second-order parametric processes and phase matching conditions in the context of optical parametric amplification. Finally, we provide a brief overview of the optical Kerr effect, a key physical concept behind nonlinear post-compression technology.

2.1 Linear optics of ultrashort pulses

2.1.1 Electromagnetic wave equation

In a classical picture, a pulse of light is a wave packet of electromagnetic radiation, consisting of oscillating electric and magnetic fields and obeying the Maxwell's equations [32]. Its spatio-temporal evolution is described by a wave equation, which in the case of a non-magnetic dielectric medium takes the following form:

$$\nabla^2 E - \mu_0 \epsilon_0 \frac{\partial^2 E}{\partial t^2} = \mu_0 \frac{\partial^2 P}{\partial t^2}. \tag{2.1}$$

Here, E is the electric field of the pulse (a function of time t and space $\vec{r}$), and μ_0 and ϵ_0 are vacuum magnetic permeability and electric permittivity, respectively[1]. The term on the right-hand side of Eq. 2.1 describes a macroscopic response of the optical medium to an incoming electric field. As the wave propagates in the material, the electrons are displaced by the Lorentz force, forming oscillating dipoles. The quantity $P = P(E)$ is the polarization density, the sum of microscopic dipole moments induced by an electric field over a unit volume. If the amplitude of the electric field is small, the polarization density responds linearly to E:

$$P = \epsilon_0 \chi^{(1)} E. \tag{2.2}$$

The quantity $\chi^{(1)}$ is the linear electric susceptibility of the medium. Equation 2.1 can then be simplified in the following way:

$$\nabla^2 E - \frac{n^2}{c^2} \frac{\partial^2 E}{\partial t^2} = 0, \tag{2.3}$$

where $c = 1/\sqrt{\epsilon_0 \mu_0}$ is the speed of light in vacuum, and $n = \sqrt{1 + \chi^{(1)}}$ is the refractive index of the optical medium. The refractive index is generally a complex quantity that depends on the light frequency ω,

$$n(\omega) = n'(\omega) + i n''(\omega). \tag{2.4}$$

In physical terms, real and complex parts of $n(\omega)$ are responsible for the effects of dispersion and absorption of light, respectively. In this thesis, we will focus on the case of weakly absorbing media, for which n can be approximated by $n'(\omega)$ only. The frequency dependence of the refractive index has a fundamental influence on the parameters of an ultrashort pulse during its propagation in optical media, as will be demonstrated below.

2.1.2 Complex electric field and spectral phase

The solution to Eqs. 2.1 and 2.3 is a wave traveling in the direction of the wave vector $\vec{k}$:

$$E(\vec{r}, t) = A(\vec{r}, t) \exp[i(\omega_0 t - \vec{k}\vec{r})], \tag{2.5}$$

[1]Both E and P are, of course, vector fields. However, in the following, we omit the vectorial nature of these quantities for simplicity.

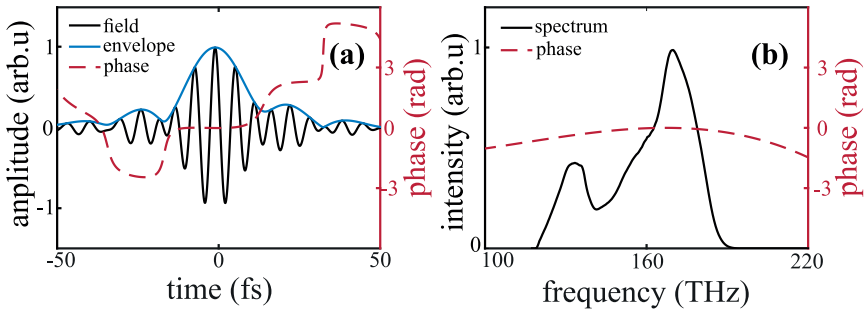

Figure 2.1: Time (a) and frequency (b) representation of an ultrashort pulse.

where $A(\vec{r},t)$ is the complex envelope. For the sake of simplicity, in the following, we will omit the dependence of E on the spatial coordinate $\vec{r}$. In the time domain, the electric field of a light pulse can be written as the product of an oscillating term at the carrier frequency ω_0 and its complex envelope [Figure 2.1(a)]:

$$E(t) = A(t)\exp\left(i\omega_0 t\right) = |E(t)|\exp\left[i(\omega_0 t - \varphi(t))\right], \tag{2.6}$$

with $\varphi(t)$ being the phase of $A(t)$. The temporal phase $\varphi(t)$ determines the instantaneous frequency of the pulse:

$$\omega(t) = \omega_0 - \frac{d\varphi}{dt}. \tag{2.7}$$

As with any time-varying signal, $E(t)$ has its counterpart in the frequency domain and the two are connected via Fourier Transform (FT):

$$\tilde{E}(\omega) = \int_{-\infty}^{\infty} E(t)\exp\left(-i\omega t\right)dt. \tag{2.8}$$

Consequently, in the frequency domain, a pulse is described by its spectral amplitude $|\tilde{E}(\omega)|$ and spectral phase $\phi(\omega)$ [Figure 2.1(b)]:

$$\tilde{E}(\omega) = |\tilde{E}(\omega)|\exp[i\phi(\omega)]. \tag{2.9}$$

From Eqs. 2.8 and 2.9, we can build an intuitive physical picture: at any point in space, the light pulse is a superposition of monochromatic waves, each with its respective amplitude

and phase. Furthermore, the larger the number of waves (i.e., the broader the spectrum), the shorter is the minimum attainable pulse width. This fundamental concept can be written as a time-bandwidth product:

$$\Delta\tau\Delta\omega = \text{const.} \tag{2.10}$$

Here, $\Delta\tau$ is the pulse duration, and $\Delta\omega$ is the corresponding spectral bandwidth. The constant value on the right-hand side of Eq.2.10 depends on the shape of the pulse and the definition of width. Generation of few-cycle pulses often requires octave-spanning spectra, where the spectral width of the pulse is comparable to its carrier frequency.

In the case of light pulses with femtosecond duration, even the fastest electronic detectors are too slow to precisely measure time-dependent quantities in Eq. 2.6. Therefore, it is usually more straightforward to use the spectral representation instead. For example, the spectral amplitude can be easily obtained by measuring the power spectrum (i.e., $|E(\omega)|^2$) with a simple spectrometer. The spectral phase, however, is not easily accessible and can be measured with various approaches described in the next chapter.

The spectral phase $\phi(\omega)$ is extremely useful when describing light propagation in dispersive media. A standard procedure is to expand the function $\phi(\omega)$ into a Taylor series around the pulse central frequency ω_0:

$$\phi(\omega) = \phi_0 + \underbrace{\frac{d\phi}{d\omega}}_{GD}(\omega-\omega_0) + \underbrace{\frac{1}{2!}\frac{d^2\phi}{d\omega^2}}_{GDD}(\omega-\omega_0)^2 + \underbrace{\frac{1}{3!}\frac{d^3\phi}{d\omega^3}}_{TOD}(\omega-\omega_0)^3 + ... \tag{2.11}$$

with the derivatives evaluated at the point $\omega = \omega_0$. The first two terms in Eq. 2.11 are the absolute phase and the group delay (GD). While they do not influence the shape of the envelope, the absolute phase ϕ_0 is directly related to the carrier-envelope phase (CEP) of the pulse. In the time domain, the CEP represents the phase offset between the peaks of the carrier and the envelope. The CEP gains importance as the pulse duration drops to the few-cycle regime. In Figure 2.2, we show 2-cycle pulses with varying values of the CEP. While the envelope functions (and thus the intensity profiles) are identical from pulse to pulse, the actual electric field waveforms differ substantially. The control and stabilization of the CEP are important in many applications, including frequency combs and strong-field physics. We address the methods of measuring and stabilizing the CEP in chapter 3. The GD is a linear phase corresponding to a simple translation in the time domain.

The quadratic term in Eq. 2.11 is called group delay dispersion (GDD), which introduces a linear change of the instantaneous frequency $\omega(t)$ (Eq. 2.7) with time. As a result, the

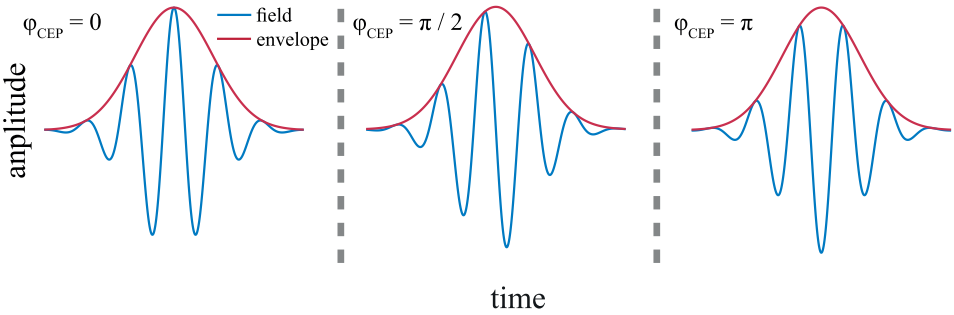

Figure 2.2: A few-cycle pulse with different values of CEP.

pulse (usually) becomes stretched (chirped). The presence of third-order dispersion (TOD) leads to the appearance of pre- or post-pulses [Figure 2.3 (b)] and a steepening of the main pulse profile.

It is particularly advantageous to use the spectral phase expansion as propagation through the majority of transparent components can be evaluated by simply using their GDD and TOD contributions at a specified wavelength. In Table 2.1, as a reference, we provide typical GDD and TOD values per mm of propagation through common optical compounds at 800 (NIR) and 2000 (SWIR) nm wavelengths. In the visible and near-infrared, most materials induce positive GDD. This is referred to as normal dispersion. As the wavelength increases, the GDD decreases, changes sign, and becomes negative, which corresponds to the anomalous dispersion regime.

When the GDD and higher-order dispersion terms are zero, the spectral phase is flat. This corresponds to the shortest pulse duration for a given spectrum, and such pulses are often called Fourier-transform-limited (FL). During the propagation in a medium with a frequency-dependent refractive index, such a pulse will acquire a phase shift:

$$\tilde{E}(z,\omega) = |\tilde{E}(\omega)| \exp\left[i\phi(\omega)\right] \cdot \exp\left[ik_0 n(\omega) z\right], \tag{2.12}$$

where z is the thickness of the material, and $k_0 = \omega/c$ is the vacuum wavenumber. The frequency dependence of $n(\omega)$ causes the initially FL pulse to become chirped, leading to an increase in the pulse duration and a loss of peak power [Figure 2.3(a)].

The effect of dispersion strongly depends on the FL duration (spectral bandwidth) of the pulse. We can define a dispersion length, L_D, as a distance at which a FL pulse gets broadened by a factor of $\sqrt{2}$ when traveling in a dispersive medium [34]. For a Gaussian pulse,

Material	GDD [$\mathrm{fs}^2/\mathrm{mm}$]		TOD [$\mathrm{fs}^3/\mathrm{mm}$]	
	800 nm	2 µm	800 nm	2 µm
CaF_2	28	−21	16	119
BaF_2	38	−24	20	72
Fused Silica	36	−101	28	455
BK7	45	−99	32	460
Sapphire	58	−122	42	530
SF10	156.5	−55.5	102.6	462
ZnS	558	161	377	254
ZnSe	1025	348	686	426

Table 2.1: GDD and TOD values for common materials at 800 and 2 µm central wavelength. Based on refractive index data from [33].

$$z_D\,[\mathrm{mm}] = \frac{\tau_0^2}{(4\log 2)\beta}, \tag{2.13}$$

where τ_0 is the FL pulse duration, and β is the GDD per 1 mm of propagation for a specific material[2]. Clearly, the shorter the FL, the smaller the z_D.

To give an example, consider two Gaussian pulses with central wavelengths of 800 nm and FL durations of 5 and 25 fs [Figure 2.3(b)] propagating through a common BK7 glass ($\beta \sim 50\,\mathrm{fs}^2/\mathrm{mm}$). For the 5 fs pulse (top row), the dispersion length is about 0.18 mm, and going through a 1 mm of BK7 will broaden the pulse almost by a factor of 6. For the 25 fs (bottom row), z_D is 25 times longer (4.5 mm), and the same 1 mm of BK7 will result in minor broadening of less than 1 fs.

In the case of few-cycle pulses, managing high-order dispersion is also critical: introducing $1000\,\mathrm{fs}^3$ of TOD to the 5 fs pulse in Figure 2.3(b) will result in a long tail of sub-pulses taking away a significant portion of energy from the main peak. On the other hand, for the many-cycle, 25 fs pulse the effect is negligible and the pulse envelope is largely left unchanged.

In almost any ultrafast laser system, it is crucial to have control over the spectral phase and manipulate dispersion in a predictable way. For example, in a CPA laser, dispersion is applied that stretches and compresses the pulse in time before and after the amplifica-

[2]Very often referred to as group velocity dispersion or GVD.

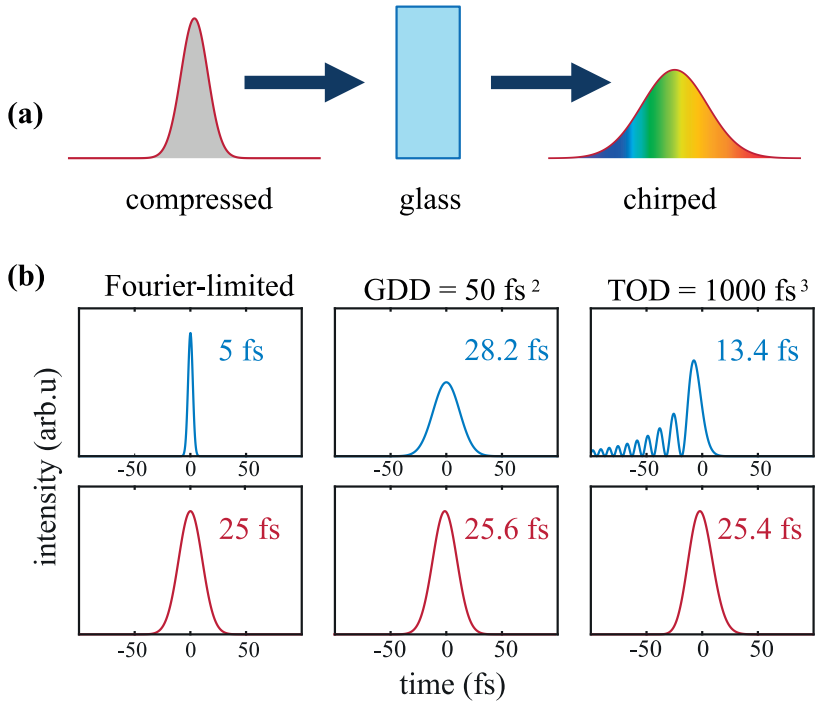

Figure 2.3: (a) A pulse propagating through a dispersive material becomes stretched in time, and the peak power decreases. (b) The effect of second and third-order dispersion on a few-cycle (top row) and multi-cycle (bottom row) pulses, respectively. In the case of a few-cycle pulse, the loss in peak power is not to scale.

tion process. Such operations are usually performed by optical arrangements commonly referred to as pulse stretchers (compressors). The difference in sensitivity to dispersion for pulses of different durations results in a large diversity of compression methods. When dealing with relatively long pulses (with durations from tens of femtoseconds and above), pairs of diffraction gratings or prisms are commonly used [Figures 2.4(a) and 2.4(b), respectively]. Angular dispersion spatially separates different frequency components of the spectrum and makes them propagate with different optical path lengths, thus introducing a frequency-dependent time delay. After the grating/prism pair, a retro-reflecting mirror is usually employed to send the beam back at a slightly different height for recombination at the compressor output. The amount of GDD that is introduced can be tuned by adjusting the distance between the gratings/prisms. The use of diffraction gratings for pulse compression was first proposed in 1969 [35] and grating compressors/stretchers are still widely used in CPA systems due to large amounts of achievable dispersion, albeit at the cost of lim-

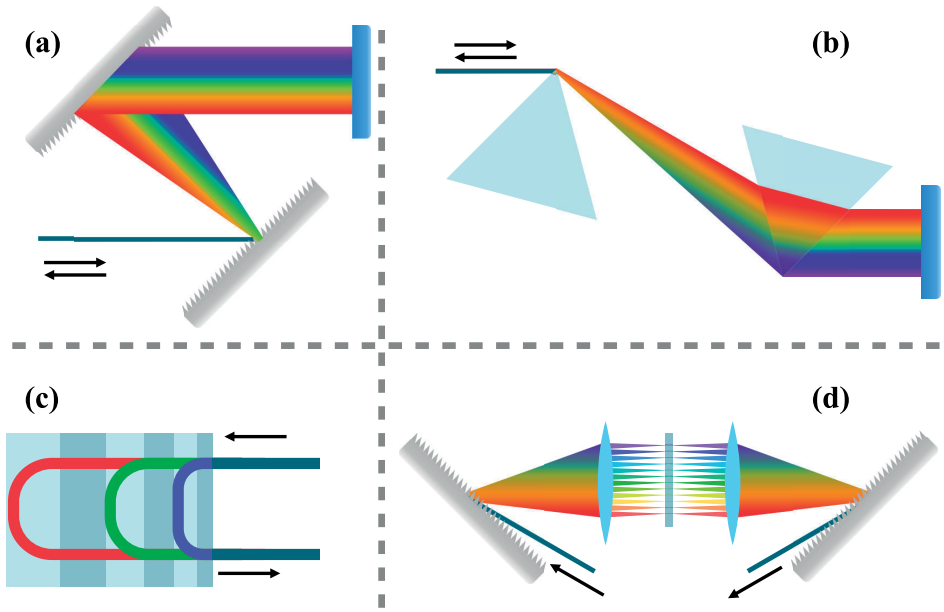

Figure 2.4: Pulse compression configurations. (a) Diffraction grating compressor. (b) Prism compressor. (c) Chirped mirror. (d) Pulse shaper.

ited diffraction efficiency. On the contrary, prism compressors are generally less dispersive but offer advantages such as significantly reduced losses, when used in Brewster configuration [36], and the ability to introduce negative TOD [37], which is impossible with grating compressors[3].

In the domain of broadband few-cycle pulses, however, it is more common to use special chirped mirrors in combination with simple material propagation. A specifically designed dielectric coating with multiple layers of varying thickness forces different frequency components to reflect at different depths inside the mirror [Figure 2.4(c)]. The use of such mirrors offers several advantages. First, it is possible to design the phase that is applied to the pulse upon reflection, which for example offers possibilities to correct for high-order dispersion. Furthermore, chirped mirrors are highly reflective, allowing for extremely high overall compressor throughput. Finally, the alignment of chirped mirror compressors is usually a much less challenging task than that of grating or prism pairs.

It is possible to arbitrarily manipulate the spectral phase of the light pulse by implementing a pulse shaper, and one example of such a device is shown in Figure 2.4(d). The light is split by the grating and different frequency components are imaged with a focusing element on to a

[3]For expressions for the GDD/TOD introduced by material, grating and prism compressors, see e.g. [38].

phase-modulating array, usually a spatial light modulator (SLM). By adjusting the voltage of each pixel on the SLM, the phase of each wavelength can be manipulated, allowing to imprint arbitrary phase curves to the spectrum. The disadvantages are usually a small throughput and a bulky optical arrangement.

The light sources presented in this thesis rely on every compressor type presented above, with the exception of a prism pair. In **Papers I**, **II**, and **IV** transmission gratings are used to compress the ytterbium fiber CPA pump laser. The SWIR light source described in **Paper I** relies on the use of carefully designed third-order-phase-compensating chirped mirrors in combination with a zinc sulfide wedge pair to compress the output pulse close to its Fourier limit. The NIR OPCPA (**Paper II**) features a *4-f* pulse shaper to precisely tailor the phase of the pulse prior parametric amplification, and additional dispersion can be compensated by chirped mirrors and glass wedges.

2.2 Nonlinear optics

As the electric field amplitude in the laser pulse increases, the relationship between polarization density and incoming radiation becomes nonlinear. The deviation from the linear behaviour (Eq. 2.2) can be described using a power series, expanded around $E = 0$,

$$P = \epsilon_0(\chi^{(1)}E + \chi^{(2)}E^2 + \chi^{(3)}E^3 + ...), \tag{2.14}$$

where $\chi^{(2)}$ and $\chi^{(3)}$ are second- and third-order electric susceptibilities, respectively. With increasing E, the second and third terms in Eq. 2.14 gain significance, and the right hand side of wave equation (Eq. 2.1) acts as a source term for a number of phenomena ranging from e.g., sum-frequency generation and optical parametric amplification to two-photon absorption and coherent anti-Stokes Raman scattering.

2.2.1 Three-wave mixing. Phase matching

The $\chi^{(2)}$ nonlinearity is usually present in materials lacking inversion symmetry, such as anisotropic crystals. Some examples of $\chi^{(2)}$ effects are shown in Figure 2.5.

A simple intuitive picture can be obtained by considering the case of two laser fields with frequencies ω_1 and ω_2 impinging on a $\chi^{(2)}$ nonlinear medium,

$$E(t) = E_1 \exp(i\omega_1 t) + E_2 \exp(i\omega_2 t) + c.c. \tag{2.15}$$

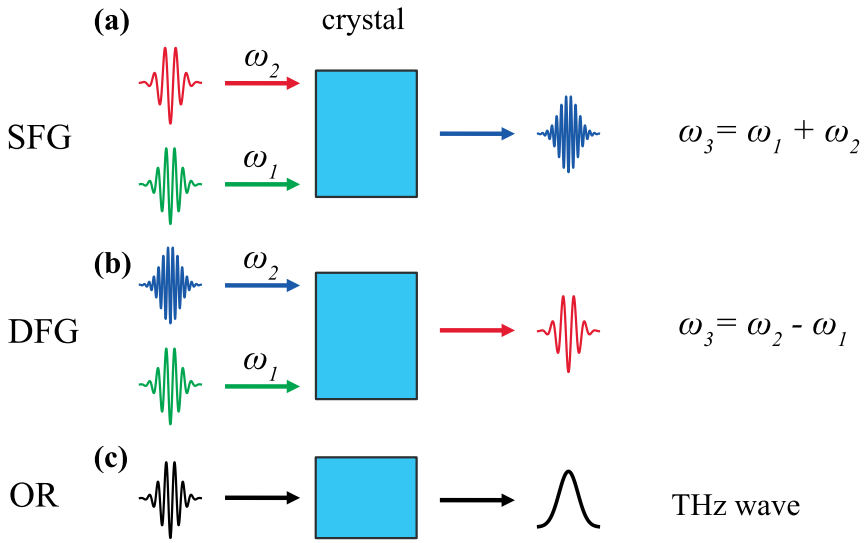

Figure 2.5: Schematic representation of second order processes. (a) SFG - sum frequency generation. (b) DFG - difference frequency generation. (c) OR - optical rectification with a femtosecond pulse.

The second-order polarization is then given by [39]:

$$P^{(2)}(t) = \epsilon_0 \chi^{(2)} \{ \underbrace{E_1^2 \exp[i(2\omega_1)t] + E_2^2 \exp[i(2\omega_2)t]}_{SHG} + \underbrace{2E_1 E_2 \exp[i(\omega_1 + \omega_2)t}_{SFG} + \underbrace{2E_1 E_2^* \exp[i(\omega_1 - \omega_2)t}_{DFG} + c.c \} + \underbrace{2\epsilon_0 \chi^{(2)} \{ E_1 E_1^* + E_2 E_2^* \}}_{OR}. \quad (2.16)$$

The first two terms describe the process of second harmonic generation (SHG) of individual input frequency components, producing light fields that oscillate at $2\omega_1$ and $2\omega_2$, respectively. The SHG can be viewed as a specific case of sum-frequency generation (SFG) [Figure 2.5(a)], which produces a component at frequency $\omega_3 = \omega_1 + \omega_2$. An opposite effect, difference-frequency generation (DFG) [Figure 2.5(b)], creates the third wave at the frequency difference between the two inputs, i.e., $\omega_3 = \omega_2 - \omega_1$. Finally, the last term on the right hand side of Eq. 2.16 is responsible for optical rectification (OR) [Figure 2.5(c)], generation of a static (DC) electric field component within the nonlinear crystal. When such a process is excited by a femtosecond pulse, OR produces a single-cycle electric field perturbation in the shape of the pulse envelope, with a central frequency in the THz spectral range, allowing for the routine production of THz radiation [40].

Coupled-wave equations and parametric gain

In a more general formulation, any second-order nonlinearity is an outcome of a three-wave mixing process, naturally affecting all three participating fields: the waves are said to be coupled, and their interaction can be described by a system of coupled equations [39]. Consider a field consisting of three monochromatic plane waves with frequencies $\omega_3 > \omega_1 > \omega_2$ and amplitudes A_1 - A_3, propagating in the z-direction in a nonlinear crystal:

$$E(t,z) = \sum_{i=1}^{3} A_i(z) \exp[i(w_i t - k_i z)]. \tag{2.17}$$

The coupled-wave equations take the following form:

$$\begin{cases} \dfrac{dA_1}{dz} = i\dfrac{\chi^{(2)}\omega_1^2}{k_1 c^2} A_3 A_2^* \exp[-i\Delta k z], \\ \dfrac{dA_2}{dz} = i\dfrac{\chi^{(2)}\omega_2^2}{k_2 c^2} A_3 A_1^* \exp[-i\Delta k z], \\ \dfrac{dA_3}{dz} = i\dfrac{\chi^{(2)}\omega_3^2}{k_3 c^2} A_1 A_2 \exp[i\Delta k z], \end{cases} \tag{2.18}$$

where,

$$\Delta k = k_3 - k_2 - k_1 = \frac{1}{c}(\omega_1 n_1 + \omega_2 n_2 + \omega_3 n_3). \tag{2.19}$$

Depending on which components are present at the crystal entrance and crystal properties, either sum- or difference-frequency generation can occur. For instance, DFG occurs when the incoming wave with the highest frequency (E_3), often called the pump, transfers its optical energy to the second input field (E_1), the signal, and the generated difference-frequency component (E_2), the idler, with two waves monotonously growing in intensity. As a result, during the propagation in the crystal, the signal beam essentially experiences amplification. When used for such a purpose, this three-wave mixing modality is referred to as optical parametric amplification (OPA).

In order to study the parameters of the signal beam after parametric amplification, it is possible to solve Eqs. 2.18 analytically by making several approximations. Assuming no idler beam at the crystal input surface and negligible pump depletion, the signal intensity ($I_1 \propto |A_1|^2$) as a function of z is given by [41]:

$$I_1(z) = I_1(0)\left[1 + \frac{\Gamma^2}{g^2}\sinh^2(gz)\right], \tag{2.20}$$

where $I_1(0)$ is the initial intensity, Γ is a parametric gain coefficient and g is the small-signal gain,

$$\Gamma^2 = \frac{2d_{\text{eff}}^2 \omega_1 \omega_2 I_3}{n_3 n_2 n_1 \epsilon_0 c^3}, \tag{2.21a}$$

$$g^2 = \Gamma^2 - \left(\frac{\Delta k}{2}\right)^2. \tag{2.21b}$$

Here, I_3 is the intensity of the pump, and d_{eff} is the effective nonlinear coefficient, a parameter closely related to $\chi^{(2)}$ that quantifies the efficiency (strength) of nonlinear interaction. The energy conversion to the signal wave strongly depends on the value of Δk and is optimized when $\Delta k = 0$: the interacting fields are then said to satisfy the *phase matching condition*. Due to material dispersion, this condition, however, cannot be easily fulfilled. The phase mismatch is usually eliminated by either exploiting crystal properties, such as birefringence or temperature dependence of the refractive index, or by engineering the nonlinear medium itself, as is the case of e.g., periodically-poled materials with a position-dependent nonlinearity d_{eff}, a technique known as quasi-phase matching.

Birefringent phase matching in anisotropic materials

Parametric amplifiers, as presented in this work, are based on birefringent phase matching in uniaxial and biaxial nonlinear crystals. Many ultrafast OPAs operate in a non-collinear geometry, as shown in Figure 2.6(a). This often offers several advantages which are discussed below. In the case of a non-collinear OPA (NOPA), Eq. 2.19 becomes vectorial:

$$\vec{\Delta k} = \vec{k_3} - \vec{k_1} - \vec{k_2}. \tag{2.22}$$

Using the notation of Figure 2.6(a), we can decompose Eq. 2.22 into two scalar equations describing two orthogonal components of the wavevector mismatch:

$$\begin{aligned} \Delta k_{\parallel} &= k_3 \cos\alpha - k_1 - k_2 \cos\Omega, \\ \Delta k_{\perp} &= k_3 \sin\alpha - k_2 \sin\Omega, \\ |\Delta k| &= \sqrt{\Delta k_{\parallel}^2 + \Delta k_{\perp}^2}, \end{aligned} \tag{2.23}$$

where α is the angle between the signal and the pump and Ω is the angle between the idler and the signal. The magnitude of the wavevectors k_i (i = 1, 2, 3) in Eq. 2.23 depends on the refractive indices n_i, which for anisotropic materials depend on polarization and propagation direction. Consider the case of propagation inside a biaxial nonlinear crystal [Figure 2.6(b)] with principal refractive indices $n_{x,y,z}$ ($n_x \neq n_y \neq n_z$). For an arbitrary

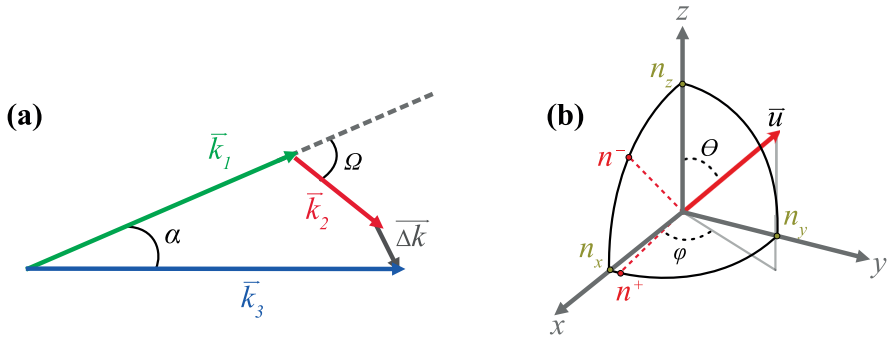

Figure 2.6: (a) Non-collinear phase matching geometry. $\vec{k}_1$ - the signal, $\vec{k}_2$ - the idler, $\vec{k}_3$ - the pump, α - non-collinear angle. (b) A schematic of an index ellipsoid of a biaxial crystal.

direction $\vec{u}$, there are two possible polarization eigenstates[4] with two corresponding refractive indices $n^{\pm}$ ($n^+ > n^-$). Their values can be calculated e.g., using the approach of Yao *et al.* [43]:

$$\begin{aligned} n^{\pm} &= \sqrt{\frac{2}{-B \mp \sqrt{(B^2 - 4C)}}}, \\ B &= -u_x^2(b+c) - u_y^2(a+c) - u_z^2(a+b), \\ C &= -u_x^2 bc + u_y^2 ac + u_z^2 ab, \\ a &= n_x^{-2},\ b = n_y^{-2},\ c = n_z^{-2}, \\ u_x &= \cos\varphi \sin\theta,\ u_y = \sin\varphi \sin\theta,\ u_z = \cos\theta. \end{aligned} \tag{2.24}$$

Here, $u_{x,y,z}$ are the Cartesian components of the propagation vector, expressed in spherical coordinates as a function of angles (θ, φ). The phase-matching calculation involves finding combinations of refractive indices $\{n_1^{\pm}, n_2^{\pm}, n_3^{\pm}\}$ (angles θ and φ) that minimize the value of Δk at a given wavelength. The phase matching is said to be of type I if the signal and idler beams share the same polarization (e.g., $\{n_1^-, n_2^-, n_3^+\}$ or $\{n_1^+, n_2^+, n_3^-\}$) and of type II, if their polarizations are orthogonal (e.g., $\{n_1^+, n_2^-, n_3^+\}$ or $\{n_1^-, n_2^+, n_3^-\}$). It is worth noting, that depending on the choice of a nonlinear crystal, not all interaction types can be phase-matched.

Using Eqs. 2.23 and 2.24, it is possible to calculate the optimum phase matching angles for a selected interaction type in arbitrary propagation direction. However, this calculation can be rather complex. In practice, propagation in the principal planes of a crystal is often

[4]These are the states that do not change their polarization during the propagation in the anisotropic medium, sometimes called the normal modes [42].

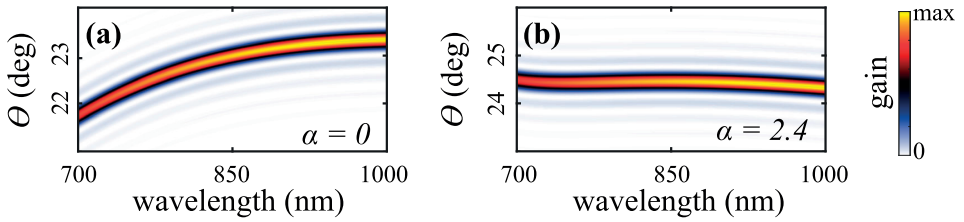

Figure 2.7: Parametric gain of a BBO-based NIR OPA as a function of wavelength and phase-matching angle. (a) Collinear geometry, $\alpha = 0$. (b) Non-collinear geometry, $\alpha = 2.4$.

assumed, where the value of only one angle is varied (either θ or φ, depending on the chosen plane). This situation is then similar to the case of a uniaxial crystal, for which $n_x = n_y \ (\equiv n_o) \neq n_z \ (\equiv n_e)$ are the ordinary and extraordinary refractive indices, respectively, and the angle dependence of the refractive index is conveniently described by a simple ellipse equation:

$$\frac{1}{n^2(\theta)} = \frac{\cos^2\theta}{n_o^2} + \frac{\sin^2\theta}{n_e^2}. \tag{2.25}$$

If the d_{eff} is known[5], plugging the calculated values for the phase mismatch Δk into Eq. 2.21b allows for the estimation of the wavelength-dependent parametric gain [$G = I_1(z)/I_1(0)$] of the amplification process. As an example, in Figure 2.7, we show the gain curve as a function of wavelength and phase matching angle θ for the case of a NIR OPA (700 - 1000 nm signal wavelength) pumped by a 515 nm beam using a 1-mm-thick beta barium borate (BBO) crystal in a type I ($o + o = e$) interaction, for the collinear [Figure 2.7(a)] and non-collinear [Figure 2.7(b)] geometries, respectively. The refractive indices of the signal and the idler beam are evaluated with Sellmeier equations, while Eq. 2.25 is used to calculate the angle-dependent refractive index of the pump.

Evidently, in the collinear case [Figure 2.7(a)], there is a clear change of the optimal phase-match angle θ across the signal spectrum and a broadband phase matching cannot be satisfied. In certain cases, it is possible to increase the amplification bandwidth by using a non-collinear geometry instead. The non-collinear angle adds an additional degree of freedom when searching for an optimum phase matching condition, as well as spatial separation of the beams after the interaction, at the cost of an angularly dispersed idler beam. In our example, adding a non-collinear angle α of approximately $2.4°$ allows to minimize the phase mismatch for every wavelength of the signal at $\theta = 24.5°$ [Figure 2.7(b)], achieving a much broader amplified spectrum.

[5]For the procedure of calculating the d_{eff}, which also depends on θ and ϕ, see e.g., [39].

Passive CEP stabilization

Besides the amplification of weak signal pulses and the generation of broadband infrared continua, the DFG/OPA process can be used to produce idler pulses with a stable shot-to-shot carrier-envelope phase, a technique known as passive CEP stabilization [44]. Akin to the phase and frequency matching conditions, the CEPs of the three waves participating in the DFG/OPA are linked by the following equation:

$$\phi_3 - \phi_1 - \phi_2 - \frac{\pi}{2} = 0, \tag{2.26}$$

where the constant $\pi/2$ phase offset is added during the nonlinear interaction [45]. If the phases of the pump ϕ_3 and the signal ϕ_1 possess similar shot-to-shot CEP fluctuations (i.e., originate from the same source), the resulting phase of the idler beam will be the difference between the two, ϕ_2 = ϕ_3 - ϕ_1 = const., yielding a constant CEP. We use this approach in **Paper I**, where CEP-stable idler pulses are generated in a DFG stage with the two incoming waves derived from the 1030 nm output of an Yb amplifier.

2.2.2 Third-order effects

Third-order nonlinear processes arise from a cubic nonlinearity of the polarization density $P^{(3)}$ = $\epsilon_0\chi^{(3)}E^3$ and present themselves as different modalities of four-wave mixing. Here, we would like to briefly focus on a particular four-wave mixing component of $P^{(3)}$, oscillating at the frequency of the incoming field ω:

$$P^{(3)}(\omega) = 3\epsilon_0\chi^{(3)}(\omega = \omega + \omega - \omega)|E(\omega)|^2E(\omega). \tag{2.27}$$

The nonlinear polarization component described by Eq. 2.27 influences the propagation of the pulse by modifying the refractive index n. The value of n becomes dependent on the light intensity $I(r,t) \propto |E(r,t)|^2$, a phenomenon known as the optical Kerr effect:

$$n(I) = n_0 + n_2I(r,t), \tag{2.28}$$

where n_0 is the "normal" weak-field refractive index, and n_2 is called nonlinear refractive index, proportional to $\chi^{(3)}$. Since the pulse intensity is a function of time and space, this phenomenon leads to self-action effects in both the spatial and temporal (spectral) domains.

The dependence of the refractive index on the spatial intensity profile $I(r)$ results in self-focusing. Since in the majority of common optical materials, the nonlinear coefficient n_2

is positive, the medium acts as a focusing lens, overcoming natural beam divergence due to diffraction if the peak power in the beam is larger than a critical value P_{crit}:

$$P_{\text{crit}} = \frac{\alpha\lambda^2}{4\pi n_0 n_2}, \tag{2.29}$$

where λ is the wavelength and the parameter α depends on the spatial profile of the incoming pulse[6]. Self-focusing plays an important role in the filament propagation of intense laser pulses, where it can be compensated by plasma defocusing in the partially ionized medium, allowing self-guiding of the beam over long distances with net zero divergence.

In the time domain, the Kerr effect induces a nonlinear phase shift, a process known as self-phase modulation (SPM):

$$\phi(t) = k(t)z = \frac{\omega_0}{c} n(t) z, \tag{2.30}$$

where z is the propagation distance in the material. This additional phase factor leads to a time- and intensity-dependent shift of the instantaneous frequency, generating new components in the spectrum:

$$\omega = \omega_0 - \frac{d\phi}{dt} = \omega_0 - \frac{\omega_0}{c} n_2 \frac{\partial I(z,t)}{\partial t} z. \tag{2.31}$$

We can demonstrate this effect by adding an SPM-induced phase to a 200 fs Gaussian pulse at 1000 nm central wavelength, see Figure 2.8. There is a clear oscillation of the instantaneous frequency (wavelength) as a function of time [red curve in Figure 2.8(a)], with the leading edge of the pulse resulting in the red-shifted extension of the spectrum, while the trailing edge is responsible for the blue shift. Looking at the frequency domain [Figure 2.8(b)], this translates to a characteristic spectral broadening with several maxima and minima, corresponding to constructive (destructive) interference of similar spectral components generated at different time intervals.

The spectral broadening induced by self-phase modulation is symmetric in frequency, i.e. both sides of the spectrum experience similar values of frequency shift (assuming initially symmetric pulse profile). However, it is usually accompanied by several additional effects that normally cause an asymmetry in the spectral broadening, often manifested as blue-shifting. Firstly, since the peak of the pulse experiences a higher refractive index compared to the edges, the temporal profile is reshaped even in the absence of material dispersion. The trailing edge runs into the more-slowly propagating peak of the pulse and as a result becomes steeper compared to the leading edge. This is called self-steepening. Other contri-

[6]For a Gaussian beam, α = 1.89.

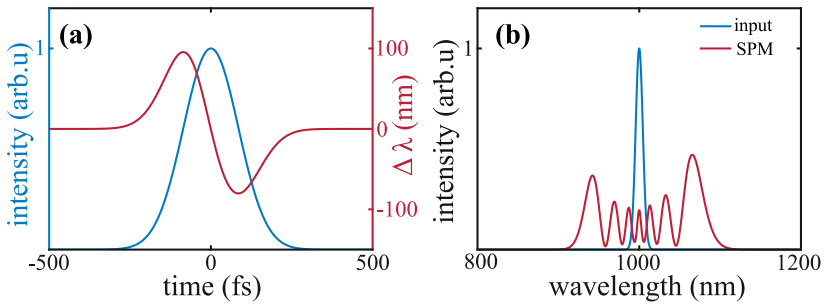

Figure 2.8: Self-phase modulation and its effect on the pulse spectrum. (a) Pulse intensity profile (blue) and shift of the instantaneous wavelength (red) as a function of time. (b) Spectrum of the pulse before and after SPM. The SPM-broadened spectrum is scaled up in intensity for illustration purposes.

butions to the blue shift can originate from the presence of a TOD or the ionization of the optical medium. In the latter case, the increase in density of free electrons causes a rapid drop in the value of the refractive index, thus increasing the instantaneous frequency according to Eq. 2.31. At large intensities, a combined action of the processes discussed above leads to generation of spectral supercontinuum, often giving access to multiple-octave-spanning spectra of coherent radiation, suitable for a multitude of applications, including seeding of broadband OPAs [46].

In conclusion, spectral broadening based on the optical Kerr effect is a robust way of increasing the bandwidth of ultrashort light pulses. If the phase acquired in the nonlinear medium is compensated, the pulse emerges with a shorter duration than before the medium. Post-compression using the optical Kerr effect was first realized in glass optical fibers [37, 47] and later became a routine way of generating mJ-level few-cycle pulses using hollow-core fibers (HCF) seeded by Ti:Sapphire CPAs [48]. In this work, we present results on post-compression of high-average-power ytterbium lasers in multipass cells, discussed in more detail in chapter 4.

Chapter 3

Ultrashort pulse characterization

When the duration of pulses emitted from lasers drops to picoseconds and below, it is no longer possible to capture the time evolution of the light intensity with conventional electronics like photodiodes: on an oscilloscope instead of the coveted pulse shape one would simply see an impulse response function of the measurement device. To be able to measure temporal profiles of such fast events with slow detectors, one usually employs a nonlinear optical effect because its signal (e.g., power or spectrum) is sensitive to the temporal profile of the driving pulse. This thesis work relies on the extensive use of several well-known pulse characterization techniques that are described in this chapter. Firstly, we introduce common approaches that measure and retrieve the electric field of the light pulse. Secondly, we devote a particular focus to the dispersion scan (d-scan) technique: we provide a brief introduction to this method and describe various experimental implementations to measure pulses with different durations both using scanning and single-shot variants. Commonly used retrieval algorithms are also discussed. Finally, we briefly mention ways to characterize and control the carrier-envelope phase of few-cycle pulses.

3.1 Pulse characterization techniques

3.1.1 Intensity Autocorrelation

Intensity autocorrelation emerged as one of the first techniques that could estimate the duration of ultrashort pulses and it is still widely used in many laboratories [49]. The core idea is to create two pulse replicas, mix them in a nonlinear material, and measure the strength of a nonlinear interaction as a function of varying delay between the two replicas. For a pulse that is split into two parts with intensities $I(t)$ and $I(t-\tau)$ (where τ is the

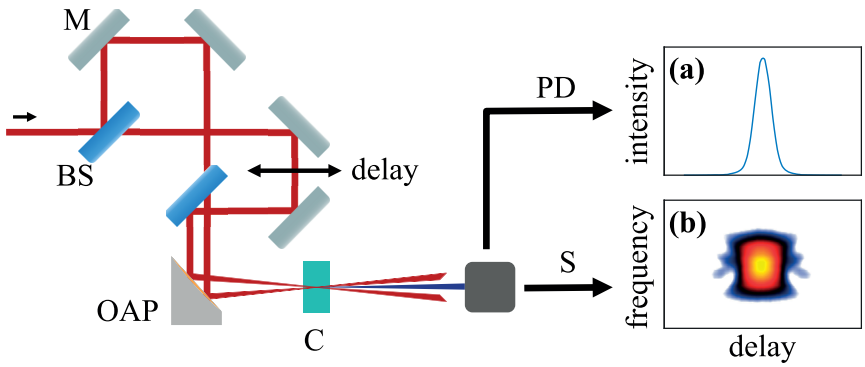

Figure 3.1: Mach-Zehnder interferometer for intensity autocorrelation (a) and FROG (b) measurements. M - mirror, BS - beam splitter, OAP - off-axis parabola, C - nonlinear crystal, PD - photodiode, S - spectrometer.

delay), the intensity autocorrelation function is given by:

$$A(\tau) = \int I(t)I(t-\tau)dt \tag{3.1}$$

The width of $A(\tau)$ is proportional to the duration of the intensity profile, with the proportionality factor depending on the shape of the pulse envelope. The common procedure is to assume a pulse shape and multiply the measurement with a corresponding number [50]. For example, a Gaussian pulse with a full-width-at-half-maximum (FWHM) duration of T produces $\sqrt{2}T$-wide autocorrelation trace.

Experimentally, autocorrelation measurements are realized with an interferometer, and the typical implementation is shown in Figure 3.1. The incoming pulse is split via a beamsplitter, and the length of one of the arms (and thus delay τ) can be varied with a translation stage. The two beams are recombined with a second beamsplitter and focused by a parabolic mirror non-collinearly into the nonlinear crystal. The intensity of the signal (usually second harmonic) as a function of delay is then recorded by a photodiode [Figure 3.1(a)].

The intensity autocorrelation is only able to give an estimate of the pulse duration. While fairly accurate for simple pulse shapes, it tends to give wrong and misleading results for pulses with a complex temporal structure (e.g., with significant third-order dispersion) and phase information is absent in this measurement. It is possible to extract a certain knowledge about the phase when using an interferometric autocorrelation. There, a collinear SHG geometry is used, and the second harmonic cross-term is interfered with SHG contributions from individual pulses. From the resulting interferogram, it is possible to deduce

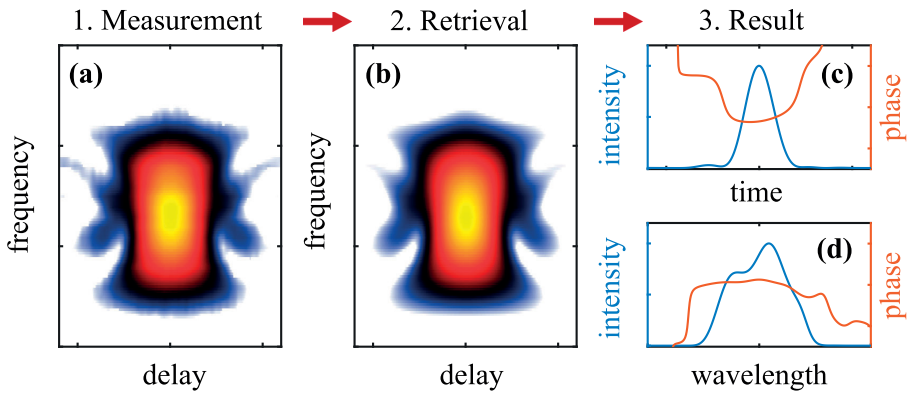

Figure 3.2: Pulse characterization with FROG: 1. A spectrum of a nonlinear signal is measured as a function of delay, and a FROG trace (a) is produced. 2. A Retrieval algorithm aims to find the field that generates a simulated trace (b), identical to the measured one. 3. If the retrieval is successful, a pulse is extracted and can be plotted in the time (c) or frequency (d) domains.

a linear chirp of the pulse, and in certain cases even reconstruct the phase [50–52], however, in practice this technique is rarely used for electric field retrieval: pulses with significantly different profiles can yield nearly identical interferograms [53], which can complicate the measurement and the subsequent data analysis.

3.1.2 Frequency Resolved Optical Gating

If the photodiode is replaced with a spectrometer in Figure 3.1, the correlation signal can now be spectrally resolved at each delay step. A two-dimensional trace is obtained that contains phase information about the pulse, and the electric field can be extracted using an iterative retrieval algorithm. This technique, introduced by Kane and Trebino in 1993, is commonly known as Frequency-Resolved Optical Gating (FROG) [54, 55], and the FROG measurement procedure is conceptually illustrated in Figure 3.2.

The resulting map of intensity versus frequency and delay is a spectrogram $I(\tau, \omega)$, which can be expressed as follows:

$$I(\tau, \omega) = \left| \int_{-\infty}^{\infty} E(t) g(t - \tau) \exp(-i\omega t) dt \right|^2 . \tag{3.2}$$

Here, $E(t)$ is the electric field, and $g(t-\tau)$ is called the gate (hence the name *gating*). The expression for the gate depends on the chosen nonlinearity and experimental geometry -

Process	$g(t-\tau)$
PG	$\lvert E(t-\tau)\rvert^2$
SD	$E(t)E^*(t-\tau)$
SHG	$E(t-\tau)$
THG	$E(t)E(t-\tau)$

Table 3.1: Expressions for gate function $g(t-\tau)$ for different optical nonlinearities. PG - polarization gate, SD - self-diffraction, S(T)HG - second (third) harmonic generation

some examples are presented in Table 3.1. In this work, we used the most common variant of FROG based on non-collinear SHG, for which $g(t-\tau) = E(t-\tau)$ - is simply the delayed pulse replica itself.

First efforts to retrieve the pulse from $I(\tau,\omega)$ were based on generalized projections algorithms, which were in turn based on similar approaches developed in diffractive imaging [56], and the review on their use in FROG measurements can be found in [57]. Here, we briefly outline the important steps for retrieving the pulse using such an algorithm:

1. To start an algorithm, an initial guess for the pulse field $E(t)$ is provided.
2. A time domain trace is generated by calculating $E_{\mathrm{sim}}(t,\tau) = E(t)g(t-\tau)$.
3. The field $E_{\mathrm{sim}}(t,\tau)$ is transformed into the frequency domain and its amplitude is replaced by the amplitude of the measured FROG trace, while the phase is kept, i.e. $\sqrt{I_{\mathrm{sim}}(\omega,\tau)}\exp[i\phi(\omega,\tau)] \Longrightarrow \sqrt{I_{\mathrm{meas}}(\omega,\tau)}\exp[i\phi(\omega,\tau)]$.
4. A new guess for the field E_{new} is calculated from $\sqrt{I_{\mathrm{meas}}(\omega,\tau)}\exp[i\phi(\omega,\tau)]$ by transforming the trace to the time domain and performing e.g., singular value decomposition operation [57].
5. The algorithm enters a new iteration, $E(t) = E_{\mathrm{new}}(t)$.

Steps 2-5 are repeated until a field is found that generates a near-identical trace to the experimental data, and the difference between the measured and retrieved FROG maps is minimized. This difference is usually assessed at every iteration by calculating a root-mean-square (RMS) error G. The error calculation is a standard procedure in almost any iterative retrieval algorithm. The expression for G is given and discussed in more detail in the context of phase retrieval from dispersion scans (Section 3.2.2).

Over the last decades, FROG has become one of the most popular characterization techniques and evolved into its own research field that spawned multiple experimental geo-

metries (e.g., single-shot versions [58, 59], interferometric FROG [60], etc.) and retrieval algorithms (e.g., ptychography [61] or machine learning approaches [62]). In this work, we routinely used a homemade FROG device for the characterization of post-compressed pulses from multipass cells, with results described in detail in chapter 4 as well as **Papers III** and **IV**.

3.1.3 Spectral Phase Interferometry for Direct Electric Field Reconstruction

Another class of pulse characterization techniques is based on spectral interferometry, i.e., the analysis of interference patterns produced by pulses in the spectral domain. A particularly well-known method called Spectral Phase Interferometry for Direct Electric Field Reconstruction (SPIDER) [63] is briefly discussed in this section. The core idea of SPIDER is to analyze a spectral interference between two delayed and frequency sheared (i.e. shifted) pulse replicas. Consider a pulse with a complex field $|\tilde{E}(\omega)|\exp[i\phi(\omega)]$ and its frequency-shifted and delayed replica $|\tilde{E}(\omega+\Omega)|\exp[i\phi(\omega+\Omega)+i\omega\tau]$, where Ω is the amount of spectral shear and τ is the delay. The interference signal measured by the spectrometer is [64]:

$$S(\omega) = |\tilde{E}(\omega)|^2 + |\tilde{E}(\omega+\Omega)|^2 + 2|\tilde{E}(\omega)\tilde{E}(\omega+\Omega)| \cdot \cos\left[\phi(\omega+\Omega) - \phi(\omega) + \omega\tau\right]. \tag{3.3}$$

One of the main advantages of the SPIDER technique is a fairly simple extraction of the spectral phase $\phi(\omega)$ from the measurement, following four steps. (1) The signal $S(\omega)$ is converted to the time domain, where it consists of a DC component (the first two terms in Eq. 3.3) and two sidebands located at $\pm\tau$. (2) Usually, one sideband signal (e.g., at $-\tau$) is kept and transformed back to the frequency domain, while the rest is filtered out. (3) The oscillating term $\omega\tau$ is subtracted from the signal and we are left with the phase difference $\phi(\omega+\Omega)$ - $\phi(\omega)$. (4) For small values of frequency shear, this difference is proportional to the pulse group delay [65], and the spectral phase can be found by integration.

Figure 3.3 shows a typical SPIDER setup. The pulse under test is split into two parts. One arm is sent to the interferometer, where two identical replicas are created with delay τ between them. The pulse in the other arm is stretched in a dispersive element, e.g., either a piece of dense glass or a grating/prism compressor. The two beams are mixed in the nonlinear crystal in an SFG process, and the signal is analyzed with a spectrometer. A frequency shear is introduced since the replicas interact with different frequency components of the chirped pulse.

Overall, this arrangement, though quite complex, does not require any mechanical movement during the measurement and thus is inherently single-shot capable. As FROG, SPIDER has seen a significant development effort over the years, and several variants have

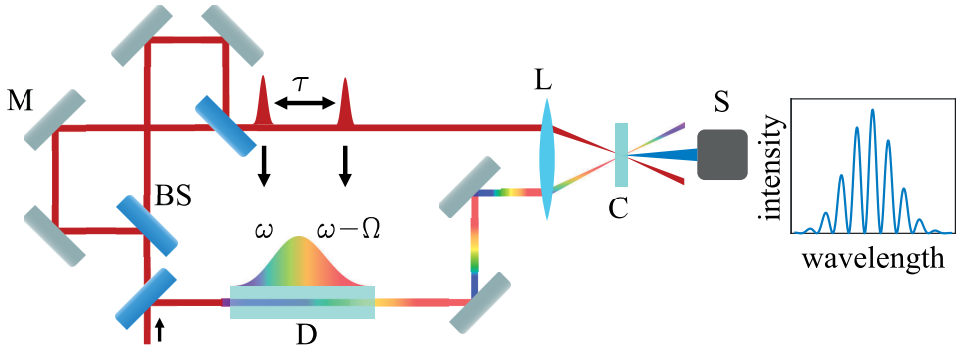

Figure 3.3: Experimental setup of a generic SPIDER measurement. BS - beam splitter, M - mirror, D - dispersive element, τ - delay, L - lens, C - nonlinear crystal, S - spectrometer.

appeared, designed to improve the robustness and versatility of the technique [66–69].

3.1.4 Multiphoton Intrapulse Interference Phase Scan

For laser systems that contain a pulse shaper, it is possible to perform a Multiphoton Intrapulse Interference Phase Scan (MIIPS) [70–72] to characterize the pulse. The general idea of this method is to add to the spectral phase $\phi(\omega)$ a series of controlled phase functions $f(\omega, \delta)$ dependent on a parameter δ and to record the SHG spectrum as a function of δ. For a pulse defined by $\tilde{E}(\omega)$ in the frequency domain, we can define the modulated field as:

$$\tilde{E}(\omega, \delta) = |\tilde{E}(\omega)| \exp[i\phi(\omega)] \exp[if(\omega, \delta)]. \tag{3.4}$$

A common choice for $f(\omega, \delta)$ is

$$f(\omega, \delta) = \alpha \cos(\gamma\omega - \delta). \tag{3.5}$$

The parameters α and γ are usually chosen experimentally, depending on the pulse bandwidth. Most often, α is set to $1.5\,\pi$ while γ is chosen to be equal to the FWHM duration of the Fourier-limit [73].

A MIIPS trace is a 2-dimensional function of frequency and δ. For a given frequency, the second harmonic signal is maximized when the phase introduced by $f(\omega, \delta)$ locally com-

pensates for distortions in the spectral phase $\phi(\omega)$[1]. This condition implies mathematically that the sum of the second derivatives (GDDs) of ϕ and f should be zero:

$$\phi''(\omega) + f(\omega, \delta) = 0. \tag{3.6}$$

Since f is known, the GDD curve of the pulse can be recovered by finding out a value of $\delta = \delta_{\max}(\omega)$ that maximizes the SHG output at each frequency:

$$GDD(\omega) = -f''(\omega, \delta) = \alpha\gamma^2 \cos\left[\gamma\omega - \delta_{\max}(\omega)\right]. \tag{3.7}$$

This method works well for pulses with a relatively simple or slow-varying spectral phase (without significant contributions of high-order dispersion). Complex spectra with fast modulations of spectral intensity/phase require the use of iterative algorithms to achieve precise correction and control of $\phi(\omega)$ [70].

3.2 Dispersion scan

3.2.1 Introduction

The d-scan technique emerged in 2012 [31, 74], and its underlying idea is quite similar to MIIPS. The spectral phase of the light pulse is manipulated by applying varying amounts of dispersion around the point of optimal pulse compression. Simultaneously recording the spectrum of a nonlinear effect, the result of a d-scan measurement, a 2D map of intensity vs. frequency and dispersion, is obtained:

$$I(z, \omega) = \left| \int E_{\mathrm{NL}}(z, t) \exp(-i\omega t) dt \right|^2. \tag{3.8}$$

Here, z denotes the change in dispersion (e.g. a glass wedge insertion), and the field $E_{\mathrm{NL}}(z, t)$ is the result of a chosen nonlinear interaction. Similarly to FROG, a pulse retrieval algorithm is required for the phase reconstruction.

As with the other techniques, the SHG variant of the d-scan is the most common one, for which $E_{\mathrm{NL}}(z, t) = E^2(z, t)$. Other nonlinearities can be used when the detection of the second harmonic is inconvenient. For example, in **Paper I** we used a third harmonic generation (THG) d-scan to characterize the output of the SWIR OPCPA, as the

[1] In other words, $f(\omega, \delta)$ makes $\phi(\omega)$ flat around ω.

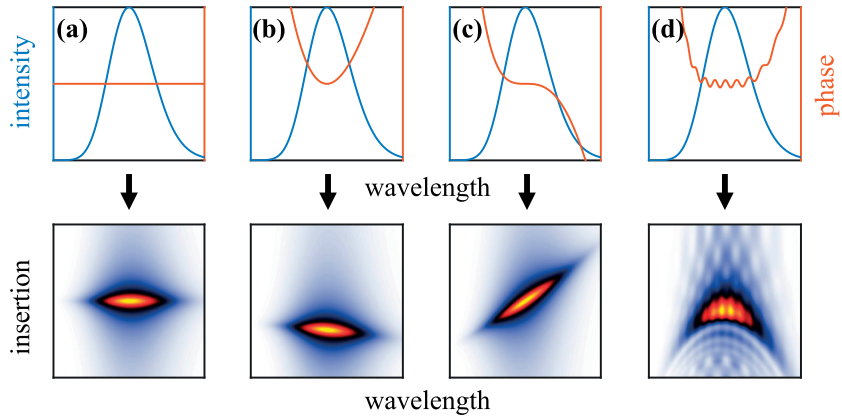

Figure 3.4: D-scan traces for various spectral phase distortions. Top row - spectral intensity and phase for an arbitrary Gaussian pulse, bottom row - corresponding d-scan trace for: (a) flat phase, (b) non-zero GDD, (c) non-zero TOD, (d) non-zero FOD with additional phase ringing, which is often seen in chirped-mirror-based compressors.

second harmonic spectrum could not be detected with a single spectrometer. Degenerate nonlinear processes, like cross-polarized wave generation or self-diffraction are particularly useful when characterizing pulses in the ultraviolet, where frequency conversion approaches quickly become impractical [75, 76]. In the following chapter, we will only focus on discussing the properties of SHG d-scans.

The d-scan technique offers several advantages that make it a method of choice in many laboratories all over the world. First of all, d-scan requires a minimum amount of additional components to perform the measurement, since a mean of manipulating the spectral phase (dispersion), i.e., a compressor, is already present in most setups. Secondly, there is no need for beam-splitting, in contrast to FROG or SPIDER, which lowers the requirement on the incoming pulse energy to generate a sufficiently strong nonlinear signal and makes the optical setup simpler and more compact. Finally, a particular advantage of the d-scan technique lies in the amount of information that can be extracted directly from the shape of the trace. Common spectral phase distortions (e.g. non-zero GDD or TOD) appear as characteristic deformations, with several examples illustrated in Figure 3.4. For example, applying a second-order phase (i.e., GDD) will shift the trace up or down on the dispersion axis [Figure 3.4(b)][2]. TOD, in turn, presents itself as a linear tilt, while fourth-order dispersion (FOD) results in a parabolic deformation of the d-scan trace [Figure 3.4(c)

[2]There also appears a slight tilt in the trace. This is due to the fact that d-scan uses propagation through glass to vary the phase, and the phase from the glass is never a pure GDD but contains high-order terms as well.

and (d), respectively]. This makes the d-scan a robust and easy-to-use reference tool when optimizing the output of ultrafast light sources.

3.2.2 Pulse retrieval

The extraction of quantitative pulse information from a d-scan trace requires solving an inverse problem with the use of iterative retrieval algorithms. Again, we seek to find such a field that produces a trace similar to the experimental data, and the similarity is estimated through the calculation of the RMS error G. For the trace sampled with $m = 1, 2, ...N_m$ dispersion and $k = 1, 2, ...N_k$ frequency points[3],

$$G^2 = \frac{1}{N_m N_k} \sum_{m,k} \left(I_{\mathrm{meas}}(z_m, \omega_k) - \mu_k I_{\mathrm{retr}}(z_m, \omega_k) \right)^2 , \tag{3.9}$$

with

$$\mu_k = \frac{\sum_m I_{\mathrm{meas}}(z_m, \omega_k) I_{\mathrm{retr}}(z_m, \omega_k)}{\sum_m I_{\mathrm{retr}}(z_m, \omega_k)^2} \tag{3.10}$$

Here, I_{meas} and I_{retr} are the measured and simulated traces, respectively, and μ_k is a function which is updated at every iteration and which accounts for the spectral response of the measurement system (e.g., SHG conversion efficiency and spectrometer response). The task of minimizing G belongs to the class of nonlinear least-squares problems, for which a number of well-known algorithms is available. One of the classical least-squares solvers, the Nelder-Mead (NM) or downhill simplex algorithm [77] was the method of choice in the early stages of d-scan development, and is still often used due to its reliability. A pseudocode implementation of this algorithm is presented below in Table 3.2.

The algorithm is initialized by creating an array of spectral phases (simplex) with $n+1$ components called vertices, each vertex corresponding to one guess phase, parameterized with n elements. At each step, G is evaluated and the vertex (phase) that gives the highest error is replaced. The algorithm adopts several protocols (called reflection, expansion, contraction or shrinking) that define with which point the worst vertex should be substituted before going to the next iteration. At each iteration, a stopping criterion is estimated, which is usually taken as a difference of the error G for the best and the worst vertices. When such a criterion (or a maximum number of iterations) is reached, the algorithm outputs the best guess for the phase and exits the loop.

[3]The value of G depends not only on the sampling but also on how the trace is normalized. Therefore, great caution has to be taken when comparing retrieval results from different measurements.

Table 3.2. Nelder-Mead retrieval algorithm. α, γ, ρ and σ are called reflection, expansion, contraction and shrinking coefficients, respectively, with standard values $\alpha = 1$, $\gamma = 2$, $\rho = 0.5$ and $\sigma = 0.5$.

1:	Simplex of phases ϕ_j, j = 1...n + 1	▷ Initialization
2:	Evaluate G and the stopping criterion	▷ Algorithm loop
	Sort ϕ_j such as $G(\phi_1) < G(\phi_j) < G(\phi_{n+1})$	
3:	Calculate centroid: $\phi_0 = \sum_j^n \phi_j / n$	
4:	Calculate reflection point: $\phi_r = \phi_0 + \alpha(\phi_0 - \phi_{n+1})$	
5:	**if** $G(\phi_1) < G(\phi_r) < G(\phi_n)$ **then**	
	$\phi_{n+1} = \phi_r$	▷ and go to Step 2
6:	**if** $G(\phi_r) < G(\phi_1)$ **then**	
	Calculate expansion point: $\phi_e = \phi_0 + \gamma(\phi_r - \phi_0)$	
7:	**if** $G(\phi_e) < G(\phi_r)$ **then**	
	$\phi_{n+1} = \phi_e$	▷ and go to Step 2
8:	**else**	
	$\phi_{n+1} = \phi_r$	▷ and go to Step 2
9:	**if** $G(\phi_r) < G(\phi_{n+1})$ **then**	
	Contraction outside: $\phi_c = \phi_0 + \rho(\phi_r - \phi_0)$	
10:	**if** $G(\phi_c) < G(\phi_r)$ **then**	
	$\phi_{n+1} = \phi_r$	▷ and go to Step 2
11:	**if** $G(\phi_r) \geq G(\phi_{n+1})$ **then**	
	Contraction inside: $\phi_c = \phi_0 + \rho(\phi_{n+1} - \phi_0)$	
12:	**if** $G(\phi_c) < G(\phi_{n+1})$ **then**	
	$\phi_{n+1} = \phi_c$	▷ and go to Step 2
13:	Shrinking: $\phi_j = \sigma(\phi_j - \phi_1)$, j = 2...n + 1	▷ and go to Step 2

For efficient performance of the NM retrieval (and any general optimization algorithm), the guess for the spectral phase has to be described in a convenient mathematical basis. An obvious choice is to let every point of the phase be an independent variable according to the sampling of the spectrum. However, this often leads to a large number of dimensions (large n) in the problem, slowing down the algorithm's convergence. Instead, a Taylor or Fourier series representations can be used, each with its advantages and drawbacks. The former is a good choice for clean phases that produce simple d-scans; however, strong coupling between even and odd terms of different orders can lead to a poor convergence for complicated traces [31]. The latter, while performing better in retrieving more complex phases, is prone to get stuck in local minima. More advanced strategies include spline interpolation [78] or a switch of parameterization in case of stagnation [74].

While in theory, both spectral phase and amplitude can be retrieved, it is rarely done so in practice: requiring the NM algorithm to retrieve the amplitude together with the phase doubles the amount of dimensions in the problem and thus makes the algorithm unnecessarily slow. In most cases, a separate measurement of the pulse spectrum is performed and fed into the algorithm.

The NM method described above is just one of the many procedures that have been adapted for pulse reconstruction from d-scans. In the same category, general optimization approaches like Levenberg-Marquardt or differential evolution algorithms have been reported to be implemented with the d-scan [79, 80]. Constraint-based algorithms, e.g. GP routines mentioned earlier in the context of FROG retrievals, can provide faster convergence when compared to brute-force minimization. However, they are prone to be less reliable when noise is present in the experimental data [81, 82]. A fairly recent and exciting development is the use of machine learning for phase retrieval [61], recently proposed for d-scan [83]. They show retrieval times on the scale of milliseconds, a very attractive feature when combined with video-like refresh rates often found in single-shot d-scan setups.

3.2.3 Scanning d-scan

The first dispersion scans characterized the output of a few-cycle Ti:Sapphire oscillator, where the compressor consisted of chirped mirrors and a pair of BK7 glass wedges. An implementation of such a setup is shown in Figure 3.5. Passing through the compressor, the pulse is focused into a thin crystal, e.g., BBO. A polarizer is often used to isolate the second harmonic from the fundamental, and the SHG signal is then resolved by a fiber spectrometer. By moving one of the wedges in and out of the beam, the phase of the pulse is changed according to Eq. 2.12, giving the vertical dispersion axis to the trace.

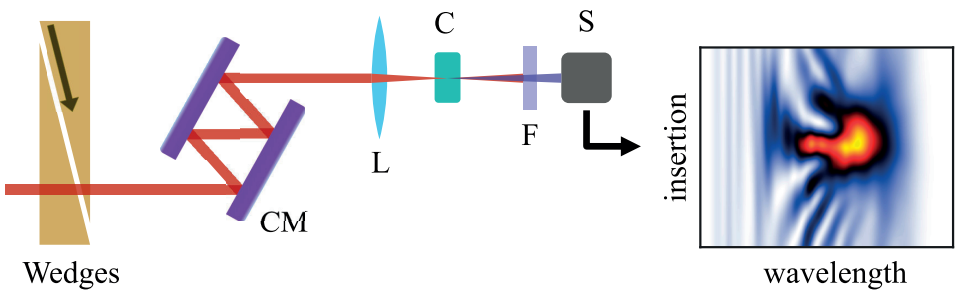

Figure 3.5: Experimental setup for a d-scan measurement based on a chirped mirror (CM) and wedge pair compressor. L - lens, C - crystal, F - filter, S - spectrometer.

In the previous chapter, we have discussed how dispersion affects pulses of different spectral

bandwidths and thus influences the choice of compressor design in the laser system. Since the compressor is an integral part of the d-scan, a similar reasoning can be applied here as well. The spectral width of the pulse (or equivalently its FL pulse duration) essentially determines the length of the dispersion window that is needed in order to fully record the evolution of a nonlinear signal as it goes through the point of best compression, which is desirable for a robust pulse retrieval. While for pulses with octave spanning spectra, only a few hundreds of fs^2 of GDD might be needed to sufficiently stretch or compress the pulse, narrow spectra require orders of magnitude larger values. To obtain a well-contained d-scan trace, we typically aim to scan $10 - 20$ dispersion lengths (Eq. 2.13) for a given pulse. This corresponds to a GDD window of $\pm$ (4 - 6) $\times \tau_0^2$ [fs^2], where τ_0 is the duration of the Fourier-limited pulse[4]. In **Paper V**, we provide several examples of how the d-scan can be adapted to different pulse duration regimes. A brief summary of this study is given below.

In glass-wedge-based compressors, a correct choice of wedge material dictates the achievable range of GDD values that can be applied to the pulse. Low dispersion glasses like BK7 or fused silica are suitable for characterizing few-cycle light sources in the near-infrared, e.g. Ti:Sapphire-based hollow-core fiber compressors (HCFs) or OPCPAs. In Figure 3.6(a)-(c), a SHG d-scan of the output of the Ti:Sapphire HCF compressor in the University of Porto is presented. The width of the dispersion window in Figure 3.6(a) is only $135\,\mathrm{fs}^2$, sufficient to contain the trace. The corresponding FWHM duration is 3.4 fs, with the pulse approaching the duration of a single cycle.

In the multi-cycle case, the same $135\ \mathrm{fs}^2$ of GDD would have a negligible effect on the pulse duration and thus will not be enough to produce a well-defined d-scan trace. In the measurement shown in Figure 3.6(d)-(f), we instead used ZnSe wedges to characterize a mJ-level 1 kHz Ti:Sapphire CPA in Lund, retrieving a pulse duration of 20.4 fs. ZnSe is ~ 20 times more dispersive than BK7 at 800 nm, and the dispersion window is now $3240\,\mathrm{fs}^2$.

For even narrower spectra, or for pulses with a large time-bandwidth product, dispersion control based on material insertion becomes unpractical. Prism or grating compressors are normally used, and with the addition of a motor they can easily be adapted to measure d-scans. In the last row of Figure 3.6, (g)-(i), a measurement on a high pulse energy 10 Hz Ti:Sapphire CPA is shown, and the dispersion is scanned by moving one of the compressor gratings. The grating compressor introduces $4300\,\mathrm{fs}^2/\mathrm{mm}$, giving a scan window of $12900\,\mathrm{fs}^2$. The retrieved pulse duration is 43.4 fs.

[4]This mostly applies to rather well compressed traces. For d-scans dominated with e.g., significant TOD contributions, the dispersion window should be larger.

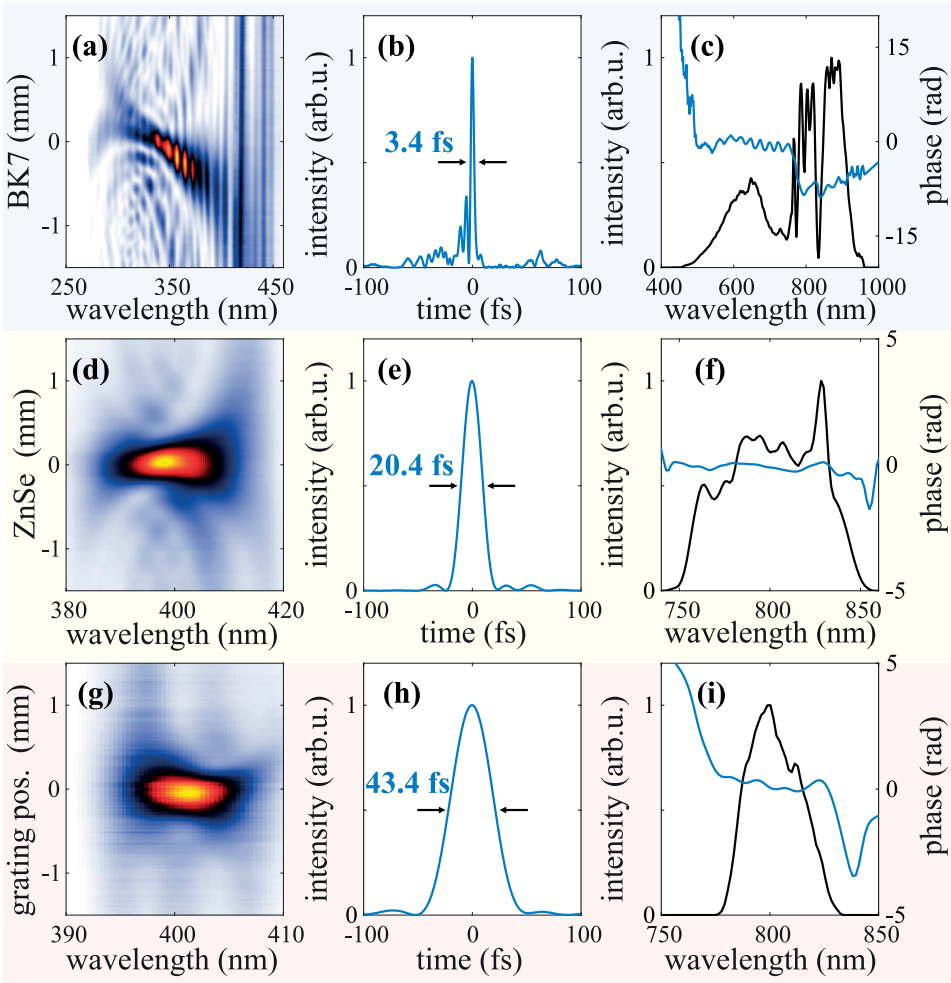

Figure 3.6: SHG d-scan measurements in different pulse duration regimes. Measured trace (left), retrieved temporal intensity profile (center), and measured spectrum with retrieved phase (right) of different Ti:Sapphire-based systems: (a)-(c) 1 kHz HCF post-compressor at Porto University, (d)-(f) 1 kHz and (g)-(i) 10 Hz CPAs at LLC.

3.2.4 Single-shot d-scan

The approaches discussed before rely on the mechanical translation of one of the elements in the compressor to perform a dispersion scan. For systems with moderate-to-high repetition rates (>1 kHz), the scanning d-scan provides information about the average pulse in the

pulse train. However, this technique may not be optimal, if used with high energy, low repetition rate laser setups: the measurement takes a long time and/or gives misleading results, if significant pulse-to-pulse instabilities are present. Thus, it is more appropriate to rely on methods that can characterize single pulses, and the d-scan has seen a significant development in the direction of single-shot measurements over the years [84–86]. Here, two single-shot geometries that can characterize near-infrared few- and many-cycle pulses are briefly described. More details can be found in **Paper V**.

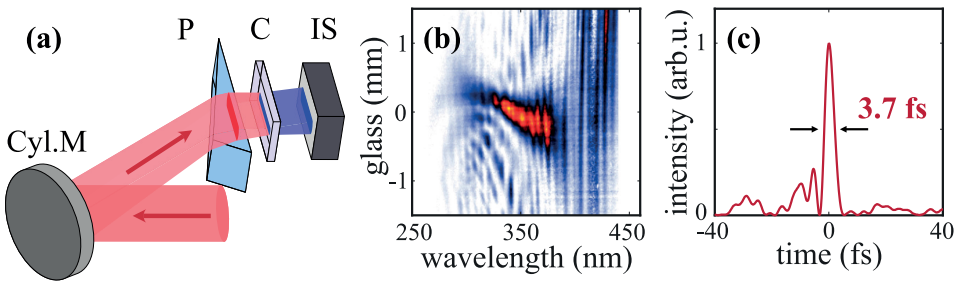

Figure 3.7: Few-cycle single-shot d-scan. (a) Optical layout. Cyl.M - cylindrical mirror, P - prism, C - SHG crystal, IS - imaging spectrometer. (b) Experimental d-scan trace from the output of a HCF compressor. (c) Corresponding retrieved pulse intensity profile.

The first approach is mostly suitable for few-cycle pulse characterization and relies on mapping varying amounts of dispersion across the spatial beam profile. This is usually achieved by propagation through a glass prism. The beam is then focused in one dimension, and the line in the crystal is imaged with an imaging spectrometer. To achieve this, several focusing geometries are possible. For example, one can image a slit placed in front of the prism onto a BBO crystal and then image the crystal onto the slit of the spectrometer [84]. A more space-efficient way is to propagate the beam through a prism and then image[5] the exit surface onto a crystal with a spherical mirror under a large angle of incidence [85]. A large off-axis angle induces strong astigmatism, resulting in two focal planes, with the crystal placed in the horizontal focus. In **Paper V** we presented yet another solution which relies on a cylindrical mirror focusing the beam onto a crystal, with a prism placed in between. This geometry is shown in Figure 3.7(a). A few practical considerations have to be taken into account. (1) The angle of incidence on the mirror and prism rotation must be carefully adjusted to reduce the influence of aberrations. (2) The crystal must be placed directly after the output facet of the prism to minimize the effect of angular dispersion.

We tested this configuration by characterizing the pulses from the same HCF-based system shown in the previous section. We use a home-built astigmatism-corrected imaging spectrometer based on a crossed Czerny-Turner configuration [87], with the detailed design described in [85]. The trace is nearly identical to the one presented in Figure 3.6(a), and

[5]Imaging helps to minimize the impact of angular dispersion.

the retrieved pulse duration is 3.7 fs, very similar to the result obtained with the scanning variant.

It is not straightforward to adapt this approach for measurements of longer multi-cycle pulses, and the reasons are similar to those described previously: the amount of GDD introduced by a prism across the beam profile is usually limited, even for large beam sizes. An alternative solution was demonstrated by Salgado-Remacha *et al.* in 2020. It relies on transverse second harmonic generation (TSHG) in a highly dispersive nonlinear crystal [Figure 3.8(a)]. As the pulse propagates through the crystal, it generates a second harmonic signal at different positions along the propagation axis, corresponding to different dispersion values. The signal is then analyzed with an imaging spectrometer, producing a conventional d-scan trace.

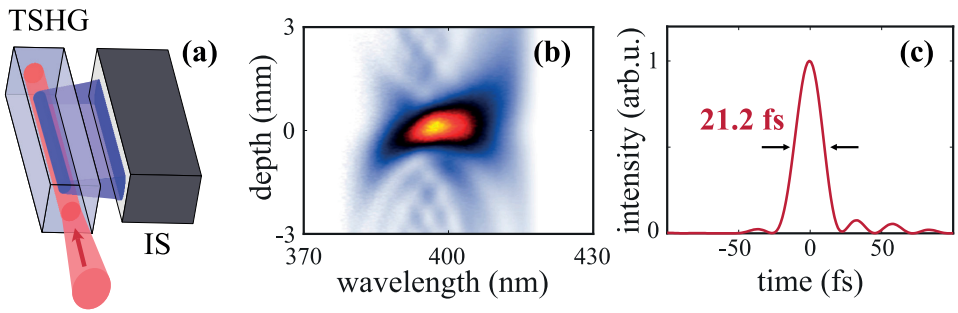

Figure 3.8: Multi-cycle single-shot d-scan based on TSHG. (a) Optical layout. TSHG - transverse second harmonic generation crystal, IS - imaging spectrometer. (b) Experimental d-scan trace from the output of a mJ Ti:Sapphire CPA. (c) Corresponding retrieved pulse intensity profile.

In the experiment described in **Paper V**, we used a disordered nonlinear crystal of strontium barium nitrate, or SBN. At 800 nm it introduces approximately 500 fs^2 (about 10 times more than BK7) of GDD per mm of length. We tested this geometry on the output of a 1 kHz Ti:Sapphire CPA, for which the scanning measurement was shown previously [Figures 3.6(d)-(f)]. The trace is well-contained, and the retrieved duration is 21.4 fs, which corresponds well to the value shown in Figure 3.6(e).

3.3 Carrier-envelope phase stability measurements

The stabilization and control of the carrier-envelope phase of few-cycle pulses are primary challenges in ultrafast optics, and various techniques to measure and stabilize the CEP have been proposed since the 1990s. Strong-field phenomena, like tunneling ionization by an intense light pulse, are sensitive to the instantaneous electric field strength and thus

can be used to probe the absolute phase. For example, the observation of an asymmetry in the emission direction of electrons in above-threshold-ionization (ATI) gave rise to a powerful method of CEP characterization called stereo-ATI [88–90]. Similarly, attosecond streaking [91], or advanced field sampling approaches [92, 93] can also access the CEP, but the experimental implementation of these techniques is often rather complex and is challenging at low pulse energies.

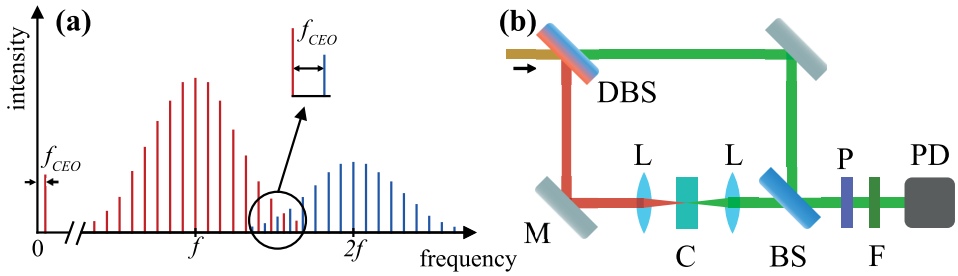

Figure 3.9: Measurement of the CEO frequency. (a) Fundamental and second-harmonic frequency combs of ultrafast mode-locked oscillator. (b) Simplified schematic of an f - $2f$ interferometer for measuring f_{CEO}. (D)BS - (dichroic) beamsplitter, M - mirror, L - lens, C - SHG crystal, P - polarizer, F - spectral filter, PD - photodiode.

Less demanding methods are employed for the CEP stabilization of ultrafast oscillators and amplified pulses [94–96]. In a high-repetition-rate laser oscillator, the difference between phase and group velocities of the pulse leads to a dephasing between the carrier and the envelope during a round trip in the cavity. In other words, there is a CEP slip $\Delta\varphi$, which typically changes from pulse to pulse. Now, consider the problem in the frequency domain. The output spectrum of an oscillator is a frequency comb, with the n-th comb line having a frequency of $f_n = f_{\mathrm{CEO}} + n f_{\mathrm{rep}}$, where f_{rep} is the repetition rate of the laser, and f_{CEO} is the so-called carrier-envelope offset (CEO) frequency. The f_{CEO} can be understood as the difference between zero-frequency and the first comb line of the oscillator spectrum extrapolated to zero [Figure 3.9(a)]. The offset frequency is directly related to $\Delta\varphi$ as [45]:

$$f_{\mathrm{CEO}} = \frac{\Delta\varphi}{2\pi} f_{\mathrm{rep}}. \tag{3.11}$$

The measurement of the CEO frequency is usually performed with an f - $2f$ interferometer[6]. A simplified implementation is shown in Figure 3.9(b). The pulse is split into two spectral components via a dichroic beamsplitter. The long-wavelength part generates the second harmonic in a nonlinear crystal, which then interferes with the short-wavelength

[6]This requires an octave-spanning fundamental spectrum, which, if not available, can be obtained via additional spectral broadening.

part of the spectrum. Since the fundamental and the second harmonic are orthogonally polarized, an additional polarizer is used to make the two interfere. Finally, the interference signal is filtered with a narrowband spectral filter and is sent onto a photodiode.

The f_{CEO} is obtained as the beat frequency between the fundamental frequency comb, $f_n = f_{\mathrm{CEO}} + nf_{\mathrm{rep}}$ and the second harmonic of the fundamental frequency comb $2f_m = 2f_{\mathrm{CEO}} + 2mf_{\mathrm{rep}}$) in the region of their spectral overlap [Figure 3.9(a)]. The interference between the comb lines at frequencies $n = 2m$[7] gives a beat note at f_{CEO}, which is then detected by a fast photodiode. The signal is processed by an RF spectrum analyzer. Once measured, the value of f_{CEO} can be stabilized by locking it to a reference waveform with a phase lock loop (PLL), varying a certain parameter in the laser cavity, e.g., the pump power, which changes the refractive index in the laser crystal.

This technique is used to stabilize the offset frequency of the Ti:Sapphire oscillator front-end of the parametric amplifiers described in **Papers I and II** to a quarter of the repetition rate (i.e., 20 MHz), yielding every 4th pulse in the oscillator pulse train to carry the same CEP ($\Delta\varphi = \pi/2$). The pulse picking in the amplifier chain is then performed so that only seed pulses with the same CEP are amplified later in the near-infrared OPCPA.

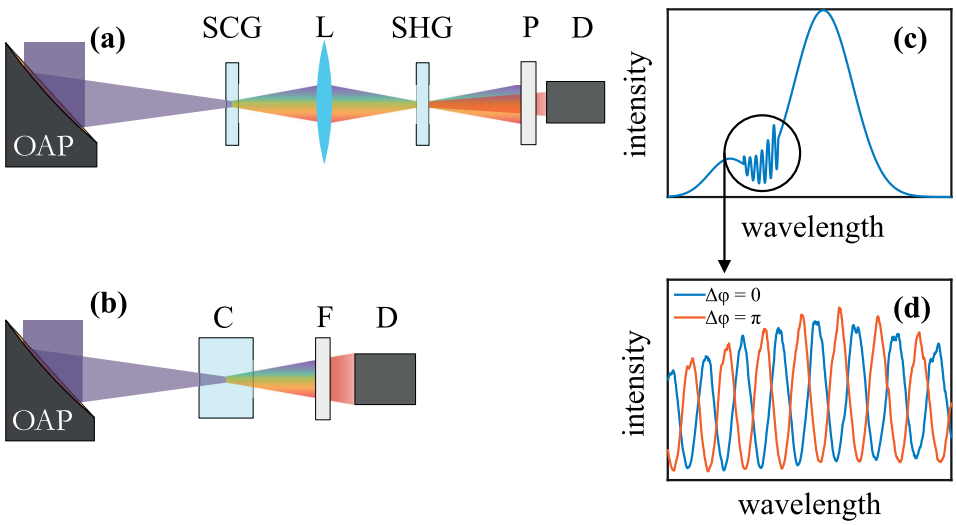

Figure 3.10: Spectral-interferometry-based CEP measurements. (a) A standard f - $2f$ setup, OAP - off-axis parabola, SCG - supercontinuum generation, L - lens, SHG - second harmonic generation, P - polarizer, D - detector. (b) A simplified monolithic setup, C - nonlinear crystal, F - filter. (c) In the region of spectral overlap between e.g. f and $2f$ components, CEP-sensitive spectral fringes can be found. (d) Position of the fringes for two values of CEP offset.

[7] E.g., at $n = 1000$ for the fundamental and m = 500 for the second harmonic comb lines.

For amplified pulses emitted at lower repetition rates, another method must be used, which is based on analyzing the f - $2f$ interference signal spectrally. A typical setup for this measurement is shown in Figure 3.10(a). The pulse is spectrally broadened in a supercontinuum generation (SCG) crystal and then refocused into an SHG crystal with a lens. Again, a polarizer projects the f and $2f$ components onto a common polarization axis to create interference. The signal is analyzed by a fiber spectrometer, and the fringe intensity is given by:

$$I(\omega) = I_f(\omega) + I_{2f}(\omega) + 2\sqrt{I_f(\omega) I_{2f}(\omega)}\cos(\omega\tau + \Delta\varphi), \tag{3.12}$$

where τ is the delay between the f and $2f$ components[8] and $\Delta\varphi$ is the value of the CEP relative to some arbitrary number. The variation in the position of the fringes is directly related to the change in the CEP: for example, a π change in the CEP results in a similar drift of the spectral fringe pattern, as shown in Figure 3.10(d), meaning that the *relative* CEP can be extracted by recording the position of the fringes over time.

This approach is often limited by the speed of data acquisition and processing, and while for kHz-repetition-rate systems, single-shot measurements are straightforward, it is difficult to assess shot-to-shot CEP fluctuations at higher repetition rates. In **Paper II**, we use a fast line camera (Basler) to record spectral interference fringes and characterize the out-of-loop CEP stability of the 200 kHz near-infrared OPCPA on a shot-to-shot basis. The results are briefly discussed in chapter 4.

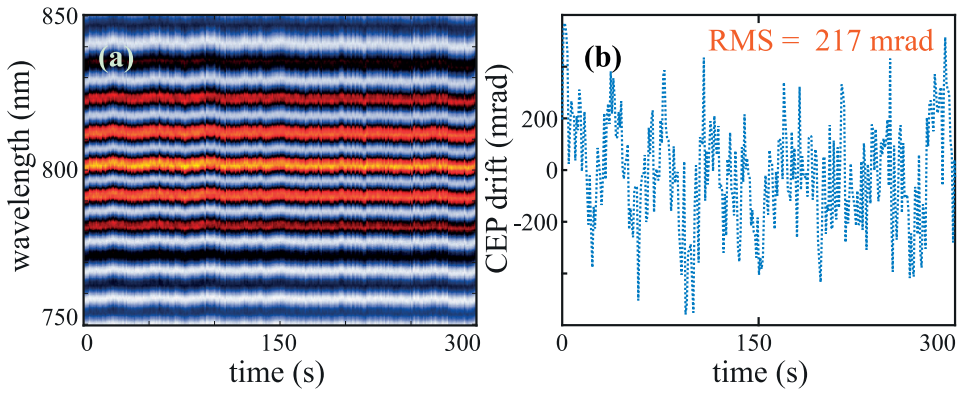

Figure 3.11: A CEP stability measurement of the DFG output of the SWIR light source (a) An interferogram acquired over 5 minutes in a BiBO crystal, spectrometer integration time is 2 ms (b) CEP drift as a function of time, RMS - root mean square.

In **Paper I**, instead of the standard geometry depicted in Figure 3.10(a), we implement a

[8]Unlike the fast oscillator measurement, where the f and $2f$ must be temporally overlapped, here, a delay is introduced between the two components in order to observe the fringe pattern and reliably extract the phase.

monolithic CEP interferometer [Figure 3.10(c)], similar in spirit to the one reported in [97]. Here, broadening and sum-frequency generation are combined in a single nonlinear crystal, and after the spectral filter, the CEP-sensitive signal is sent directly to the detector. The signal is resolved by a spectrometer, where the interference fringes in the region of the spectral overlap can be seen. In Figure 3.11, we show an example of a stability measurement of the passively-CEP-stable idler pulses generated in the DFG stage of the SWIR light source, based on the monolithic scheme. By focusing the pulse into a 4-mm-thick BiBO crystal, we generate CEP-sensitive fringes around 800 nm wavelength and detect them with a fiber spectrometer. Accumulating the fringe spectra over 5 minutes, we can extract the phase variation as a function of time and obtain an RMS value of 217 mrad. The integration time of the spectrometer was set to 2 ms, meaning that the phase noise above 500 Hz is averaged out.

Chapter 4

Ultrashort-pulsed light sources

Advances in attosecond and strong-field science are closely connected to the emergence of new driving laser technology operating at high repetition rates and different central wavelengths. The development of such drivers is one of the cornerstones of this thesis work. This chapter focuses on discussing the technical aspects and parameters of light sources that were either developed or optimized during this thesis work. First, we give an overview of two high-repetition-rate optical parametric chirped pulse amplifiers (OPCPAs) located at the Lund Laser Centre. They both emit sub-2.5-optical-cycle pulses in the near- and short-wave infrared and are presented in **Papers I** and **II**. Second, we show the results of post-compression of pulses from high-power Yb laser amplifiers based on gas- and solid-state multipass cells (Papers **III** and **IV**, respectively).

4.1 Optical parametric chirped pulse amplification systems

OPCPA as a concept is nearly identical in spirit to a classic CPA: the seed pulse is stretched, amplified, and then re-compressed back to the original duration. The critical difference lies in that stimulated-emission-based amplification is replaced by parametric interaction (i.e., OPA) in a nonlinear crystal. This difference has a few significant consequences: (1) there is no storage of pump laser energy in the nonlinear medium, allowing high average power scaling (due to a lower thermal load, determined by crystal absorption), (2) the amplification process is not tied to a specific laser-active transition and thus can be achieved in parts of the electromagnetic spectrum where no suitable laser materials are available, (3) depending on phase matching conditions, the spectral bandwidth of OPAs can be extremely broad, allowing direct amplification of spectra supporting few-cycle pulse durations, without significant gain narrowing.

Both OPCPAs discussed in this thesis are derived from the same oscillator front-end. They operate in two different spectral regions but with similar output pulse energies and comparable pulse durations (in terms of the number of optical cycles).

4.1.1 Front-end oscillator. Yb fiber CPA

The shared front-end of the two OPCPA systems is a broadband Ti:Sapphire oscillator (Venteon), delivering sub-6 fs near-infrared pulses at the repetition rate of 80 MHz (Figure 4.1). The oscillator spectrum is octave-spanning, allowing for the stabilization of the CEP slip with an f- $2f$ interferometer without additional spectral broadening. The oscillator output is sent into a $4f$ pulse shaper, which is used to finely tune and pre-compensate the phase of the seed pulses in the near-infrared OPCPA. The phase correction is introduced by adjusting the voltages on a spatial light modulator placed in the Fourier plane of the shaper.

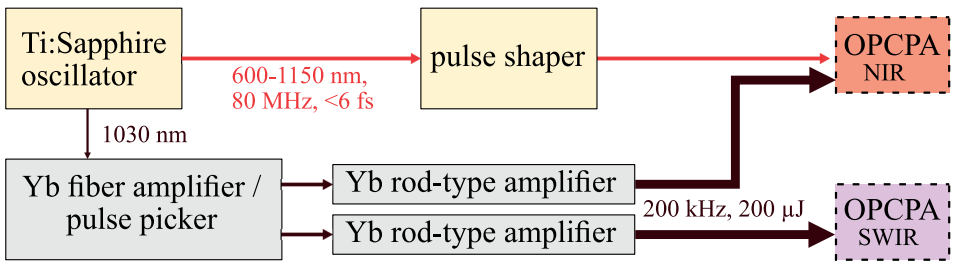

Figure 4.1: A simple sketch of the front-end and the Yb fiber amplifier chain.

A fraction of the oscillator spectrum centered around 1030 nm is filtered out and sent into an Yb fiber CPA chain, consisting of a fiber pre-amplifier (VALO Innovations), (pre-amp), and a pair of high-power rod-type amplifiers. In the pre-amp, the pulses are stretched via a chirped fiber Bragg grating to ~ 0.5 ns duration and amplified in three amplification stages, while the repetition rate is reduced to 200 kHz by a pair of acousto-optic modulators. The pre-amp has two identical ~ 4 µJ outputs, which are separately coupled into two 1-m-long Yb rod-type amplifiers (NKT Photonics) and further amplified to the energy of ~ 200 µJ. One of the rod-type amplifiers pumps the near-infrared OPCPA, while the other one pumps the short-wave infrared OPCPA system.

4.1.2 Near-infrared OPCPA

Setup description

The near-infrared, few-cycle-pulsed light source was initially a commercial OPCPA system (Venteon) set up in Lund in 2012. It has seen a significant development effort over the years that aimed at boosting the power and improving the stability of the amplified pulses. The details of the "first iteration" of this setup are described elsewhere [98]. In the initial stages of this thesis work, an upgrade of the Yb fiber amplifier allowed the increase of the output pulse energy from 8 µJ to 15 µJ without affecting the pulse duration (6 fs). This version of the setup is briefly described in **Paper II**, where its upgraded capabilities allowed us to drive challenging pump-probe and coincidence studies. We have also used the few-cycle near-infrared OPCPA to drive coherent currents in gallium nitride, as described in **Paper VI**.

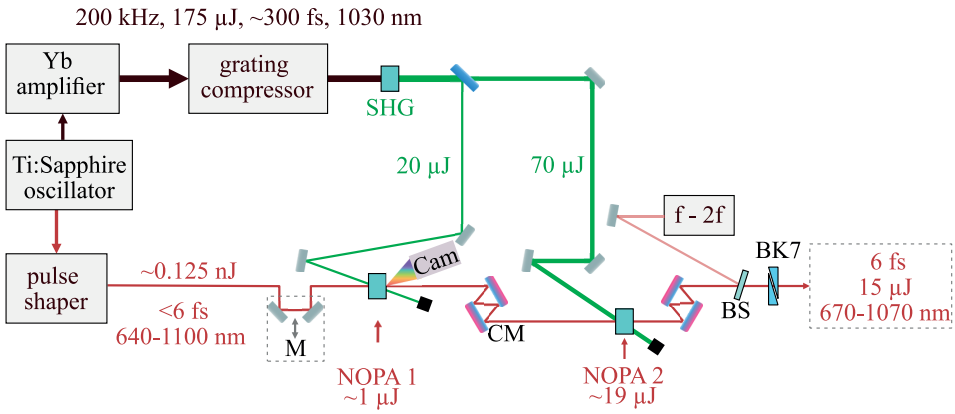

Figure 4.2: A schematic of the few-cycle NIR OPCPA system. M - motorized translation stage, Cam - Camera, CM - chirped mirrors, BS - beam sampler, BK7 - BK7 glass wedge pair.

A simple sketch of the setup is shown in Figure 4.2. The pump source for the system is the output from one of the Yb rod-type amplifiers. Firstly, it is compressed in the grating compressor to ~ 300 fs pulse duration. Infrared pulses with the energy of 175 µJ are sent into a 1.5-mm-thick BBO crystal for SHG. We typically generate 90 µJ of 515 nm radiation (51% conversion efficiency). The green is split into two parts with energies of 20 and 70 µJ, which are used to pump two NOPA stages.

The seed from the Ti:Sapphire oscillator passes through the pulse shaper and enters the first NOPA stage, where it is amplified from 0.125 nJ to ~ 1 µJ. The delay between the pump and the seed beams in the NOPA is stabilized by recording the angularly dispersed beam profile of the second harmonic of the idler with a camera [99] and sending the feedback

to a motorized translation stage. The pulses are further sent to the second amplification stage, where the energy is boosted to 19 µJ. The dispersion in the setup is controlled by a combined action of the $4f$ pulse shaper, chirped mirrors, and BK7 wedges. The wedge pair is motorized, allowing for a precise pulse characterization with the dispersion scan technique. Finally, a fraction of the output pulse energy is sent into a conventional f - $2f$ interferometer for slow-loop CEP stabilization. Pulses with an energy of 15 µJ (3 W average power) and central wavelength of 850 nm can then be sent to pulse characterization devices or to the experiment.

Output pulse characterization

To measure the output pulse duration, we use a second-harmonic d-scan. The measured and retrieved d-scan traces are shown in Figures 4.3(a) and 4.3(b), respectively. Even though the trace and the retrieved spectrum are highly structured, the retrieved phase remains flat over the whole bandwidth of the pulse [Figure 4.3(c)]. The pulse duration is approximately 6 fs FWHM, very close to the Fourier limit of 5.7 fs [Figure 4.3(d)].

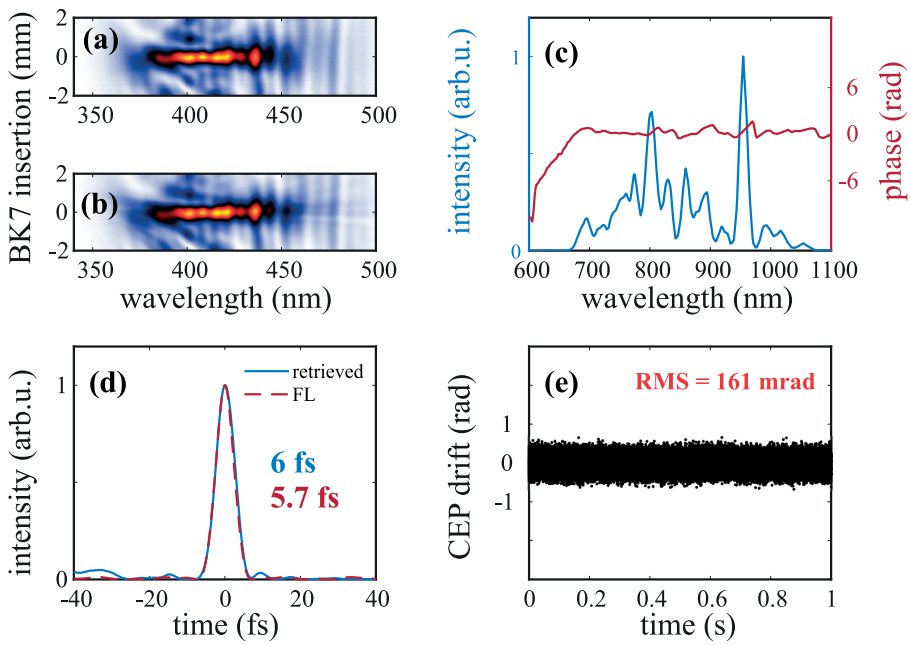

Figure 4.3: (a) Measured and (b) retrieved SHG d-scan traces of the amplified output. (c) Retrieved spectrum and retrieved spectral phase. (d) Retrieved pulse intensity profile and Fourier-limited pulse of the spectrum in (c). The pulse duration is given at FWHM and the temporal profiles are normalized to 1. (e) Single-shot CEP stability measurement.

Furthermore, we measured the CEP stability of the output in a separate f - $2f$ interferometer, employing a high-speed line camera (Basler) as a detector, capable of reading out 256 pixels at a speed of >200 kHz. This allowed to perform the measurement shot-to-shot at the full repetition rate of the system. Figure 4.3(d) shows a short-term RMS stability of 161 mrad. Measuring CEP fluctuations at such a high repetition rate enables a detailed analysis of the sources of CEP noise. In addition, it paves the way for the tagging of the CEP to reduce the noise in the sensitive data obtained later in the experiment.

4.1.3 Short-wave infrared OPCPA

The few-cycle, short-wave infrared OPCPA that was developed as a major part of this thesis work is based on several stages of nonlinear frequency conversion and parametric amplification. The system is entirely driven by the output of one of the rod-type fibers of the Yb CPA. We generate SWIR radiation in a DFG stage by mixing a fraction of the pump laser and the specially prepared visible pulse derived from the same pump. This approach, introduced by Homann *et al.*, produces passively CEP-stable idler pulses, which are ready to be amplified via OPA [22]. In our case, the DFG output is amplified in two consecutive non-collinear optical parametric amplification (NOPA) stages and then compressed with chirped mirrors and zinc sulfide wedges. Here, we outline the main parameters of the experimental setup, with more details given in **Paper I**.

Setup description

The optical layout of the SWIR OPCPA is sketched in Figure 4.4. Pulses coming from the rod-type amplifier are compressed by a transmission grating compressor to a duration of ~ 300 fs. The overall compressor efficiency is $\sim$ 90%, with pulses of 180 µJ energy after compression, corresponding to an average power of 36 W.

Approximately 36 µJ is split from the main beam to create a visible pulse with a spectrum spanning 630 - 750 nm. This is done in several steps. Firstly, the beam is further split by a ratio of 9:1, with the majority of pulse energy sent to a 1-mm-thick beta barium borate (BBO) crystal (cut at $\theta = 23.4°$) for SHG. About 17 µJ of pulse energy at 515 nm are obtained (53% conversion efficiency). The rest is tightly focused into a 4-mm-thick yttrium aluminum garnet (YAG) crystal for white-light generation (WLG). A typical supercontinuum spectrum is presented in Figure 4.5(a). The red part of the continuum is amplified to ~ 0.5 W average power in a visible NOPA stage (NOPA 1 in Figure 4.4) using a 4-mm-thick BBO (cut at $\theta = 23.6°$) as a nonlinear medium and the second harmonic beam as a pump. The internal non-collinear angle α is set to be approximately 2°, and the amplified spectrum is shown in Figure 4.5(b).

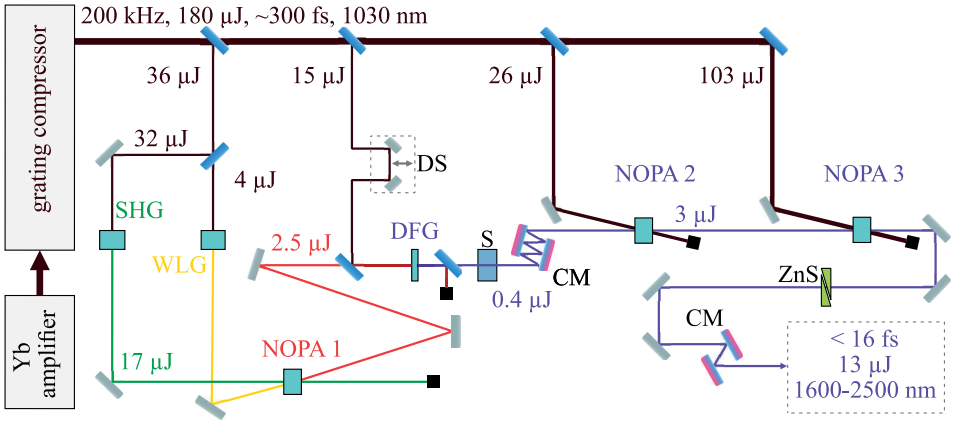

Figure 4.4: A schematic of the few-cycle SWIR OPCPA light source. DS - piezo-driven delay stage, S - sapphire, CM - chirped mirrors, ZnS - zinc sulfide.

The amplified continuum is sent to another BBO crystal (1-mm-thick, $\theta = 20.5°$), where it is collinearly combined with a fraction (15 µJ) of the fundamental 1030 nm pulse in a DFG stage. The idler wave from this interaction spans the spectral range between 1.6 and 2.5 µm [Figure 4.5(c)], with a typical pulse energy of ~ 0.4 µJ. The spectrum supports a Fourier-limited pulse duration of <14 fs, which corresponds to 2.2 oscillations at 2 µm central wavelength.

After the DFG, the SWIR pulses are amplified in two consecutive NOPA stages (NOPA 2 and 3 in Figure 4.4). Here, we use two crystals of bismuth triborate, commonly known as BiBO. The first stage amplifies the SWIR seed to approximately 3 µJ of energy in a 4-mm-thick crystal. In order to phase match the amplification process, we use the crystal in the XZ principal plane cut at $\theta = 7.3°$. A typical spectrum from this stage is shown in green in Figure 4.5(d). Afterwards, the output from the first amplification stage is refocused in another BiBO crystal (3 mm, XZ plane at $\theta = 7.8°$) and amplified to ~ 13 µJ (2.6 W average power), with a spectrum shifted slightly towards longer wavelengths [purple curve in Figure 4.5(d)]. Both stages use a small non-collinear angle (~ 0.5 - $0.7°$) to separate the spectrally overlapping idler and signal beams after amplification.

Dispersion compensation

To obtain the shortest pulses from the amplifier, it is essential to carefully characterize and compensate for the dispersion in the setup. The residual group delay dispersion in the SWIR spectral range can be removed by propagation through materials, using combinations of media with positive and negative GDD values. It is also possible to pre-chirp the

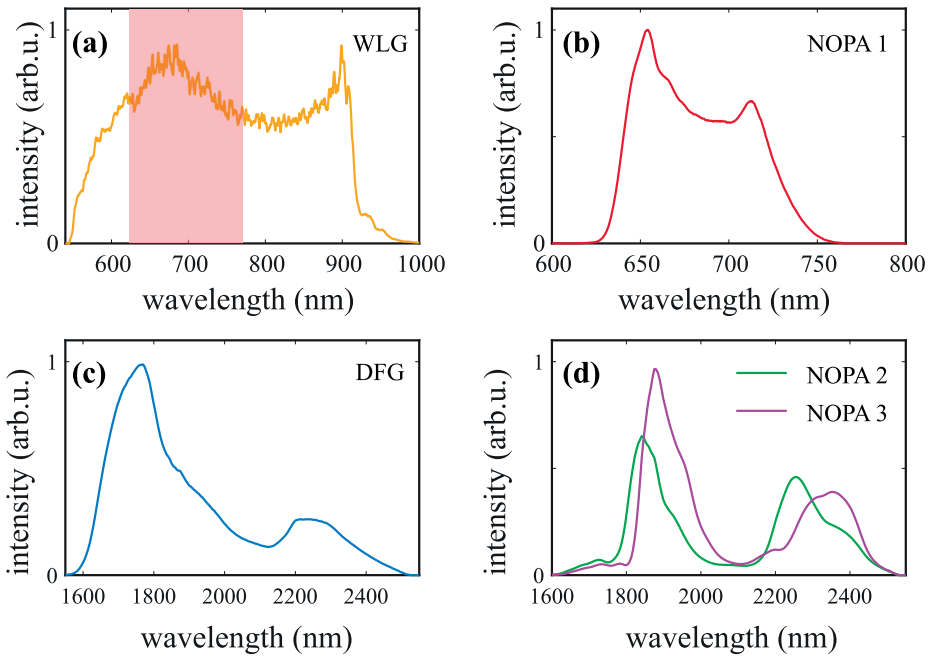

Figure 4.5: Spectra of different stages of the SWIR setup. (a) Output spectrum of the YAG-based WLG stage. The target amplification spectral range is shaded in red. (b) Output spectrum of the BBO-based visible NOPA (NOPA 1) stage. (c) Output spectrum of the BBO-based DFG stage. (d) The output spectra of the two BiBO-based NOPA (NOPA 2 and NOPA 3) stages.

visible NOPA output and then use ordinary glass with anomalous dispersion to compress the SWIR pulse, an approach taken, e.g., by Neuhaus *et al.* [22]. In our case, we use a combination of anti-reflection-coated sapphire plates and zinc sulfide (ZnS) glass wedges to compensate for the second-order phase, and their respective GDD contributions are depicted in Figure 4.6(a). We chose ZnS as a wedge material due to a moderately large positive GDD and favorable GDD/TOD ratio. It should be noted, however, that due to the large nonlinearity of zinc-based compounds (especially ZnSe), large beam sizes have to be used to avoid parasitic nonlinear interactions during propagation.

For spectra with bandwidths supporting few-cycle pulses, it is not enough to only compensate for the GDD. Higher-order phase terms, e.g., TOD, significantly influence the shape and duration of the intensity profile and thus have to be corrected. Unfortunately, there are no naturally-occurring materials with negative TOD in the near- or short-wave infrared[1]. Thus, we implement custom-made TOD-compensating chirped mirrors (Ul-

[1]To the author's knowledge.

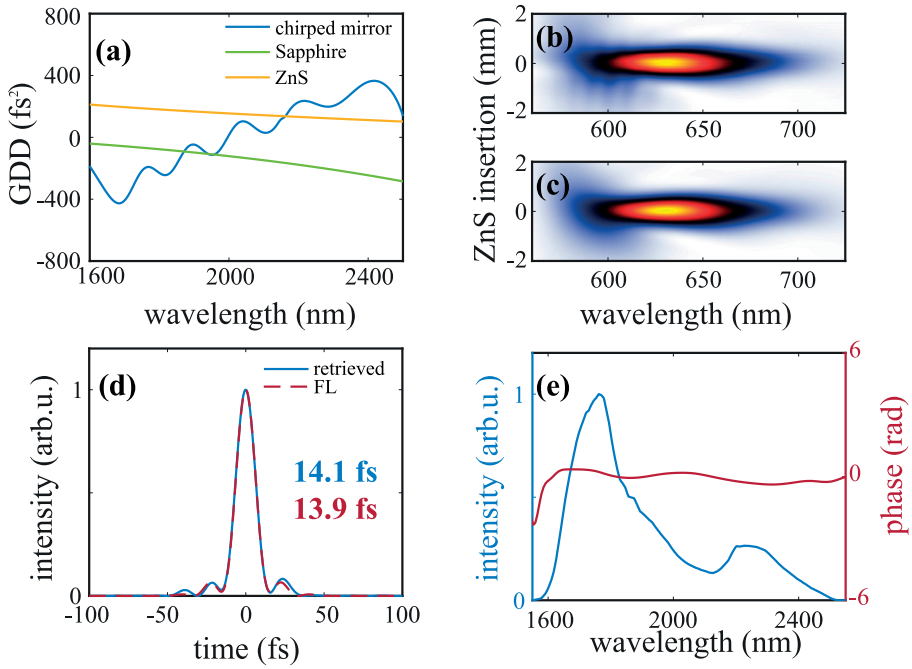

Figure 4.6: (a) GDD curves of TOD-compensating mirrors (Ultrafast Innovations TOD2102, 1 bounce), 1 mm Sapphire, and 1 mm ZnS. (b) Measured and (c) retrieved THG d-scan traces of the DFG output. (d) Temporal intensity profiles of retrieved and Fourier-limited pulses. The pulse duration is given at FWHM and the temporal profiles are normalized to 1. (e) Measured spectrum and retrieved spectral phase.

trafast Innovations), with the GDD curve shown in Figure 4.6(a). The mirrors have a positive GDD slope with increasing wavelength and remove 2000 fs^3 per reflection over the wavelength range of 1.6 - 2.5 µm.

We test the performance of the TOD-compensating mirrors by performing a third harmonic generation (THG) d-scan directly on the idler beam after the DFG. The measured and retrieved traces are shown in Figures 4.6(b) and (c), respectively. By adjusting the number of bounces on the chirped mirrors and material insertion, we are able to compress the pulses almost to the Fourier limit, confirmed by the nearly flat retrieved spectral phase, shown in Figure 4.6(e). This measurement also allows us to quantify and adjust the amount of residual chirp contained in the idler. Our estimates suggest that the pulse contains approximately 500 fs^2 of GDD and 4100 fs^3 of TOD after the dichroic filter. We apply $-1100\,\mathrm{fs}^2$ and $-5000\,\mathrm{fs}^3$ (7 mm of Sapphire and 4 bounces on the TOD mirrors)

in order to negatively chirp the pulses before amplification. Here, the negative chirp is beneficial as it ensures the absence of pulse compression in the BiBOs, which in turn helps avoiding large parasitic frequency conversion in the crystals.

Output pulse characterization

After amplification, the pulses are compressed to the final duration of ~ 15.8 fs (see d-scan measurement in Figure 4.7) by adjusting the insertion of ZnS wedges and adding two additional reflections from the chirped mirrors. Even though we have gained almost 2 fs in the pulse duration (compared to the DFG), the number of cycles under the intensity envelope increased only by a marginal amount (to 2.3 cycles). This can be explained by the shift of the central wavelength mentioned above. The retrieved pulse is similar in duration to the Fourier-limited case [Figure 4.7(d)], with the main differences appearing in the height of pre- and post-pulses.

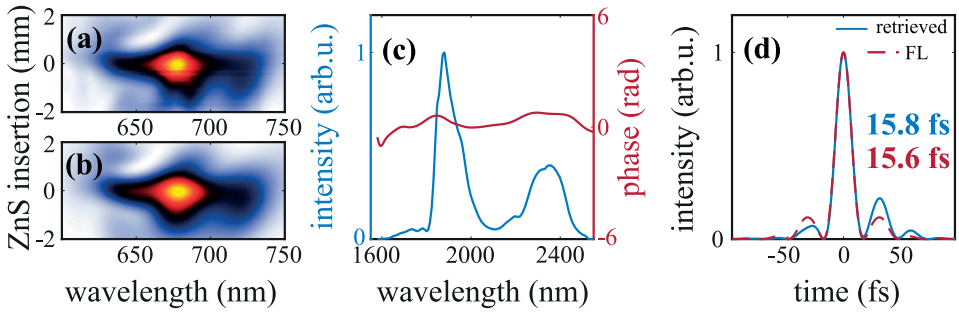

Figure 4.7: (a) Measured and (b) retrieved THG d-scan traces of the amplified output. (c) Measured spectrum and retrieved spectral phase. (d) Retrieved pulse intensity profile and Fourier-limited pulse of the spectrum in (c). The pulse duration is given at FWHM and the temporal profiles are normalized to 1.

We also determine the power and CEP stability of our SWIR light source. In Figure 4.8(a), a measurement of the average power stability is shown. The data is acquired with a thermal power meter at a rate of 1 Hz and demonstrates excellent stability with power fluctuations not higher than 0.3% RMS. The CEP fluctuations are measured with a monolithic interferometer, introduced in the previous chapter. In this measurement, we focus a small fraction of the output energy (~ 250 nJ) into a 5-mm-thick BBO crystal. By adjusting the crystal angle and orientation, we find spectral interference fringes in the $620 - 670$ nm wavelength region. First, we confirm their CEP sensitivity by changing the position of the piezo delay stage in the 1030 nm arm of the DFG. We record the spectrum of the fringes over 10 minutes (with a 1.5 ms spectrometer integration time, Figure 4.8(b)) and find a CEP stability equal to approximately 255 mrad [Figure 4.8(c)], in good agreement

with a separate measurement with a standard f - $2f$ interferometer (RMS = 290 mrad, not shown).

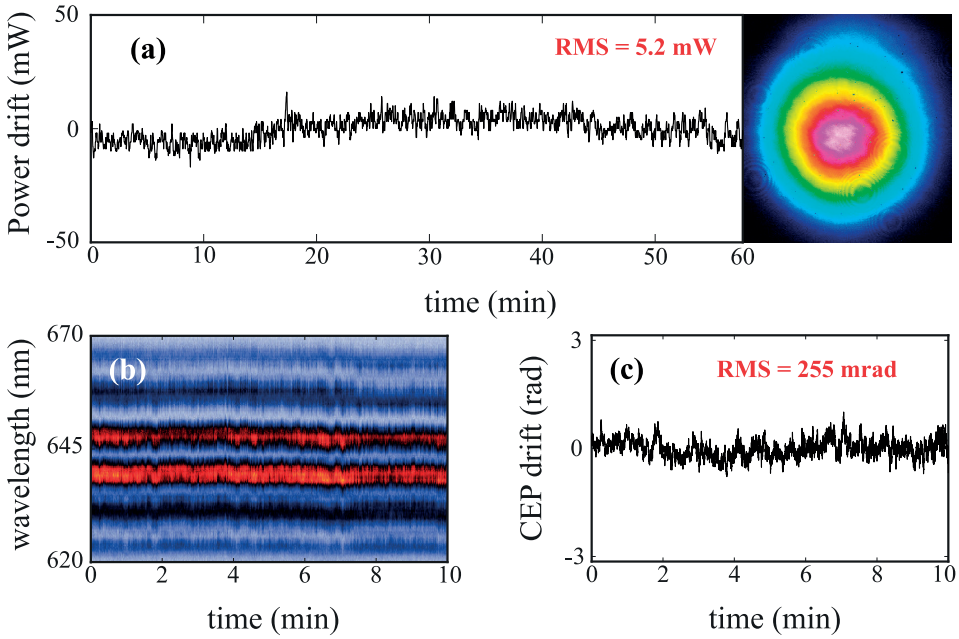

Figure 4.8: (a) Average power stability measurement of the amplified output. To the right: a two-photon absorption image of the SWIR beam profile, recorded 1 m away from the final amplification stage. (b) CEP stability interferogram recorded with a monolithic spectral interferometry scheme. (c) CEP drift as a function of time.

4.2 Post-compression of Ytterbium lasers with multipass cells

Nonlinear pulse compression with multipass cells (MPCs) has recently emerged as an efficient way of reducing the duration of laser pulses, achieving high throughput ratios and preserving good quality of the beam [17]. The basic concept of this technique is to couple the laser pulse into a cavity comprised of two concave mirrors with a Kerr medium in between (Figure 4.9). Since the cell is, in essence, an optical cavity, the transverse mode of the laser beam needs to be mode-matched (usually with a lens telescope) to the eigenmode of the MPC. The pulse travels back and forth in the cell and acquires a nonlinear phase shift at each pass, leading to spectral broadening through self-phase modulation. The total B-integral (i.e., the nonlinear phase) can be adjusted by changing the number of passes in the cell. The pulse emerges with a broadened spectrum and a chirp, and if the latter is removed (e.g., via a chirped mirror compressor), the resulting pulse duration decreases.

One of the essential parameters in designing an MPC-based compressor is the choice of the nonlinear medium, which mainly depends on the incoming peak power of the laser pulse. For mJ-level systems, noble gases are attractive candidates due to their low nonlinear refractive index, no losses at the interface, and immunity to optical damage. Furthermore, the use of gas offers the ability to tune the effective nonlinearity in the cell by simply changing the gas pressure. On the other hand, at reduced input peak powers, corresponding to lower pulse energies, solid-state-based MPCs are typically used, employing, e.g., thin plates of fused silica. In this case, the MPC approach is very similar in spirit to the multiple-plate post-compression technique [100], with the main difference being a smaller B-integral per pass [101], allowing to suppress beam degradation caused by self-focusing [102].

In the following, we present a brief overview of post-compression results obtained with two different Yb laser amplifiers, using gas- and bulk-based MPCs. The first system, set up at the FLASH2 pump-probe laser at DESY, is a multi-stage, gas-filled MPC compressor of a high-power slab amplifier. By using two consecutive cells filled with krypton gas, we manage to bring the pulse duration from nearly one picosecond down to 4 optical cycles (13 fs), and the details are presented in **Paper III**. The second system, described in **Paper IV**, is a compact, solid-state MPC in Lund that is used for compression of the same Yb rod-type amplifier that pumps the OPCPAs described earlier. We achieve a stable and efficient operation at the highest input and output powers (370 MW and 2.5 GW, respectively) reported to date for bulk MPCs, to the best of our knowledge. The pulse duration is reduced from 300 fs down to 31 fs.

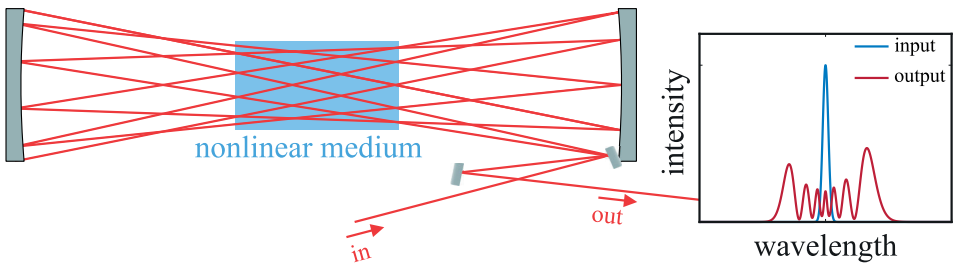

Figure 4.9: The concept of spectral broadening using a multipass cell. The pulse is coupled into a cavity comprised of two concave mirrors and makes several passes through a nonlinear medium to acquire a nonlinear phase shift.

4.2.1 Multistage gas-based MPC

The experimental setup is schematically depicted in Figure 4.10. The input to the system is an Yb Innoslab amplifier that produces 1.2 ps pulses with an energy of 2 mJ. The laser is operated in burst mode at the rate of 10 Hz, with a short 100 kHz-repetition-rate pulse train contained within a single burst. The beam is mode-matched to the eigenmode of

the first MPC via a lens telescope and coupled into the cavity with a small pickoff mirror located close to the edge of one of the curved mirrors. This MPC is filled with krypton at the pressure of 0.9 bar and contains two dielectric concave mirrors with 1 m radius of curvature (ROC). After 44 passes, the beam is coupled out using the same pickoff mirror as for in-coupling. We collimate the beam and send it to a chirped mirror compressor. The transmission of the cell is approximately 80 % including the compressor, with the output pulse energy equal to 1.6 mJ.

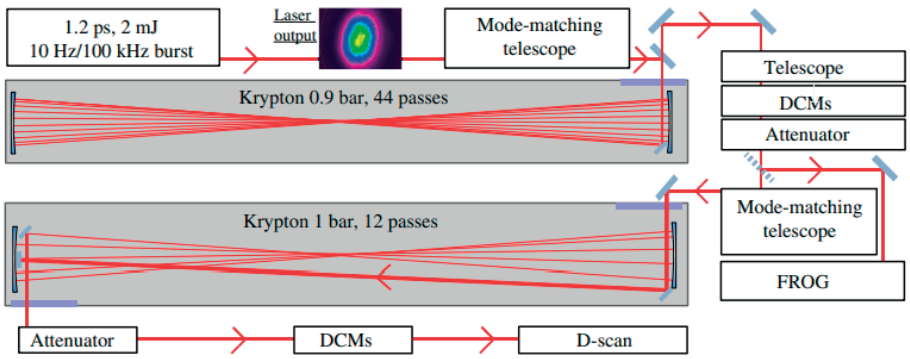

Figure 4.10: Schematic of the multi-stage, gas-based MPC post-compression system. The length of each cell is slightly less than 2 m. Figure adapted from **Paper III**.

The output spectrum of the first cell is shown in blue in Figure 4.11(a). The spectrum is significantly broader compared to the input (gray line) and supports a Fourier-limited pulse width of 30 fs. The amount of broadening achievable in this stage is limited by the bandwidth of the dielectric mirrors used in the cell. In order to analyze the pulse duration after the compressor, we employ SHG FROG as characterization technique. During the experiment, we measured and retrieved FROG traces with different numbers of reflections in the chirped mirror compressor and found that the optimal compression is achieved with 32 bounces (corresponding to a total GDD of $-2600\,\mathrm{fs}^2$) on the mirrors. In this configuration, the retrieved pulse duration is 32 fs FWHM [Figure 4.11(b)], and the corresponding measured FROG trace is shown in Figure 4.11(c). The decrease in duration from 1.2 ps to 32 fs corresponds to a single-stage compression factor of 37.5, still the highest reported to date. The cell preserves a good beam quality with a focused beam profile shown to the right of Figure 4.11(d).

To reach the few-cycle regime, the pulse bandwidth has to be increased further. Thus, we implemented a second MPC based on two concave enhanced silver mirrors (1 m ROC) filled with krypton at the pressure of 1 bar. The beam is coupled in and out of the cell via separate mirrors located on opposite sides of the cavity and makes 12 passes before the outcoupling. We observe the onset of optical damage on the mirror surfaces with input

energies >1 mJ, and thus we attenuate the incoming pulse energy to about 0.8 mJ to avoid further damage. The efficiency of this stage is 46 %, resulting in 0.37 mJ of energy in the output pulse, with a limiting factor being reflection losses on the silver mirrors.

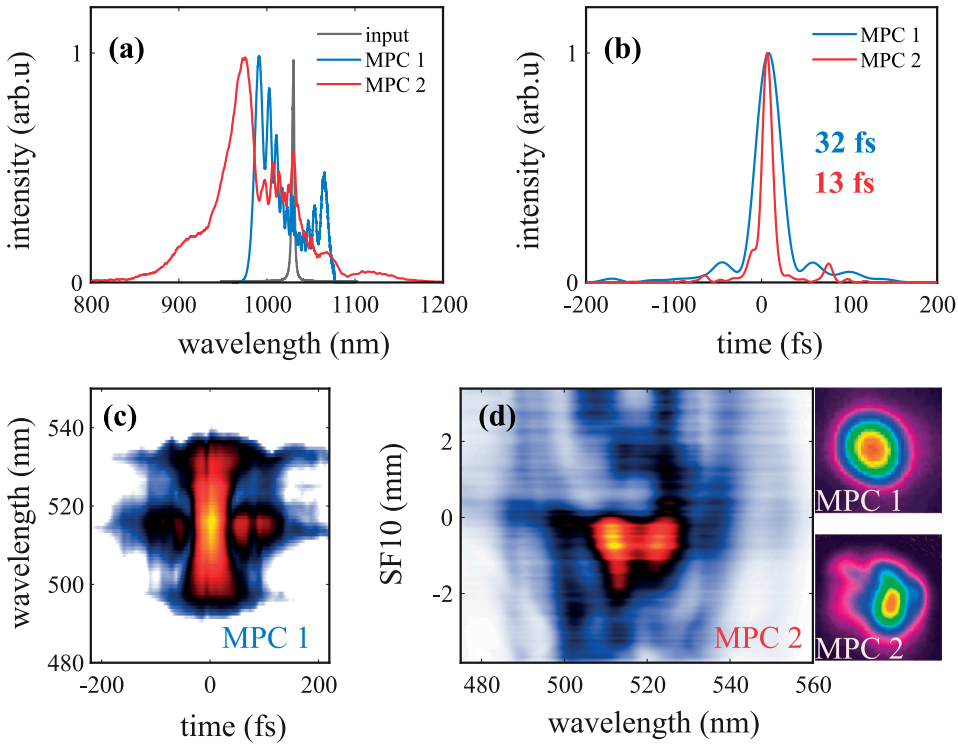

Figure 4.11: Multi-stage, gas-based MPC post-compression results. (a) Measured spectra of the laser and the first and second MPC output. (b) Retrieved pulse intensity profiles. (c) Measured SHG FROG trace of the output of first cell (logarithmic scale). (d) Measured SHG d-scan trace of the output of the second cell (linear scale). To the right: spatial intensity profiles of the focused beam after MPC 1 and 2, respectively.

The measured spectrum of the second cell output is shown in red in Figure 4.11(a), supporting a 10.8 fs Fourier-limited pulse. To compress the pulses and measure their duration, we only use a surface reflection of a glass wedge located at the exit of the MPC. This ensures no additional nonlinear propagation effects in air, as they could potentially influence the measurement results. The pulses are compressed in another chirped mirror compressor with a GDD contribution of $-1900\,\mathrm{fs}^2$. Here, we characterize the pulses via an SHG d-scan, and the measured d-scan trace is shown in Figure 4.11(d). The retrieval indicates an output pulse duration of approximately 13 fs [Figure 4.11(b)], which corresponds to slightly less than 4 optical cycles under the intensity profile at λ_0 = 1030 nm. The measurement of the spatial beam profile reveals a reduced beam quality, with possible reasons being the deformation

of the silver mirrors due to heating or the onset of unwanted nonlinear propagation effects in the optical elements (e.g., multipass cell windows).

4.2.2 Single stage bulk-based MPC

The optical layout of the bulk MPC post-compressor is sketched in Figure 4.12. The pulses from one of the rod-type amplifiers introduced in section 4.1.1 are compressed to a duration of 300 fs in a transmission grating compressor, with 170 µJ available after compression. The laser beam is mode-matched to the MPC by a lens telescope and is coupled into the cavity via a scraper mirror. The MPC consists of two dielectric mirrors with a ROC of 300 mm placed 500 mm apart from each other, and two 1-mm-thick antireflection-coated fused silica plates. The plates are spaced by 150 mm and are placed on either side of the center of the cell. We can vary the total B-integral (and thus the amount of broadening) acquired in the cell by moving the plates closer to or further from the foci. After 15 passes, the beam is coupled out of the cell using the same scraper mirror with a different angle of incidence. The pulse is then sent to a chirped mirror compressor, where approximately 2800 fs^2 of GDD are removed. After the compressor, the output power is about 30 W (150 µJ), corresponding to an overall efficiency of 88%. The reflection from a glass wedge is used to perform extensive spatial and temporal diagnostics, discussed in the following.

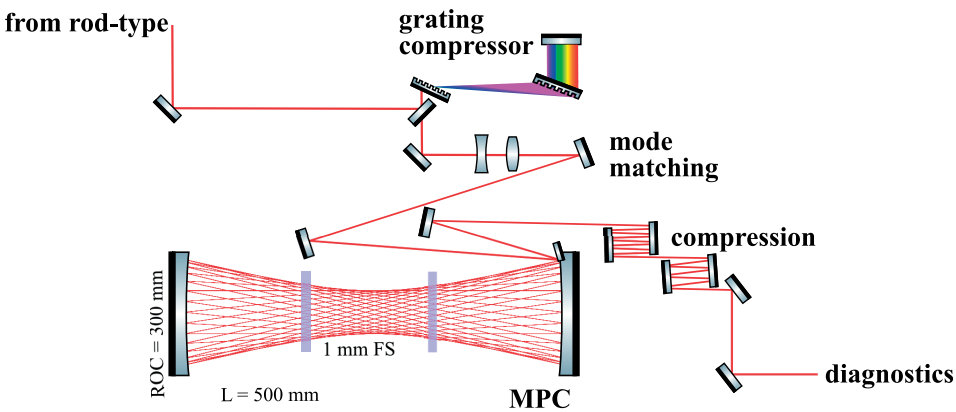

Figure 4.12: Layout of the single-stage bulk MPC post-compression setup. The length of the cavity is about 0.5 m.

The measured spectrum of the MPC output is shown in Figure 4.13(a), supporting a Fourier-limited temporal width of 30 fs. To obtain the information about the compressed pulse duration, we perform SHG FROG. The measured trace is shown in Figure 4.13(b), with the retrieval result plotted in Figure 4.13(c). The retrieved pulse duration is 31 fs, almost an order of magnitude shorter (compression ratio = 9.7), when compared to the input pulse.

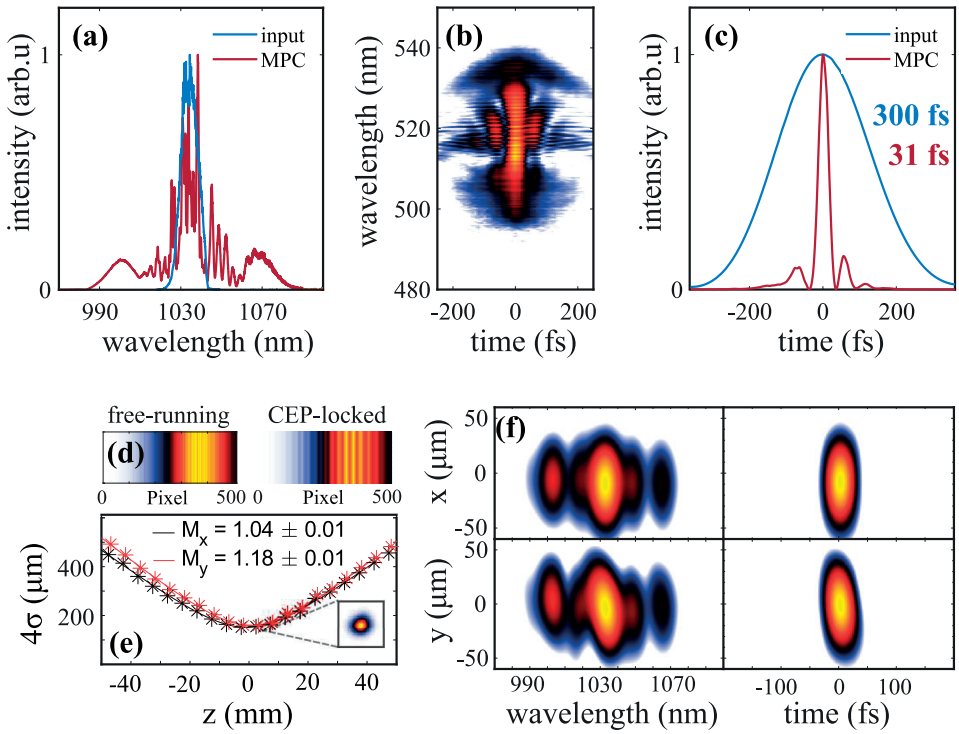

Figure 4.13: Single-stage, bulk-based MPC post-compression results. (a) Measured spectra of the input pulse and the MPC output. (b) Measured SHG FROG trace of the MPC output, plotted in logarithmic scale. (c) Retrieved temporal intensity profiles of the input and output pulses. (d) Spectral fringes from an f-$2f$ interferometer in the case of a free-running (left) and CEP-stabilized (right) oscillator. (e) M^2 of the compressed output, inset: spatial beam profile in the focus. (e) Spatio-temporal couplings measurement of the output.

Approximately 77% of the total pulse energy is confined to the main peak, while the rest is distributed over pre- and post-pulses located up to 1 ps away.

The compressed output showed an excellent long-term average power stability. We measure the average power over 1 hour with a 10 Hz sampling rate and found RMS power fluctuations of 0.32%, comparable to those of the input (0.27%). Furthermore, since the front-end oscillator can be CEP-stabilized, we study the short-term CEP stability of the source, which can be crucial in driving strong-field processes (if an additional compression stage to the few-cycle regime is added). We measure the CEP fluctuations with a standard f-$2f$ interferometer and record the spectral fringes in single-shot using the same high-speed line camera as before (Section 4.1.2). The results are shown in Figure 4.13(d). It is possible to distinguish between two regimes, the free-running oscillator (left panel) and the

locked one (right). In the latter case, the CEP fringes are visible, indicating that the CEP is somewhat preserved through the whole fiber amplifier chain and the MPC itself, albeit the fringe contrast is low[2].

Complementary to the spectral and temporal measurements, we also determine the output beam quality in the spatial domain. First, we characterize the focusability of the compressed beam by performing an M^2 measurement, with the results summarized in Figure 4.13(e). The values obtained for the MPC output (1.04 and 1.18 for x and y dimensions, respectively) are almost identical when compared to that of the input (1.04 and 1.17), and no significant changes were observed.

This MPC operates at an input power of 370 MW, which exceeds the critical power for self-focusing in fused silica by more than 80 times. This condition can potentially cause unwanted nonlinear propagation effects, resulting in the appearance of spatio-temporal couplings. To address these concerns, we perform a 3D characterization based on spatially-resolved Fourier transform spectrometry [103]. Combined with the previous FROG pulse measurement, we can reconstruct a complete 3D profile of the pulse, and the results are shown in Figure 4.13(f). In the spatio-spectral domain (left panel), the spectrum is spatially homogeneous along the x-dimension; however, spatial chirp is observed in the y-dimension, translating into an apparent pulse-front tilt in the spatio-temporal domain (right panel). The spatial chirp likely originates from a slight misalignment of the grating compressor before the MPC, as similar behavior is observed for the input beam. Even with the presence of the spatial chirp, the calculated temporal 3D Strehl ratio is found to be equal to 0.80, indicating good spatio-temporal localization of the pulse when focused.

[2]The Yb fiber CPA is not designed to be phase-stable. This result is purely due to the CEP stability of the Ti:Sapphire oscillator.

Chapter 5

Applications

Excellent temporal resolution and large peak intensities provided by few-optical-cycle pulses enable a plethora of applications within ultrafast processes and strong-field light-matter interaction. This chapter provides a summary of several applications of few-cycle pulses that were explored during this thesis work. We start with a discussion of the process of high-order harmonic generation (HHG) and cover its main properties, e.g., electron trajectories, maximum photon energy scaling, pulse structure in the time domain, and macroscopic phase matching effects. We then present the experimental beamline that is used to generate high-order harmonics with the NIR-, and later with the SWIR OPCPA light sources. Secondly, we use short attosecond pulse trains generated from the NIR OPCPA together with the same infrared laser to perform XUV-IR pump-probe experiments in helium (**Paper II**). Finally, we show how 2.4-cycle pulses from the NIR OPCPA can be used to drive coherent electric currents in semiconductors (**Paper VI**).

5.1 High-order harmonic generation

The phenomenon of high-order harmonic generation in gases was first observed in 1987-1988 [7, 8] in the context of studying the properties of fluorescence emission from noble gases. By focusing an intense laser pulse into a gas target, a comb of odd-order harmonics of the driving laser frequency was generated with a rather surprising outcome: after an initial exponential decline of conversion efficiency with increasing harmonic order, a long plateau of harmonic peaks with similar amplitudes was discerned, followed by an abrupt cutoff. Such a result could not be explained by standard perturbation-based methods of nonlinear optics and required a non-perturbative treatment. The first approach was to solve numerically the time-dependent Schrödinger equation [104]. It was followed by the semi-

classical or the three-step model, proposed by Kulander *et al.* [105] and Corkum [18] in 1993. A year later, a fully quantum-mechanical description of the HHG process was presented by Lewenstein *et al.*, the so-called strong-field approximation (SFA) [106]. Here, we use the semi-classical approach to discuss the main features of the harmonic emission, and SFA to simulate the process of two-color, XUV-IR photoionization of helium.

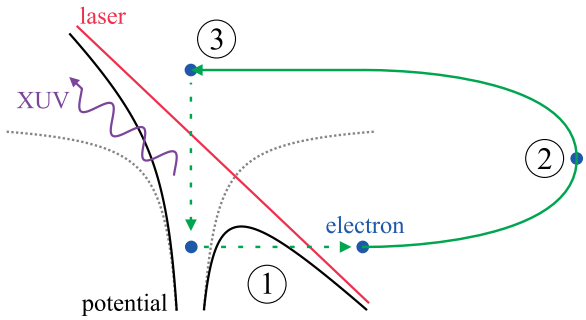

Figure 5.1: Three-step model of HHG: (1) - tunneling ionization. (2) - acceleration in the continuum. (3) - recombination.

Just a few years after the discovery of HHG, it was proposed that a repeating harmonic structure in the frequency domain (i.e. the harmonic comb) could be a product of the repeating structure in the time domain (i.e. the pulse train) [107, 108], akin to the trains of pulses from ultrafast mode-locked lasers emitting optical frequency combs. Furthermore, the broad bandwidth of the harmonic radiation would imply that the pulses in the train would have sub-femtosecond (or attosecond) duration [9, 109], subject to the condition that the harmonics have a fixed phase relationship between each other. This condition, and thus the first experimental proof of attosecond pulse train (APT) was observed in 2001 by Paul and co-workers [110], and the first isolated attosecond pulses generated by extremely short infrared pulses were demonstrated shortly after [111]. If HHG is driven by a $2-3$-cycle-long pulse, the harmonic emission will take the form of a short train of pulses in the time domain, with its structure being heavily dependent on the CEP of the driving pulse. We discuss this in more detail in the following section.

5.1.1 Semi-classical model

Within the framework of the semi-classical model, the process of HHG in rare gases can be described in three distinct steps, illustrated in Figure 5.1. The electric field of the laser pulse is strong enough to distort the Coulomb potential of the atom, such that a valence electron can be ejected into the continuum by the process of tunneling ionization (step 1). The now-free electron is accelerated away from the core, and as the field changes sign, is

driven back to the parent ion (step 2). Finally, when close to the ion, it may recombine with the latter, emitting a burst of electromagnetic radiation with wavelengths typically in the XUV or soft-X-ray range.

The "classical" part of this model comes from the fact that the trajectory of an electron during its acceleration in the continuum is calculated using simple Newtonian mechanics. The Coulomb force imparts an acceleration to the electron according to Newton's second law:

$$m_e \frac{d^2x}{dt^2} = eE_0 \sin(\omega t), \tag{5.1}$$

where m_e and e are the mass and the charge of the electron, respectively, E_0 is the amplitude of the field, and ω is the angular frequency. By choosing an initial conditions $x(t_i) = 0$ and $v(t_i) = 0$, we integrate Eq. 5.1 and find expressions for the electron velocity and position as a function of time:

$$v(t) = \frac{eE_0}{m_e\omega}[\cos(\omega t) - \cos(\omega t_i)], \tag{5.2a}$$

$$x(t) = \frac{eE_0}{m_e\omega^2}[\sin(\omega t) - \sin(\omega t_i) - (\omega t - \omega t_i)\cos(\omega t_i)]. \tag{5.2b}$$

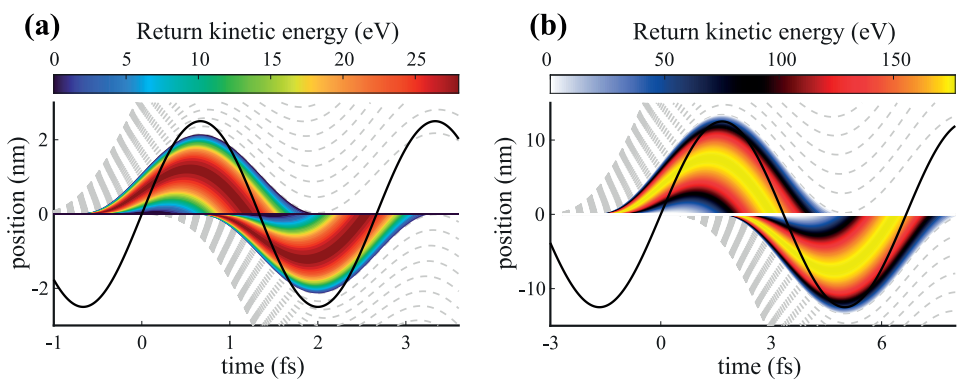

Figure 5.2: Classical electron trajectories in HHG driven by 850 nm (a) and 2 µm (b) fields. Gray dashed lines indicate trajectories that do not return to the core. The color bars denote the electron's kinetic energy at the return to the parent ion.

The analysis of Eq. 5.2b leads us to several conclusions. The general shape of the electron trajectory strongly depends on the ionization (or tunneling) time t_i. For certain values of t_i, the electric field of the laser will simply drive the electron away from the ion. However, if the

atom is ionized during a quarter-cycle after the peak of the field, the electron will be driven back ($x = 0$) and potentially recombine with the ion, contributing to HHG. The electron trajectories leading to the photon emission are plotted for two driving wavelengths, 850 nm and 2 µm [Figures 5.2(a) and 5.2(b), respectively] at the laser intensity of $1.5\times10^{14}\,\mathrm{W/cm^2}$. It is evident, both from the figure and Eq. 5.2b, that increasing wavelength (decreasing ω) results in larger excursions, e.g., exceeding 10 nm for the 2 µm driver.

When an electron is accelerated by the laser field, it gains kinetic energy. Its value E_{kin} at the time of recombination t_r is given by:

$$E_{\mathrm{kin}} = \frac{1}{2} m_e v^2(t_r) = 2U_p[\cos(\omega t_r) - \cos(\omega t_i)]^2, \tag{5.3}$$

where $U_p = e^2E_0^2/4m_e\omega^2$ is called the ponderomotive energy. From Figure 5.2, we can see that the different trajectories can lead to the same values of return energy, and are usually divided into two categories, named *short* and *long*. Electrons that take long trajectories are ionized earlier and recombine at later times compared to the electrons that follow short trajectories. Even though both trajectories lead to the same photon energies, in practice, it is favourable to optimize the generation conditions for the short trajectories as they possess significantly smaller spatial divergence [112], desirable in many experiments.

The maximum value of E_{kin} is approximately equal to $3.17U_p$, resulting in a simple expression for the highest photon energy emitted in the HHG process, the so-called harmonic cutoff law:

$$E_{\mathrm{cutoff}} = I_p + 3.17U_p = I_p + 3.17\frac{e^2}{8\pi^2 m_e \epsilon_0 c^3}\lambda^2 I \tag{5.4}$$

Here, I_p is the ionization potential of the neutral atom, and $I = c\epsilon_0 E_0^2/2$ is the peak intensity of the driver. In theory, it is possible to increase the cutoff energy by increasing the incoming light intensity. However, in practice, too high intensity will quickly lead to a strong ionization of the gas medium, which can reduce the efficiency of the generation process [113]. A more elegant way is to exploit the λ^2 scaling of the kinetic energy: in Figure 5.2 the color maps indicate electron return energies, showing a significant increase in E_{kin} for the 2 µm pulse. The caveat of this strategy, however, is a decreased yield of HHG, which scales highly unfavourably with λ [19, 20, 114][1].

The 3-step process described above occurs periodically, emitting a pulse every half-cycle of

[1] This is usually attributed to the fact that the longer the time the electron spends in the continuum, the smaller is the overlap integral of the wave functions of continuum and ground-state electron wave packets. Hence, the probability of recollision and, thus, the yield are drastically reduced with larger excursions.

the driving laser. The total XUV field produced by a single infrared pulse can be obtained by coherently adding individual pulses in the frequency domain:

$$E(\Omega) = \sum_m |E_m(\Omega)| \exp[i(t_m\Omega + \phi(\Omega) + m\pi)] \tag{5.5}$$

Here, Ω is the frequency, $|E_m(\Omega)|$ is the spectral amplitude of an XUV pulse generated in the m-th half-cycle with a starting time t_m. The $m\pi$ phase shift emerges from the sign flip of the driving field, and $\phi(\Omega)$ is a quantity known as the dipole phase, originating from electron propagation in the continuum. Within the semi-classical model, this phase can be approximated by an analytical expression [115], and for the short trajectories we write it as follows:

$$\phi(\Omega) = t_{ps}(\Omega - \Omega_p) + \frac{\gamma}{I}(\Omega - \Omega_p)^2, \tag{5.6}$$

where t_{ps} is a threshold return time of the electron relative to the zero of the infrared field, and is approximately equal to 0.18τ (where τ is the duration of the laser cycle), Ω_p is the ionization potential, and γ is a proportionality constant[2]. The presence of a quadratic term in Eq. 5.6 indicates that the XUV emission is chirped, which is connected to the fact that different photon energies are emitted at different return times.

Equation 5.5 can be used to simulate an APT for an arbitrary input field. In Figure 5.3, we show two examples of simulated APTs in argon, calculated with Eq. 5.5, when driven by few-cycle Gaussian pulses with central wavelengths of 850 nm and 2 µm with varying values of CEP. The spectral amplitude $|E_m(\Omega)|$ of the XUV pulse, first assumed to span from the ionization potential to the cutoff with a super-Gaussian shape [115], is then weighted by the photoionization cross-section of argon in the outermost shell [116]. The integrated power spectrum of each pulse is presumed to vary with the laser intensity as the ionization rate, calculated with an Ammosov-Delone-Krainov model [117], and the phase is calculated according to Eq. 5.6.

From Figure 5.3(b) it is clear that, when driven by a few-cycle near-infrared pulse, the APT consists of only a few attosecond pulses, and its structure is heavily influenced by the CEP of the driving field. If the IR driver has a CEP value of 0 (i.e. the so-called "cosine" pulse), the XUV field mainly consists of three pulses, while for the CEP of $\pi/2$ (the "sine" pulse) there are two dominant bursts, with smaller pre- and post-pulses. Similar behaviour is observed for the case of a 16 fs SWIR pulse with a central wavelength of 2 µm [Figure 5.3(d)]. Even though the driver duration is almost three times longer, the number of cycles contributing

[2]A more general expression for the dipole phase, e.g., accounting for the long trajectories, as well as the calculation of γ can be found in [112].

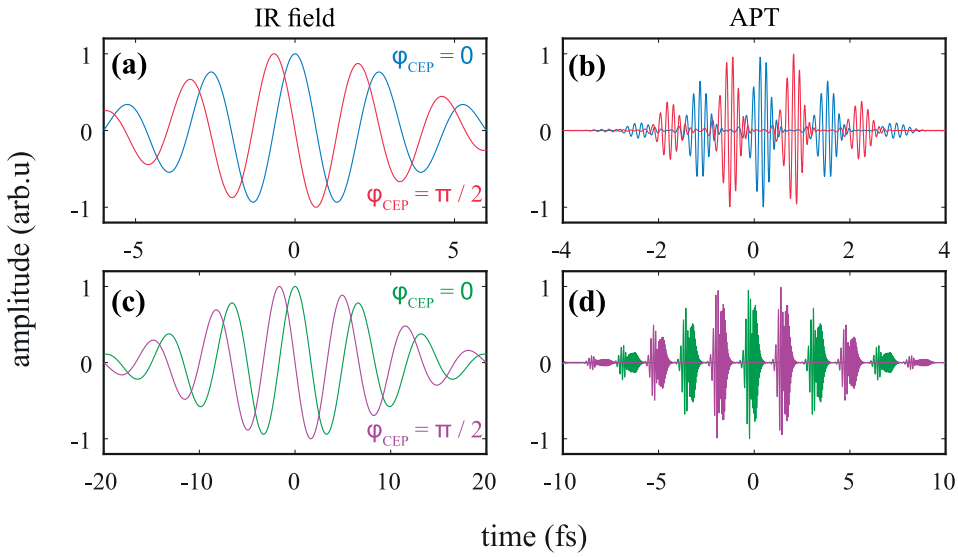

Figure 5.3: Infrared few-cycle drivers with different CEP values and their generated APTs, calculated with the multiple pulse interference model [115]. (a) A 6 fs Gaussian pulse centered at 850 nm and the corresponding APT (b). (c) A 16 fs Gaussian pulse centered at 2 µm and the corresponding APT (d).

to HHG is similar, resulting in a comparable profile of the APT. A significantly higher central frequency is also evident, originating from the extension of the HHG plateau to higher photon energies.

Knowledge of the temporal structure of the generated XUV emission is important, since the outcome of many photoionization-based measurements depends on the amount of pulses in the train and their relative amplitudes and phases, as will be shown below in the case of XUV-IR pump-probe spectroscopy experiments in Section 5.2.

5.1.2 Phase matching

The discussion so far was concerned with studying HHG properties on a single-atom level. Since the gas target is an ensemble of many atoms, the emission from different source points (atoms) must build up constructively for efficient HHG: phases of XUV light produced at different positions in the gas medium should interfere constructively, thus satisfying the phase matching condition. Here, we give a brief overview on the main origins of the phase mismatch in HHG, and we refer the interested reader to Refs. [118–121] for a more rigorous discussion.

The underlying physical concept in HHG phase matching is similar to the case of crystals, described in chapter 2. We seek to minimize the phase mismatch Δk, which consists of several terms:

$$\Delta k = \Delta k_e + \Delta k_g + \Delta k_n + \Delta k_d, \tag{5.7}$$

where Δk_e is the mismatch to due to the ionization of the gas [118, 119], Δk_g originates from the Gouy phase of the infrared beam, Δk_n accounts for the dispersion of the neutral gas, and Δk_d is due to the presence of the dipole phase. In experimental conditions, it is usually possible to vary these terms by adjusting (1) the incoming light intensity, (2) the position and the size of the focus, and (3) the pressure/geometry of the gas target.

Adjusting either of the three parameters influences several phase matching contributions in Eq. 5.7. Raising the light intensity increases the degree of ionization in the medium, affecting Δk_e and Δk_n. In order to reach the optimum phase matching, it is necessary to have a certain degree of ionization, however, too strong ionization can suppress the harmonic emission. Gases with high ionization potential (e.g. neon or helium) can sustain higher intensities, leading to a cutoff extension to higher photon energies, however the conversion efficiency is usually lower when compared to heavier species like argon or krypton.

The dipole phase contribution Δk_d varies strongly across the medium through its dependence on the laser intensity:

$$\Delta k_d = \frac{\partial \phi(\Omega)}{\partial z} \tag{5.8}$$

As the beam goes through the region of focus, $\partial \phi(\Omega)/\partial z$ changes the sign, and consequently, there is a sign flip of Δk_d, and since the dipole phase has different signs for short and long trajectories [112], it is not possible to compensate the phase mismatch for both trajectories simultaneously. Usually, one achieves phase matching for short trajectories by setting the laser beam focus slightly before the gas medium. The focusing geometry also determines the Gouy phase contribution Δk_g. The Gouy phase arises from propagation of a focused beam in space. The phase mismatch due to the Gouy phase is always negative and is inversely proportional to the Rayleigh length z_0. For the q-th harmonic, at the position of the waist, $\Delta k_g = -q/z_0$ [120].

Finally, adjusting the gas pressure influences Δk_e and Δk_n. These phase matching terms have opposite signs ($\Delta k_e < 0$ and $\Delta k_n > 0$) and scale linearly with gas density. The parameters of the gas target should be adjusted according to the focusing geometry. We can illustrate this by considering the generation process at the position of the laser focus, where the phase mismatch due to the dipole phase vanishes. The density ρ required for phase-

matched generation is [122]:

$$\rho = -\frac{\Delta k_g}{\Delta\kappa_n + \eta_e \Delta\kappa_e} = \frac{q}{z_0(\Delta\kappa_n + \eta_e \Delta\kappa_e)}, \tag{5.9}$$

where $\Delta\kappa_n = \Delta k_n/\rho$, $\Delta\kappa_e = \Delta k_e/\rho\eta_e$, with η_e being the degree of ionization. From Eq. 5.9, we conclude that tight focusing geometries (short z_0) require high pressure in the gas target. The medium length should be rather short to prevent re-absorption of the generated XUV radiation.

The considerations above play an important role in the design of the gas target for HHG driven by the few-cycle light sources described in the previous chapter. In the µJ pulse energy regime, a tight focusing and thus a high-density gas target are needed for efficient generation of the XUV/SXR light. In the following section, we briefly discuss the design of the high-pressure gas jet that was used to generate high harmonics with NIR and SWIR OPCPA systems.

5.1.3 The harmonic generation beamline

Within the scope of this thesis work, high-order harmonics were generated and analyzed in a compact XUV-IR interferometer vacuum chamber, featuring a high-pressure gas jet in the generation stage and an XUV spectrometer for output characterization. The experimental setup is schematically illustrated in Figure 5.4(a), and the more detailed discussion of the interferometer design is presented in **Paper II**.

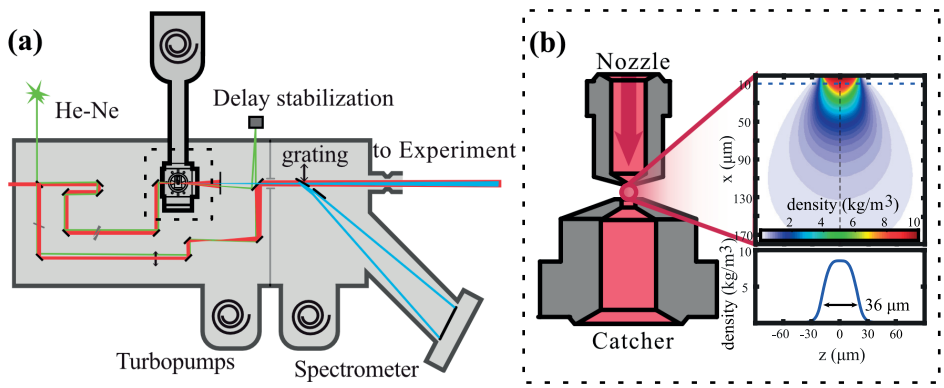

Figure 5.4: XUV-IR interferometer for HHG and pump-probe experiments. (a) Experimental setup. (b) Gas target design and simulated density profile in the interaction region. The dashed line indicates the position of the laser beam relative to the nozzle opening.

The infrared beam enters the chamber and is split into two arms. Approximately 80% of pulse energy is transmitted and used as the pump for XUV generation. The beam path of the pump consists of a piezo-driven delay stage for precise delay control and a pair of glass wedges for fine dispersion tuning. We focus the pump beam into a gas jet using an off-axis parabolic mirror with a focal length of 50 mm.

The generation of the XUV light is contained within a small cube placed inside the main vacuum chamber, pumped by a separate turbo pump. The design of the gas target is shown in Figure 5.4(b). It consists of a 40 µm-wide nozzle mounted on a 3D translation stage, and a gas catcher with a 1 mm opening, mounted at a distance <200 µm away from the nozzle. The optimum phase matching conditions in argon should correspond to a gas density of $8.8\,\mathrm{kg/m^3}$ ($\sim$ 5 bar pressure at standard conditions)[3] when driven by our NIR OPCPA with the focusing geometry described above. Comprehensive simulations using the described nozzle and catcher parameters for a backing pressure of 12 bar reveal a gas density of $8.5\,\mathrm{kg/m^3}$($\sim$ 4.8 bar of pressure) 10 µm away from the nozzle [see inset of Figure 5.4(b)]. The gas is evacuated through the catcher with a scroll vacuum pump in order to preserve good vacuum conditions in the interferometer chamber.

After the HHG, the residual infrared can be removed with metallic filters. The XUV is then sent to the experiment, or to an insertable gold mirror that diverts it towards a flat-field XUV spectrometer. The spectrometer consists of a concave diffraction grating (Hitachi $001-0640$) and a combination of a microchannel plate (MCP) and a phosphor screen as a detector. The grating refocuses the beam onto the detector, and the phosphor screen is imaged by a camera to obtain the XUV spectrum.

The remaining 20% of the IR is reflected by the beamsplitter to be used as a probe. A 1-mm-thick glass plate is introduced to match the dispersion of the arms. We introduce a focus in the probe beam with a lens at the location that matches the position of the interaction region (i.e the focus of the pump arm). The infrared and the HHG are recombined using a holey mirror, where the XUV is transmitted through a small hole in the center, while the IR is reflected from the rest of the mirror surface, and the two are sent to a toroidal mirror, which focuses both beams into the experiment.

To be able to perform sensitive pump-probe measurements with high temporal stability over many hours, it is essential to minimize the influence of vibrations and drift that would cause a timing jitter between the pump and the probe. We employ several means that help us to increase the temporal stability of the interferometer. Firstly, all optical components are mounted on a breadboard that is vibrationally decoupled from the vacuum chamber. This isolates the optical setup from vibrations caused by the vacuum pumps. Secondly, an active delay stabilization is implemented by sending a beam from a Helium-Neon (He-Ne)

[3] 1 bar of pressure corresponds to a density of $1.76\,\mathrm{kg/m^3}$ for argon at the standard temperature, i.e., 273 K.

laser through the interferometer arms and recording the spatial interference pattern with a CCD camera mounted outside the chamber. The drift of the fringes is recorded over time and a feedback signal is generated to control the delay stage in the pump arm. An overall short-term stability (over 10 seconds) of 26 as is achieved.

The experimental setup described above was mostly used with the NIR OPCPA as a driving source for HHG. Recently, we have tested the capabilities of the SWIR OPCPA by sending the beam into the same chamber for harmonic generation. In this case, we used all available pulse energy by coupling the beam into a separate input port of the vacuum chamber, and we estimate the gas density in the interaction region to $10.4\,\mathrm{kg/m^3}$(~ 5.9 bar of pressure) for 15 bar backing pressure. The results of this experiment are presented below.

5.1.4 Experimental results

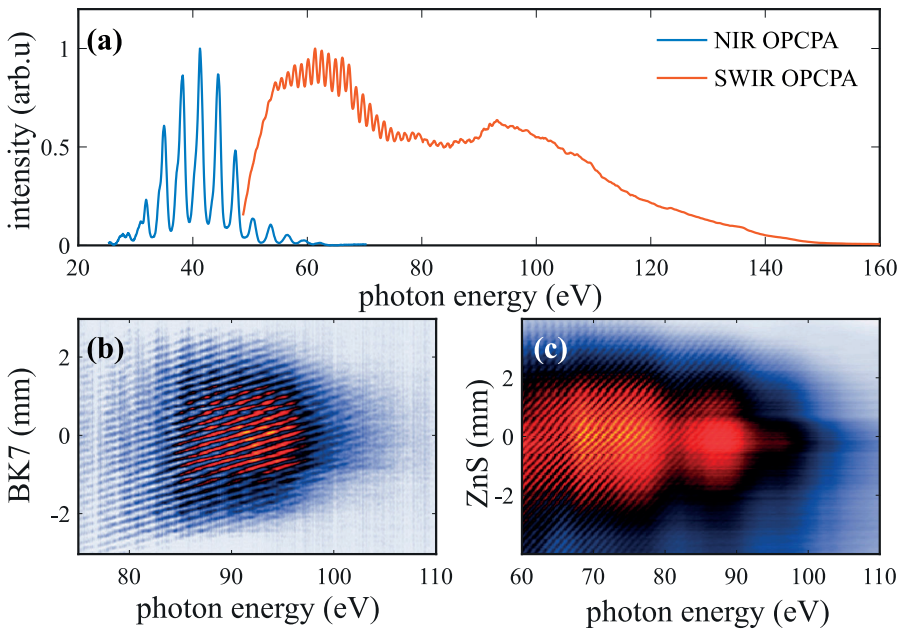

Figure 5.5: HHG results. (a) Typical measured HHG spectra in Ar for an 850 nm driver (blue) and 2 µm driving pulse (red). (b) HHG dispersion scan in Ne driven by 850 nm OPCPA. (c) HHG d-scan in Ar driven by 2 µm OPCPA.

Over the course of this thesis work, high harmonics were routinely produced with the near-infrared OPCPA, while for the SWIR light source only a proof-of-principle experiment was

carried out. In Figure 5.5(a), we show representative HHG spectra generated in argon with the two light sources. As expected, the HHG photon flux is significantly higher for the NIR driver, where lower MCP voltages (typically 1500 - 1600 V) and camera exposure times ($\approx$ 1 s) were used to acquire the spectrum. In comparison, up to 1750 V and 10 - 20 s exposures to obtain good signal-to-noise ratio (SNR) in the case of HHG spectra driven by SWIR pulses. The cutoff extension due to the λ^2-scaling of ponderomotive energy is evident, with the SWIR-driven spectrum extending up to 150 eV in photon energy. It is worth noting that the grating used in the spectrometer suffers a significant drop in diffraction efficiency for energies above 110 eV, as the spectrometer was primarily designed to be used for the XUV light produced by near-infrared pulses. Thus, we expect the photon flux above 110 eV to be higher than indicated by the figure. In order to optimize generation conditions with the SWIR driver, further measurements/calculations on the optimum gas pressure and incoming light intensity as well as a more accurate spectrometer instrumentation are required.

Furthermore, we recorded the harmonic spectra as a function of insertion of glass wedges that we normally use to tune the dispersion and perform d-scan measurements of the infrared pulses. In Figure 5.5(b), we demonstrate an HHG dispersion scan in neon, when driven by a NIR OPCPA, resulting in higher photon energies, when compared to generating in argon with the same source. Here, we also use a zirconium filter to reject low photon energies. We see distinct interference fringes due to variation of the CEP of the driving pulse. Scanning the BK7 wedges changes the CEP and the intensity of the half-cycles leading to the attosecond pulse emission, thus changing the phase difference between consecutive pulses. The change in the phase difference shifts the positions of constructive interference of attosecond pulses, thus resulting in the shift of harmonic structure. Similar behaviour is also seen for the SWIR HHG dispersion scan, realized in argon [Figure 5.5(c)]. Clear interference fringes are observed when the ZnS glass wedges are scanned around the point of optimum compression.

5.2 Photoelectron pump-probe spectroscopy with short trains of attosecond pulses

The ability to produce pulses of attosecond duration paved the way for photoionization studies of atomic and molecular systems on a corresponding timescale [10], with a notable example being the assessment of photoionization time delays [123, 124]. Most measurements rely on methods of pump-probe spectroscopy, and here the two main approaches, emerged in the early 2000's initially as means of attosecond pulse characterization, are highlighted: Reconstruction of Attosecond Beating By Interference of two-photon Transitions (RABBIT) and attosecond streaking [110, 125]. They are based on a two-color photoioniza-

tion process, where an XUV pump ionizes the atom in the presence of an IR probe, with the latter altering the properties of the emitted photoelectrons depending on the delay between the two fields. The RABBIT technique usually works in the domain of long APTs consisting of many pulses combined with many-cycle infrared fields, while attosecond streaking is performed with single attosecond pulses (SAPs) and near-single-to-few-cycle IR waveforms.

In this section, we briefly investigate an intermediate regime, where the atomic system is ionized by a short (2 or 3 pulses) train of attosecond pulses in the presence of a few-cycle infrared field. Depending on the number of pulses in the APT, we observe substantial differences in the photoionization spectra of helium. The details of the experiment are presented in **Paper II**. Here, we only summarize the main results and compare newly obtained experimental data to simulations.

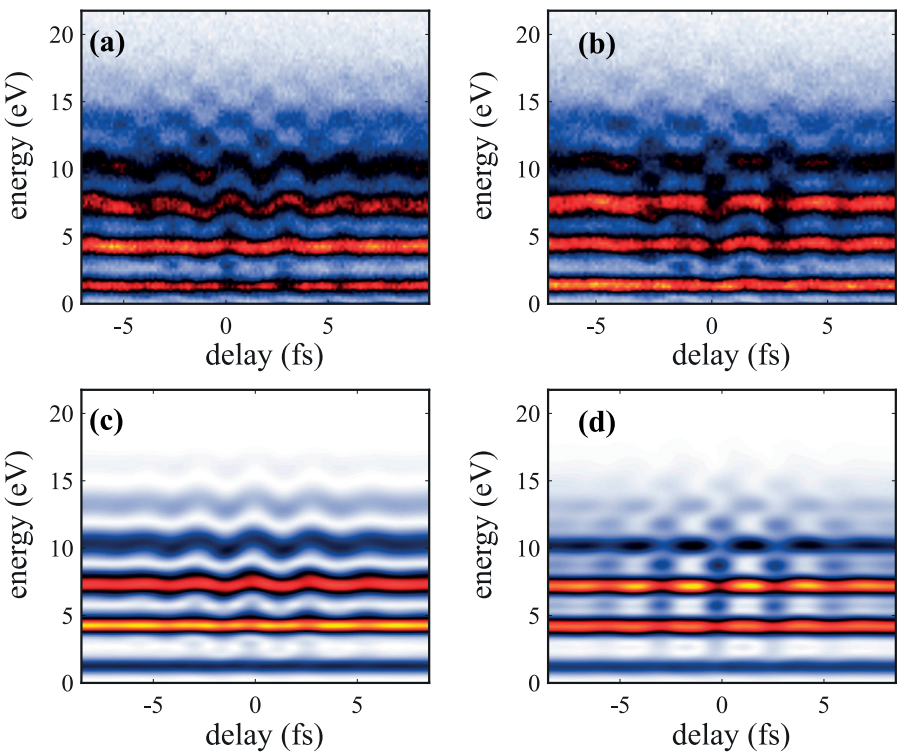

Figure 5.6: Photoelectron spectra in helium as a function of delay, integrated in the down direction. Experimental results for the two-pulse (CEP = $\pi/2$) APT (a) and three-pulse (CEP = 0) APT (b). (c) and (d) - corresponding SFA simulations.

In this experiment, we record cross-correlation traces between short APTs (i.e., the pump) generated with few-cycle pulses from the NIR OPCPA and a time-delayed copy of the

same driving pulse (i.e., the probe) using He as a detection gas. By changing the CEP of the infrared driver with motorized glass wedges, we are able to tune the number of pulses in the APT. The delay between the pump and the probe can be precisely controlled via a piezo-driven delay stage. The detector used in the measurements is a photoelectron/ion 3D momentum imaging spectrometer based on the Coincidences entre ions et electrons localises (CIEL) principle [126–128], which is similar to REaction MIcroscope [129] or Cold Target Recoil Ion Momentum spectroscopy (COLTRIMS) [130] designs. It allows the detection of 3D momentum distributions of photoelectrons and ions over the solid angle of 4π by using a combination of electric and magnetic fields and position sensitive detectors.

The photoelectron spectra as a function of time delay are shown in the top row of Figure 5.6. The bottom row shows the corresponding simulations based on SFA [106, 131, 132], where the IR field intensity was set to $6\times10^{10}\,\mathrm{W/cm^2}$. The spectra are obtained by integrating all the electrons emitted in the "down" direction relative to the laser polarization axis. Similar results are obtained by integrating the electrons emitted in the "up" direction, with a shift in delay by half a period. The reason for the difference between the up and down direction is discussed in detail in ref. [132].

When the APT consists of two attosecond pulses [Figures 5.6(a) and (c)], the photoelectron peaks corresponding to absorption of different harmonic orders are shifted up and down in energy, depending on the delay of the probe field. The energy shifts can be explained as an interference of two electron wave packets (EWPs) ionized by individual attosecond pulses [132]. The presence of the infrared field changes the relative phase of the EWPs, shifting the position of the interference peaks, depending on the value of the IR vector potential. The simulated trace agrees very well with experimental data, with exception of the high energy region (> 12 eV), where a chequered pattern appears in the measured trace, similar to the three-pulse case discussed below.

When photoionization is driven by a three-pulse APT [Figures 5.6(b) and (d)], sidebands appear at positions corresponding to absorption of even harmonics. This is very reminiscent of the spectrograms obtained in the RABBIT measurements. The difference here, however, is that the period of sideband oscillations is equal to a duration of the laser cycle (ω oscillations), while in RABBIT the sidebands oscillate twice as fast (2ω). The existence of photoelectrons at sideband energies arises due to the interference of EWPs ionized by individual pulses in the three-pulse train. The additional phase from the IR influences the positions of constructive and destructive interferences in the sidebands. Due to the HHG femtosecond chirp leading to a variation of the phase difference between two consecutive pulses[4], and to the detection of only "up" or "down" electrons, the interference of EWPs will oscillate only at a frequency of ω.

[4]That is, consecutive pulses in the three-pulse train are not identical to each other. The spectral phase varies in a complex way between attosecond pulses and is not just a constant π shift from one pulse to another.

5.3 Lightwave-driven currents

One of the unique features of carrier-envelope-phase-stable few-cycle pulses is an asymmetric shape of the electric field waveform present at specific values of the CEP. A direct consequence of this property can be observed when such an intense few-cycle pulse is impinging on a dielectric or a semiconductor material. The pulse's electric field will drive a nonlinear current, and the asymmetry in the waveform will lead to a net transfer of charge within the medium, resulting in a residual current signal that can be measured with an external circuit. Since optical fields oscillate at frequencies reaching into the PHz range, the direct generation and control of these currents open up pathways to the development of ultrafast lightwave electronics, potentially boosting signal processing rates by several orders of magnitude.

The first experimental observation of this phenomenon was reported by Schiffrin *et al.* [133] in a sample of fused silica when excited by intense sub-4 fs long pulses (1.4 cycles) at the repetition rate of 1 kHz. Pulses of similar duration were used to investigate the generation of lightwave-driven currents in various semiconductor and dielectric materials [134–136]. However, the generation of near-single-cycle optical pulses is still an experimentally challenging endeavor that sets a constraint on the applicability of this approach. In **Paper VI**, we report on the generation of coherent currents in a high bandgap semiconductor, driven by pulses from the NIR OPCPA at 200 kHz repetition rate. By varying the CEP of the laser pulse, we induce charge oscillations in a gallium nitride (GaN) sample, which are detected via a pair of gold electrodes connected to the sensitive electronic circuit. Our measurement results are in good agreement with a theoretical model based on the interference of multiphoton transitions [137].

The schematic of the device structure used in the experiments is shown in Figure 5.7(a). The sample is based on a GaN film grown on an aluminium oxide (Al_2O_3) substrate. The layer of gold is deposited together with a titanium adhesion layer on GaN with a 5 µm gap in the center of the device. The metal contacts are etched out via UV photolithography, and an additional thin layer of Al_2O_3 is added on top to protect the contacts from environmental and laser-induced damage.

The layout of the experimental setup is illustrated in Figure 5.7(b). The CEP-stable output of the NIR OPCPA passes the BK7 glass wedges and a wire-grid polarizer pair. One of the wedges is mounted on a motorized translation stage, allowing to finely tune the amount of glass insertion in the beam, while the polarizers are used to adjust the incoming laser power. The beam is focused on the sample by a parabolic mirror, and the current is picked up by a pair of aluminium wires connected to an external circuit, consisting of a high-sensitivity pre-amplifier (that amplifies the signal and acts as a current-to-voltage converter) and a lock-in amplifier. We also perform on-target pulse characterization via the second-

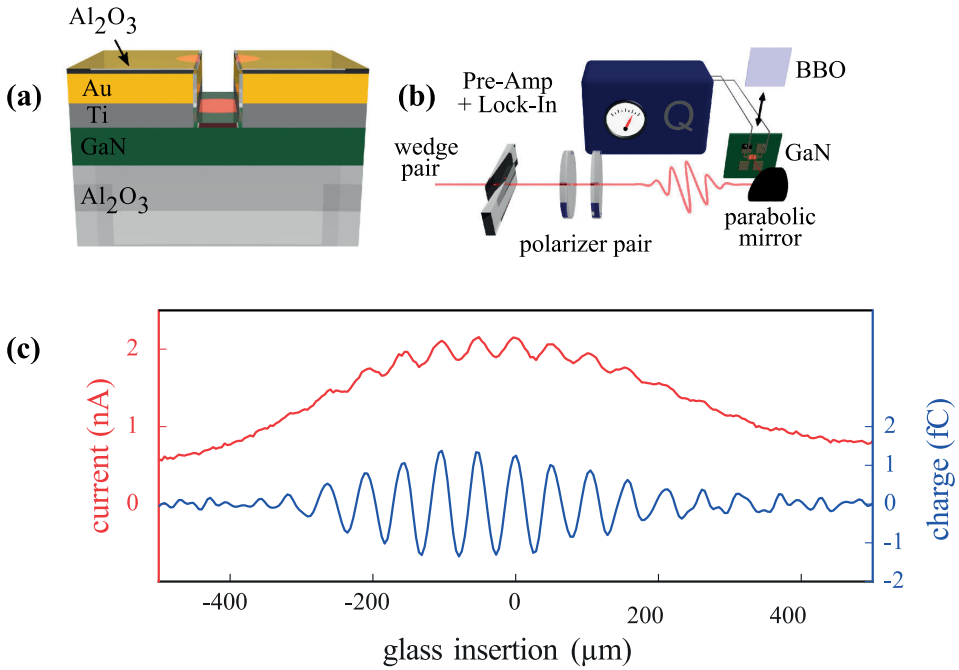

Figure 5.7: Lightwave-driven currents. (a) Sample composition. (b) Experimental setup. (c) Measured current (red) and transferred charge per laser shot (blue), the zero in glass insertion indicates the optimum pulse compression point.

harmonic d-scan, by replacing the GaN sample with a thin BBO crystal and recording the SHG spectrum as a function of the wedge insertion.

The results of the experiment are presented in Figure 5.7(c). As we scan the glass wedges, we observe clear CEP-dependent oscillations in the current signal on top of a large, intensity-dependent offset (red curve). The offset reflects the change in the peak intensity due to stretching/compression of the light pulse. Fourier filtering can be used to remove this offset, and the measured residual charge is plotted in blue in Figure 5.7(c). The charge oscillations grow stronger in amplitude as the pulse approaches the point of optimal compression (i.e. its shortest pulse duration) and vanish for increasing pulse durations. The CEP dependence of the observed signal is clear in the period of oscillations that repeat every $\approx$ 50 µm of inserted BK7 glass, corresponding well to the amount needed to introduce a 2π CEP shift at 850 nm.

To validate the experimental results, we simulate the charge transfer induced by the electric field by employing a model developed by Khurgin [137]. In this model, the photoinduced current is treated as a nonlinear optical effect, originating from the interference of mul-

tiphoton processes that excite virtual charge carriers (electron-hole pairs) in the material. Depending on the CEP, the amount of generated electron-hole pairs will differ slightly for negative or positive values of crystal momentum, leading to a net charge Q remaining after the excitation, which can be calculated in the following way [137]:

$$Q = \epsilon_0 \chi^{(3)} \omega_0^4 \Bigg(\int_{-\infty}^{\infty} d\tau A^3(\tau) + \frac{\chi^{(3)}}{\chi^{(1)}} \omega_0^2 \int_{-\infty}^{\infty} d\tau A^5(\tau) + \left[\frac{\chi^{(3)}}{\chi^{(1)}} \omega_0^2 \right]^2 \int_{-\infty}^{\infty} d\tau A^7(\tau) \Bigg) S_{\text{eff}}, \tag{5.10}$$

where ϵ_0 is the vacuum permittivity, $\chi^{(1)}$ and $\chi^{(3)}$ are the linear and third-order susceptibilities, ω_0 and $A(\tau)$ are the central frequency and the vector potential of the excitation field, and S_{eff} is the effective area of the junction.

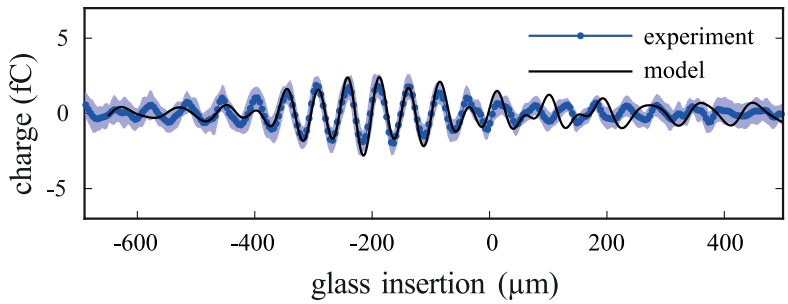

Figure 5.8: Comparison of the experimental data (in blue) to the multiphoton quantum interference model (black curve). The shaded blue area depicts the standard deviation of 20 measurements.

In Figure 5.8, the results of this model are compared to the experimental data. We use the d-scan technique in order to retrieve the electric field of the pulse, which is then integrated to obtain the potential $A(\tau)$ used in Eq. 5.10. The input peak field strength is estimated to be equal to 0.62 V/Å using the retrieved pulse duration and the measured focal spot size and optical power. Employing these parameters, we get an excellent agreement between the simulation and the measurement, indicated by a clear overlap between the curves. Combined with a successful modelling, the experimental observation of lightwave currents generated by longer pulses at increased repetition rates marks an important step towards the development of lightwave-driven electronic devices.

Chapter 6

Summary and outlook

6.1 Summary

The work presented in this thesis is dedicated to the generation, characterization, and application of few-optical-cycle light pulses. These pulses are produced in the infrared region of the electromagnetic spectrum with two distinct technological approaches. Different characterization techniques are used to optimize the output of multiple laser systems and to gain insight into the properties of ultrashort pulses in the time and frequency domains. Finally, several ultrafast optics and strong-field physics applications of these pulses are demonstrated.

The thesis showcases two OPCPA-based light sources that operate in the NIR and SWIR spectral ranges, sharing the same Ti:Sapphire oscillator front-end that seeds an Yb fiber CPA chain. Pumped by the output of two separate Yb rod-type amplifiers, they deliver CEP-stable, sub-2.5-cycle pulses at the repetition rate of 200 kHz. One of these systems, described in detail in **Paper I**, is a SWIR OPCPA emitting 13 µJ 2.3-cycle pulses at a center wavelength of 2 µm. We measure <16 fs pulse duration with a third-harmonic d-scan and demonstrate the potential of the system to drive strong-field experiments by generating high-order harmonics.

The near-infrared OPCPA is a more mature laser source that was commissioned previously to this work. During this thesis, we have performed an upgrade of the system and increased its pulse energy output to 15 µJ. A careful pulse characterization revealed no loss in pulse quality, with 6 fs pulses at 850 nm and a 160 mrad shot-to-shot CEP stability. The energy increase allows us to perform several challenging photoionization studies, shown in **Paper II**.

Nonlinear pulse post-compression using MPCs emerges as an effective way of reducing the pulse duration of high-average-power Yb lasers and is currently an active area of research [17]. During this thesis work, we perform two MPC post-compression experiments. In **Paper III**, we use two cascaded gas-filled MPCs to compress the output of a 2 mJ Yb Innoslab laser amplifier. The first stage brings the pulse duration from 1.2 ps down to 31 fs, with a compression factor of about 40. The second stage, operated at reduced power, yields 13 fs pulses, pushing the system into the few-cycle regime. In **Paper IV**, we show a single-stage bulk MPC for the compression of pulses from one of the Yb rod-type amplifiers. Operating at record-high input and output peak power levels for a bulk MPC, we reach 31 fs duration (from 300 fs) with >88% efficiency. We perform an extensive characterization of the MPC output. No significant loss of beam quality is observed, despite exceeding the critical power of fused silica, the employed nonlinear material, by a factor of 80.

A significant part of the work is focused on obtaining expertise within the field of ultrashort pulse characterization, using several well-known characterization methods. In particular, the d-scan technique is employed to characterize pulses of different durations and central wavelengths, proving this method to be reliable and versatile. We summarize the recent results in the d-scan development in **Paper V**, where we discuss the basics of d-scan measurements, common retrieval algorithms and various approaches to recording second-harmonic d-scans in scanning and single-shot configurations.

Few-cycle pulses from a NIR OPCPA are used as a driving source for several atomic and solid-state physics experiments. In **Paper II**, XUV-IR pump-probe photoionization of helium is studied, where the pump is a short XUV attosecond pulse train, produced via HHG. Depending on the CEP of the infrared driving field, the train consists of two or three attosecond pulses, which has a profound impact on the shape of photoelectron spectra of helium ionized in the presence of the same few-cycle IR pulse. In **Paper VI**, employing the same NIR OPCPA, we demonstrate the generation of coherent currents in the high-bandgap semiconductor GaN. We use almost twice as long pulses to drive the process as reported before, and at a repetition rate two orders of magnitude higher than in previous works. We successfully reproduce our experimental results using a theoretical approach based on the interference of multiphoton transitions, obtaining an excellent agreement with the measured data.

6.2 Outlook

Next generation few-cycle light sources

The development of new systems delivering few-optical-cycle light pulses is a research effort at the frontiers of ultrafast optics, driven by advances in laser materials and post-

compression methods. The OPCPA, while offering considerable advantages discussed before, is a technologically complex approach often requiring powerful pump lasers and various stabilization systems. Currently, it is being challenged by several competing technologies in both the NIR and SWIR spectral ranges, briefly discussed below.

In the near-infrared, a direct competitor to high repetition rate OPCPAs is a multi-stage nonlinear post-compression of Yb CPA lasers. Reducing the pulse duration of high-average-power picosecond Yb laser amplifiers to sub-40 fs is now almost a routine task, owing to the remarkable progress of efficient MPC-based post-compression. Various approaches can perform a leap into the few-cycle regime, e.g., post-compression in multiple thin plates or hollow-core fibers, and several systems based on the combination of post-compression methods have been reported [138, 139]. It is also possible to implement an additional MPC for few-cycle compression, as shown in **Paper III** and [140]; however, it has only been demonstrated with metallic mirrors, which suffer from lower reflectivity and damage thresholds, calling for further research and development efforts for broadband, high-damage-threshold, dispersion controlled coatings.

In the SWIR region, two notable concepts can potentially compete with parametric amplifiers. Direct lasing in bulk crystals can be achieved in the longer part of the SWIR wavelength range (from 2 to 3 μm) with transition-metal-doped-chalcogenides (e.g. Cr:ZnS/ZnSe) as gain media [141]. Recent advances in crystal growth and the emergence of powerful nanosecond pump lasers around 1.6 - 2.1 μm resulted in the successful development of ultrashort-pulsed mJ-level Cr:ZnS/Cr:ZnSe amplifiers at kHz repetition rates, and the first water-window soft X-ray generation was shown in 2020 by Leshchenko *et al.* [142]. However, an HHG-capable operation at high repetition rates (>100 kHz) is yet to be reported[1]. Another approach is based on post-compression of Thulium-doped fiber amplifiers (TDFA). TDFA are capable of delivering enormous (kW-level) average powers [143], and when combined with nonlinear pulse post-compression techniques [144], they are an attractive alternative to OPCPAs. The first soft-X-ray source based on the output of the TDFA was reported recently [145]. In conclusion, we are likely to see an increased variety of SWIR few-cycle light sources driving a multitude of strong-field applications in the future.

Advancing the dispersion scan

As the sources of ultrashort pulses grow in diversity of central wavelengths and pulse durations, so must extend the application ranges of methods of pulse characterization. The d-scan technique is no exception, and further developments are needed to increase its spec-

[1]This laser technology is often referred to as the "Ti:Sapphire of the mid-infrared". As with Ti:Sapphire's advantages (broad absorption and emission bands), Cr:ZnS/ZnSe present its main drawbacks as well: strong thermal lensing and short excited state lifetime [141].

tral coverage and ability to measure pulses of different widths. Several works adapting the d-scan to measure pulses in the mid-infrared have been reported recently [146, 147]. One of the most challenging d-scan development directions is the extension of single-shot variants for the measurement of long, many-cycle pulses emitted from Yb lasers. Without a doubt, we will see more work dedicated to this in the future.

In the domain of pulse retrieval, machine learning algorithms [61, 83] can offer an order of magnitude faster retrieval times than conventional methods. It would be exciting to combine this machine-learning-based retrieval with a single-shot d-scan to perform a "live-view" pulse monitoring of different laser systems at video refresh rates. Furthermore, machine learning can provide the first guess for more standard algorithms, potentially increasing the speed of accurate phase retrieval.

Future applications

Emerging sources of intense few-cycle pulses operating at different central wavelengths and high repetition rates will enable a myriad of exciting applications within attosecond science and ultrafast solid-state physics. The 2.3-cycle SWIR OPCPA system presented in this thesis is already an excellent platform for many experiments, e.g., the optimization of high harmonic flux in heavy gases (argon, krypton), solid-state HHG [148], or for surface science and plasmonics studies with ultrafast photoelectron microscopy[2]. In the following year, the output pulse energy of the SWIR OPCPA will be increased through the upgrade of the pump laser, paving the way for water-window X-ray generation at 200 kHz. This motivates for an extensive investigation of the optimum HHG phase matching conditions [122], which will influence the design of a tailored HHG high-density gas target.

XUV-IR pump-probe spectroscopy using short trains of attosecond pulses allows the study of many exciting features of the APT itself or the ionized atomic system. In the former case, attosecond pulse retrieval algorithms, such as FROG-CRAB (Frequency-Resolved Optical Gating for Complete Reconstruction of Attosecond Bursts) [150] or VTGPA (Volkov Transform Generalized Projection Algorithm) [151], can be used for more accurate reconstruction of these pulse trains (which can potentially help explain puzzling features of the high energy region in the photoelectron spectra shown in Figure 5.6(a)). In the latter case, we aim to demonstrate control of photoionization dynamics by tailoring APTs as well as the driving IR field.

Further advances are being made in the field of lightwave-driven currents. Heide *et al.* [152] showed that employing synchronized two-color fields allows for a current generation two orders of magnitude higher than with single-color schemes due to a larger degree of field

[2]For example, see [149], where a similar light source was used for investigating the properties of electron emission from gold nanoantennas.

asymmetry. However, the cost of this enhancement is an increased complexity of the optical setup, requiring a stabilized two-color interferometer. Recently, Hanus and colleagues [153] observed lightwave currents in various semiconductor and dielectric samples when excited directly by the output of a few-cycle Ti:Sapphire oscillator, operating at 80 MHz. Achieving an operation at a much higher repetition rate than previously and with a simple experimental setup, this result brings the emerging field of petahertz optoelectronics forward.

Author Contributions

Paper I: Few-cycle short-wave-infrared light source for strong-field experiments at 200 kHz repetition rate

This paper summarizes the development and characterization of the short-wave infrared few-cycle light source. It includes a description of the stages of the experimental setup based on different nonlinear optical processes as well as a detailed characterization of the SWIR pulse with regard to output spectrum, pulse duration, and CEP stability. It demonstrates a simple and efficient scheme to measure the CEP of the SWIR few-cycle pulses and presents first HHG experiments performed with this system.

I took a leading role in the development of the experimental setup throughout my doctoral studies. I performed the SWIR pulse characterization and with the help of colleagues performed a high-order harmonic generation experiment. Finally, I wrote the manuscript.

Paper II: A high-repetition rate attosecond light source for time-resolved coincidence spectroscopy

This paper presents a high repetition rate near-infrared OPCPA-based attosecond beamline at the Lund Laser Centre. The characteristics of the laser source as well as the design of the XUV-IR pump-probe interferometer are presented. This beamline was used to perform advanced 3-D momentum spectroscopy experiments using time-resolved and coincidence techniques.

I took part in the maintenance and optimization of the OPCPA light source. I performed the dispersion scan measurements presented in this work. I provided feedback and comments during the preparation of the manuscript.

Paper III: Postcompression of picosecond pulses into the few-cycle regime

This paper demonstrated the efficient nonlinear compression of picosecond pulses down to 13 fs duration using gas-phase spectral broadening in two consecutive multipass cells. A description of the experimental setup along with pulse duration measurements using the FROG and d-scan techniques are presented.

I took part in the experimental campaign and performed the FROG and the d-scan measurements. I analyzed the FROG data and provided feedback and comments for the manuscript.

Paper IV: Multi-gigawatt peak power post-compression in a bulk multi-pass cell at high repetition rate

In this paper, a compact pulse post-compression setup based on bulk multipass cell is demonstrated. The nonlinear broadening in thin fused silica plates and subsequent chirped-mirror compressor leads to reduction of the pulse width by an order of magnitude. An extensive pulse characterization is performed: pulse duration, power, spectral and CEP stability. The effect of spatio-temporal couplings is measured.

I took part in the building and alignment of the laser amplifier together with the grating compressor that were used in this work and built an interferometer for the FROG measurements. I provided feedback for the manuscript.

Paper V: Characterizing ultrashort laser pulses with second harmonic dispersion scans

This paper provides a review of different dispersion scan measurements, mostly performed at the Lund Laser Centre. Focusing on the second harmonic version of the d-scan, various aspects of this technique are presented in a tutorial manner. Measurements on various laser systems in different pulse duration regimes are presented for both conventional and single-shot versions of the d-scan, demonstrating the versatility and robustness of this method.

I have performed the majority of the measurements presented in this paper and analyzed the data. I wrote the manuscript with the help and feedback from colleagues.

Paper VI: Few-cycle lightwave-driven currents in a semiconductor at high repetition rate

This paper presents results on the generation of light-wave driven currents in semiconductors using a 200 kHz near-infrared OPCPA light source. Charge oscillations were measured using longer pulses than previously reported at high repetition rate. The experimental results are supported by a theoretical model based on the interference of multi-photon processes.

I contributed to the maintenance and optimization of the OPCPA source during the experiments. I provided comments and feedback for the manuscript.

Acknowledgments

In the year 2022, on the sunny and rather hot day of the third of August, I started to write a special section of the doctoral thesis. The writing of this section brought me happiness for several reasons. First, it meant that all the other important sections were written and I could relax a little bit. Second, I no longer worried that the word "to write" (and its derivatives) would appear too often in this paragraph. But most importantly, now I could finally express my gratitude to all the people who have helped me to get to this point, *in the writing*.

To begin, I would like to thank my supervisors. I could always show up with questions or discussions, and you would always be happy to talk to me. I believe this is one of the reasons that we have such a great atmosphere and environment within the group. Cord, thank you for sharing all the knowledge and experience and helping me navigate different sides of the PhD journey, whether it was problems in the lab or difficulties during the writing. Thank you, Anne, for accepting me as a student and showing me how exciting physics can be. I enjoyed our discussions about high harmonics a lot towards the end of my PhD and I learned so much. Fabian, I could not wish for a better SWIR teammate, and I can say for sure that our SWIR laser would not have got as far as it did without you. I am grateful for the time we shared at the workplace and outside of it.

A special thank you goes to the present and past members of the 0.2 MHz team with whom I worked in the lab during those four years. Thank you, Chen, for answering all my 31415926 questions and the endless optics discussions we had. Thank you, Sara, for showing me how the OPCPA worked at the beginning of my PhD and for all your excellent explanations on the complex COLTRIMS (CIEL?) stuff. Jan (Vogelsang), thank you for all the knowledge that you shared with me about MATLAB programming and vacuum things. Anne-Lise, thank you for joining the SWIR development (and many other projects). Your help and support were invaluable and always came when I needed it. Anka, thanks for your cheerful attitude and all the joyful conversations we had. Thank you, Dominik, for sharing my passion for stable lasers and showing the importance of chillers. Yu-Chen, thank you for being a great office mate and for the friendly atmosphere around you. Praveen, thank you

for joining our team and already contributing to the friendly spirit within our lab.

There are many amazing people in the big atto group who made my PhD so interesting and fun. Thank you: Neven, for inventing the legendary lunch game (Figure 6.1) and for the classic Neven conversations. Robin, for the Neven conversations 2.0. Hugo, for your mushroom ratings and being Hugo. Mattias, for being a non-Swedish Swede. Lana, for your passion for vocative commas, "Let's eat, Ivan" and "Let's eat Ivan" are indeed two very different sentences. Emma, for all the funny businesses and excellent stuffs. Samuel, for your great company and for our laser chess battles a long time ago. Marius, for accepting me as your flatmate and great late-night-after-party conversations. Jasper, for your appreciation of the *Blin* Boys and all the Formula 1 chats. Jan (Lahl), for all your amazing puns.

There are many people who are (were) part of the atto group who play (played) a great role in making this group so nice to work in. Thank you Per, Johan, Mathieu, Hampus, Sylvain, Elisa, Lisa, Marius (Petersen), Sizuo, Daniel, Saga, Serhii, Venus, and the people I might have forgotten to add to this list.

My gratitude also goes to all the people working in different groups in Atomic Physics who contributed to great atmosphere in the division. Thank you for Monday Fika, Christmas Dinners, Friday meetings and so many other things. I am grateful to the administrative and technical staff of the division (Anne Petersson Jungbeck, Jakob Testad, Maria Algotsson, Åke Johansson, and Jane Nilsson) for providing the great support for our research work.

Special spasibo goes to Sasha Permogorov and señor David Busto, the honorary slav. You guys are a huge part why I felt so at peace and happy when I came back from Belgium. I am grateful to have you as my friends, thanks for all the trips, adventures and experiences that we shared during all these years.

I would like to mention my friends Temur, Gosha, Dima (Zenkovich) and Dima (Mosin), Anna, Reeta, Anton (Skripilov), and Anton (Kozubov), and thank them for all the great moments and memories.

Мама, папа. Эта работа - конец одного большого путешествия, которое никогда бы не случилось, если бы не вы. Я вас очень люблю.

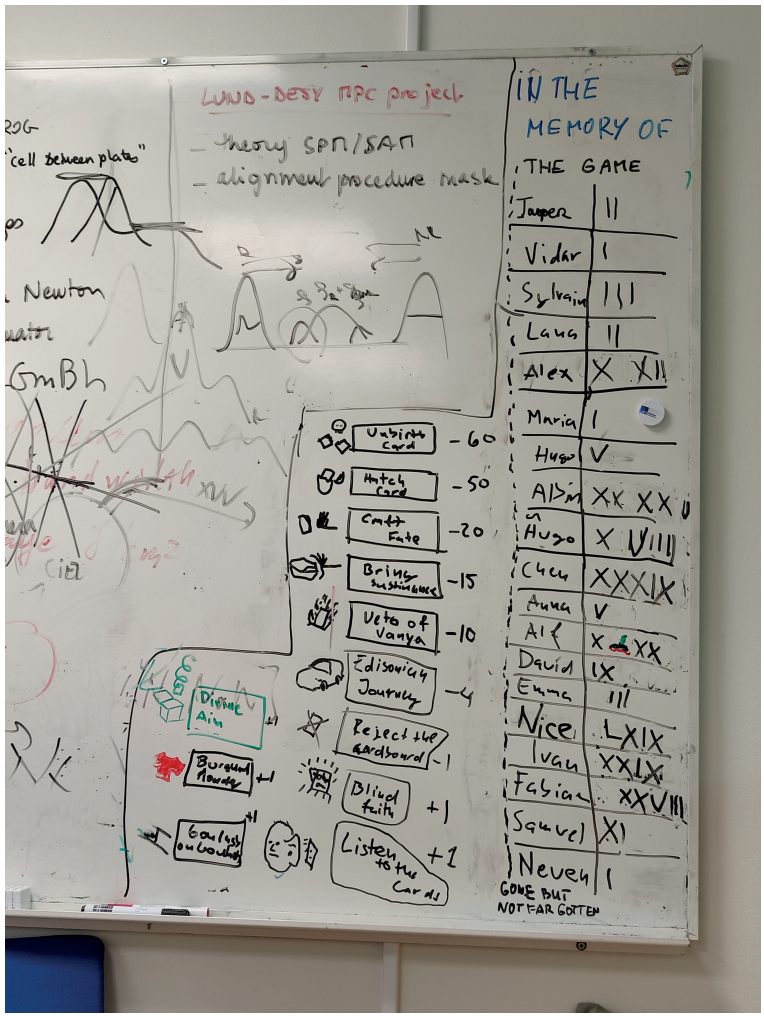

Figure 6.1: The infamous attogroup lunch game. I would like to veto the BMC.

References

[1] T. H. Maiman. Stimulated optical radiation in Ruby. *Nature*, **187**:493, 1960.

[2] L. E. Hargrove, R. L. Fork, and M. A. Pollack. Locking of HeNe laser modes induced by synchronous intracavity modulation. *Applied Physics Letters*, 5(1):4–5, 1964.

[3] M. DiDomenico, J. E. Geusic, H. M. Marcos, and R. G. Smith. Generation of ultrashort optical pulses by mode locking the YAIG:Nd laser. *Appl. Phys. Lett.*, 8(7):180–183, 1966.

[4] P. F. Moulton. Spectroscopic and laser characteristics of Ti:Al_2O_3. *J. Opt. Soc. Am. B*, 3(1):125–133, 1986.

[5] U. Morgner, F. X. Kärtner, S. H. Cho, Y. Chen, H. A. Haus, J. G. Fujimoto, E. P. Ippen, V. Scheuer, G. Angelow, and T. Tschudi. Sub-two-cycle pulses from a Kerr-lens mode-locked Ti:sapphire laser. *Opt. Lett.*, **24**:411, 1999.

[6] P. A. Franken, A. E. Hill, C. W. Peters, and G. Weinreich. Generation of optical harmonics. *Phys. Rev. Lett.*, **7**:118, 1961.

[7] A. McPherson, G. Gibson, H. Jara, U. Johann, T. S. Luk, I. A. McIntyre, K. Boyer, and C. K. Rhodes. Studies of multiphoton production of vacuum-ultraviolet radiation in the rare gases. *Journal of the Optical Society of America B*, **4**:595, 1987.

[8] M. Ferray, A. L'Huillier, X. Li, L. Lompre, G. Mainfray, and C. Manus. Multiple-harmonic conversion of 1064 nm radiation in rare gases. *J. Phys. B*, **21**:L31, 1988.

[9] P. Antoine, A. L'Huillier, and M. Lewenstein. Attosecond Pulse Trains Using High-Order Harmonics. *Phys. Rev. Lett.*, **77**:1234, 1996.

[10] F. Krausz and M. Ivanov. Attosecond physics. *Rev. Mod. Phys.*, 81(1):163–234, 2009.

[11] D. Strickland and G. Mourou. Compression of amplified chirped optical pulses. *Opt. Commun.*, **56**:219, 1985.

[12] M. Müller, A. Klenke, A. Steinkopff, H. Stark, A. Tünnermann, and J. Limpert. 3.5 kW coherently combined ultrafast fiber laser. *Opt. Lett.*, 43(24):6037–6040, 2018.

[13] P. Russbueldt, D. Hoffmann, M. Höfer, J. Löhring, J. Luttmann, A. Meissner, J. Weitenberg, M. Traub, T. Sartorius, D. Esser, R. Wester, P. Loosen, and R. Poprawe. Innoslab amplifiers. *IEEE Journal of Selected Topics in Quantum Electronics*, 21(1):447–463, Jan.-Feb. 2015.

[14] J.-P. Negel, A. Loescher, A. Voss, D. Bauer, D. Sutter, A. Killi, M. A. Ahmed, and T. Graf. Ultrafast thin-disk multipass laser amplifier delivering 1.4 kW (4.7 mJ, 1030 nm) average power converted to 820 W at 515 nm and 234 W at 343 nm. *Opt. Express*, 23(16):21064–21077, 2015.

[15] H. Fattahi, H. G. Barros, M. Gorjan, T. Nubbemeyer, B. Alsaif, C. Y. Teisset, M. Schultze, S. Prinz, M. Haefner, M. Ueffing, A. Alismail, L. Vamos, A. Schwarz, O. Pronin, J. Brons, X. T. Geng, G. Arisholm, M. Ciappina, V. S. Yakovlev, D.-E. Kim, A. M. Azzeer, N. Karpowicz, D. Sutter, Z. Major, T. Metzger, and F. Krausz. Third-generation femtosecond technology. *Optica*, 1(1):45–63, 2014.

[16] A. Dubietis, G. JonuÅ¡auskas, and A. Piskarskas. Powerful femtosecond pulse generation by chirped and stretched pulse parametric amplification in bbo crystal. *Optics Communications*, 88(4â€“6):437 – 440, 1992.

[17] A.-L. Viotti, M. Seidel, E. Escoto, S. Rajhans, W. P. Leemans, I. Hartl, and C. M. Heyl. Multi-pass cells for post-compression of ultrashort laser pulses. *Optica*, 9(2):197–216, 2022.

[18] P. Corkum. Plasma perspective on strong-field multiphoton ionization. *Phys. Rev. Lett.*, **71**:1994, 1993.

[19] J. Tate, T. Auguste, H. G. Muller, P. Salieres, P. Agostini, and L. F. DiMauro. Scaling of wave-packet dynamics in an intense mid-infrared field. *Phys. Rev. Lett.*, 98:013901, 2007.

[20] A. D. Shiner, C. Trallero-Herrero, N. Kajumba, H.-C. Bandulet, D. Comtois, F. Légaré, M. Giguère, J.-C. Kieffer, P. B. Corkum, and D. M. Villeneuve. Wavelength scaling of high harmonic generation efficiency. *Phys. Rev. Lett.*, 103:073902, 2009.

[21] J. Pupeikis, P.-A. Chevreuil, N. Bigler, L. Gallmann, C. R. Phillips, and U. Keller. Water window soft x-ray source enabled by a 25 W few-cycle 2.2 µm OPCPA at 100 kHz. *Optica*, 7(2):168–171, 2020.

[22] M. Neuhaus, H. Fuest, M. Seeger, J. Schötz, M. Trubetskov, P. Russbueldt, H. Hoffmann, E. Riedle, Z. Major, V. Pervak, M. F. Kling, and P. Wnuk. 10 W CEP-stable

few-cycle source at 2 µm with 100 kHz repetition rate. *Optics Express*, 26(13):16074–16085, 2018.

[23] Y. Deng, A. Schwarz, H. Fattahi, M. Ueffing, X. Gu, M. Ossiander, T. Metzger, V. Pervak, H. Ishizuki, T. Taira, T. Kobayashi, G. Marcus, F. Krausz, R. Kienberger, and N. Karpowicz. Carrier-envelope-phase-stable, 1.2 mJ, 1.5 cycle laser pulses at 2.1 µm. *Opt. Lett.*, 37(23):4973–4975, 2012.

[24] Y. Shamir, J. Rothhardt, S. Hädrich, S. Demmler, M. Tschernajew, J. Limpert, and A. Tünnermann. High-average-power 2 µm few-cycle optical parametric chirped pulse amplifier at 100 kHz repetition rate. *Opt. Lett.*, 40(23):5546–5549, 2015.

[25] T. Feng, A. Heilmann, M. Bock, L. Ehrentraut, T. Witting, H. Yu, H. Stiel, S. Eisebitt, and M. Schnüer. 27 W 2.1 µm OPCPA system for coherent soft X-ray generation operating at 10 kHz. *Opt. Express*, 28(6):8724–8733, 2020.

[26] X. Gu, G. Marcus, Y. Deng, T. Metzger, C. Teisset, N. Ishii, T. Fuji, A. Baltuska, R. Butkus, V. Pervak, H. Ishizuki, T. Taira, T. Kobayashi, R. Kienberger, and F. Krausz. Generation of carrier-envelope-phase-stable 2-cycle 740-µJ pulses at 2.1-µm carrier wavelength. *Opt. Express*, 17(1):62–69, 2009.

[27] Y. Yin, J. Li, X. Ren, K. Zhao, Y. Wu, E. Cunningham, and Z. Chang. High-efficiency optical parametric chirped-pulse amplifier in BiB_3O_6 for generation of 3 mJ, two-cycle, carrier-envelope-phase-stable pulses at 1.7 µm. *Opt. Lett.*, 41(6):1142–1145, 2016.

[28] F. Silva, P. K. Bates, A. Esteban-Martin, M. Ebrahim-Zadeh, and J. Biegert. High-average-power, carrier-envelope phase-stable, few-cycle pulses at 2.1 µm from a collinear BiB_3O_6 optical parametric amplifier. *Opt. Lett.*, 37(5):933–935, 2012.

[29] T. Fuji, N. Ishii, C. Y. Teisset, X. Gu, T. Metzger, A. Baltuska, N. Forget, D. Kaplan, A. Galvanauskas, and F. Krausz. Parametric amplification of few-cycle carrier-envelope phase-stable pulses at 2.1 µm. *Opt. Lett.*, 31(8):1103–1105, 2006.

[30] T. Gaumnitz, A. Jain, Y. Pertot, M. Huppert, I. Jordan, F. Ardana-Lamas, and H. J. Wörner. Streaking of 43-attosecond soft-X-ray pulses generated by a passively CEP-stable mid-infrared driver. *Optics Express*, 25(22):27506, 2017.

[31] M. Miranda, T. Fordell, C. Arnold, A. L'Huillier, and H. Crespo. Simultaneous compression and characterization of ultrashort laser pulses using chirped mirrors and glass wedges. *Opt. Express*, 20(1):688–697, 2012.

[32] J. D. Jackson. *Classical electrodynamics.* New York : Wiley, cop. 1999, 1999.

[33] https://refractiveindex.info/.

[34] A. E. Siegman. *Lasers*. University Science Books, Sausalito, 1986.

[35] E. Treacy. Optical pulse compression with diffraction gratings. *Quantum Electronics, IEEE Journal of*, 5(9):454 – 458, 1969.

[36] R. L. Fork, O. E. Martinez, and J. P. Gordon. Negative dispersion using pairs of prisms. *Opt. Lett.*, 9:150, 1984.

[37] R. L. Fork, C. H. B. Cruz, P. C. Becker, and C. V. Shank. Compression of optical pulses to six femtoseconds by using cubic phase compensation. *Opt. Lett.*, **12**:483, 1987.

[38] S. Backus, C. G. Durfee, M. M. Murnane, and H. C. Kapteyn. High power ultrafast lasers. *Review of Scientific Instruments*, 69(3):1207–1223, 1998.

[39] R. W. Boyd. *Nonlinear Optics*. Academic Press, 2003.

[40] R. A. Lewis. A review of terahertz sources. *Journal of Physics D: Applied Physics*, 47(37):374001–, 2014.

[41] G. Cerullo and S. De Silvestri. Ultrafast optical parametric amplifiers. *Review of Scientific Instruments*, 74(1):1–18, 2003.

[42] B. E. A. Saleh and M. C. Teich. *Fundamentals of Photonics*. John Wiley and Sons, 2007.

[43] J. Q. Yao and T. S. Fahlen. Calculations of optimum phase match parameters for the biaxial crystal ktiopo4. *Journal of Applied Physics*, 55(1):65–68, 1984.

[44] A. Baltuška, T. Fuji, and T. Kobayashi. Controlling the carrier-envelope phase of ultrashort light pulses with optical parametric amplifiers. *Phys. Rev. Lett.*, 88:133901, 2002.

[45] G. Cerullo, A. Baltuška, O. Mücke, and C. Vozzi. Few-optical-cycle light pulses with passive carrier-envelope phase stabilization. *Laser & Photon. Rev.*, 5(3):323–351, 2011.

[46] C. Manzoni and G. Cerullo. Design criteria for ultrafast optical parametric amplifiers. *Journal of Optics*, 18(10):103501–, 2016.

[47] W. J. Tomlinson, R. H. Stolen, and C. V. Shank. Compression of optical pulses chirped by self-phase modulation in fibers. *J. Opt. Soc. Am. B*, **1**:139, 1984.

[48] M. Nisoli, S. D. Silvestri, and O. Svelto. Generation of high energy 10 fs pulses by a new pulse compression technique. *Appl. Phys. Lett.*, 68:2793, 1996.

[49] E. P. Ippen and C. V. Shank. *Ultrashort Light Pulses: Picosecond Techniques and Applications*, chapter Techniques for Measurement, pages 83–122. Springer Berlin Heidelberg, 1977.

[50] J.-C. Diels and W. Rudolph. *Ultrashort laser pulse phenomena*. Academic Press, 1996.

[51] K. Naganuma, K. Mogi, and H. Yamada. General method for ultrashort light pulse chirp measurement. *Quantum Electronics, IEEE Journal of*, 25(6):1225 –1233, 1989.

[52] W. Yang, M. Springer, J. Strohaber, A. Kolomenski, H. Schuessler, G. Kattawar, and A. Sokolov. Spectral phase retrieval from interferometric autocorrelation by a combination of graduated optimization and genetic algorithms. *Opt. Express*, 18(14):15028–15038, 2010.

[53] J.-H. Chung and A. M. Weiner. Ambiguity of ultrashort pulse shapes retrieved from the intensity autocorrelation and the power spectrum. *IEEE Journal of selected topics in quantum electronics*, 7(4):656–666, 2001.

[54] D. J. Kane and R. Trebino. Characterization of Arbitrary Femtosecond Pulses Using Frequency-Resolved Optical Gating. *IEEE J. Quantum Electron.*, **29**:571, 1993.

[55] R. Trebino and D. J. Kane. Using phase retrieval to measure the intensity and phase of ultrashort pulses: frequency-resolved optical gating. *J. Opt. Soc. Am. A*, 10:1101, 1993.

[56] R. W. Gerchberg and W. O. Saxton. A practical algorithm for the determination of phase from image and diffraction plane pictures. *Optik*, 35(2):237–246, 1972.

[57] D. Kane. Principal components generalized projections: a review. *J. Opt. Soc. Am. B*, 25:A120–A132, 2008.

[58] D. J. Kane and R. Trebino. Single-shot measurement of the intensity and phase of an arbitrary ultrashort pulse by using frequency-resolved optical gating. *Opt. Lett.*, **18**:823, 1993.

[59] P. O'Shea, M. Kimmel, X. Gu, and R. Trebino. Highly simplified device for ultrashort-pulse measurement. *Opt. Lett.*, 26(12):932–934, 2001.

[60] G. Stibenz and G. Steinmeyer. Interferometric frequency-resolved optical gating. *Opt. Express*, 13(7):2617–2626, 2005.

[61] P. Sidorenko, O. Lahav, Z. Avnat, and O. Cohen. Ptychographic reconstruction algorithm for frequency-resolved optical gating: super-resolution and supreme robustness. *Optica*, 3(12):1320–1330, 2016.

[62] T. Zahavy, A. Dikopoltsev, D. Moss, G. I. Haham, O. Cohen, S. Mannor, and M. Segev. Deep learning reconstruction of ultrashort pulses. *Optica*, 5:666–673, 2018.

[63] C. Iaconis and I. A. Walmsley. Spectral phase interferometry for direct electric field reconstruction of ultrashort optical pulses. *Opt. Lett.*, 23:792, 1998.

[64] M. Anderson, A. Monmayrant, S.-P. Gorza, P. Wasylczyk, and I. Walmsley. Spider: A decade of measuring ultrashort pulses. *Laser Phys. Lett.*, 5(4):259–266, 2008.

[65] I. A. Walmsley and C. Dorrer. Characterization of ultrashort electromagnetic pulses. *Adv. Opt. Photon.*, 1(2):308–437, 2009.

[66] A. S. Wyatt, I. A. Walmsley, G. Stibenz, and G. Steinmeyer. Sub-10 fs pulse characterization using spatially encoded arrangement for spectral phase interferometry for direct electric field reconstruction. *Opt. Lett.*, 31(12):1914–1916, 2006.

[67] J. R. Birge, R. Ell, and F. X. Kärtner. Two-dimensional spectral shearing interferometry for few-cycle pulse characterization. *Opt. Lett.*, 31(13):2063–2065, 2006.

[68] D. R. Austin, T. Witting, and I. A. Walmsley. Resolution of the relative phase ambiguity in spectral shearing interferometry of ultrashort pulses. *Opt. Lett.*, 35(12):1971–1973, 2010.

[69] A. S. Wyatt, A. Grün, P. K. Bates, O. Chalus, J. Biegert, and I. A. Walmsley. Accuracy measurements and improvement for complete characterization of optical pulses from nonlinear processes via multiple spectral-shearing interferometry. *Opt. Express*, 19(25):25355–25366, 2011.

[70] V. V. Lozovoy, I. Pastirk, and M. Dantus. Multiphoton intrapulse interference. IV. Ultrashort laserpulse spectral phase characterization and compensation. *Opt. Lett.*, 29(7):775–777, 2004.

[71] Y. Coello, V. V. Lozovoy, T. C. Gunaratne, B. Xu, I. Borukhovich, C. hung Tseng, T. Weinacht, and M. Dantus. Interference without an interferometer: a different approach to measuring, compressing, and shaping ultrashort laser pulses. *J. Opt. Soc. Am. B*, 25(6):A140–A150, 2008.

[72] V. V. Lozovoy, B. Xu, Y. Coello, and M. Dantus. Direct measurement of spectral phase for ultrashort laser pulses. *Opt. Express*, 16(2):592–597, 2008.

[73] B. Xu, J. M. Gunn, J. M. D. Cruz, V. V. Lozovoy, and M. Dantus. Quantitative investigation of the multiphoton intrapulse interference phase scan method for simultaneous phase measurement and compensation of femtosecond laser pulses. *J. Opt. Soc. Am. B*, 23(4):750–759, 2006.

[74] M. Miranda, C. L. Arnold, T. Fordell, F. Silva, B. Alonso, R. Weigand, A. L'Huillier, and H. Crespo. Characterization of broadband few-cycle laser pulses with the d-scan technique. *Opt. Express*, 20(17):18732–18743, 2012.

[75] A. Tajalli, B. Chanteau, M. Kretschmar, H. Kurz, D. Zuber, M. Kovačev, U. Morgner, and T. Nagy. Few-cycle optical pulse characterization via cross-polarized wave generation dispersion scan technique. *Opt. Lett.*, 41(22):5246–5249, 2016.

[76] A. Tajalli, T. K. Kalousdian, M. Kretschmar, S. Kleinert, U. Morgner, and T. Nagy. Full characterization of 8 fs deep uv pulses via a dispersion scan. *Opt.Lett*, 44:2498–2501, 2019.

[77] J. A. Nelder and R. Mead. A Simplex Method for Function Minimization. *The Computer Journal*, 7(4):308–313, 1965.

[78] A. Baltuska, A. Pugzlys, M. Pshenichnikov, and D. Wiersma. Rapid amplitude-phase reconstruction of femtosecond pulses from intensity autocorrelation and spectrum. In *Technical Digest. Summaries of papers presented at the Conference on Lasers and Electro-Optics. Postconference Edition. CLEO '99. Conference on Lasers and Electro-Optics (IEEE Cat. No.99CH37013)*, pages 264 –265, 1999.

[79] B. Alonso, I. Sola, and H. Crespo. Self-calibrating d-scan: measuring ultrashort laser pulses on-target using an arbitrary pulse compressor. *Scientific Reports*, 8(1):3264–, 2018.

[80] E. Escoto, A. Tajalli, T. Nagy, and G. Steinmeyer. Advanced phase retrieval for dispersion scan: a comparative study. *J. Opt. Soc. Am. B*, 35:8–19, 2018.

[81] M. Miranda, J. Penedones, C. Guo, A. Harth, M. Louisy, L. Neoričić, A. L'Huillier, and C. L. Arnold. Fast iterative retrieval algorithm for ultrashort pulse characterization using dispersion scans. *J. Opt. Soc. Am. B*, 34(1):190–197, 2017.

[82] N. C. Geib, M. Zilk, T. Pertsch, and F. Eilenberger. Common pulse retrieval algorithm: a fast and universal method to retrieve ultrashort pulses. *Optica*, 6(4):495–505, 2019.

[83] S. Kleinert, A. Tajalli, T. Nagy, and U. Morgner. Rapid phase retrieval of ultrashort pulses from dispersion scan traces using deep neural networks. *Opt. Lett.*, 44(4):979–982, 2019.

[84] D. Fabris, W. Holgado, F. Silva, T. Witting, J. W. G. Tisch, and H. Crespo. Single-shot implementation of dispersion-scan for the characterization of ultrashort laser pulses. *Opt. Express*, 23(25):32803–32808, 2015.

[85] M. Louisy, C. Guo, L. Neoričić, S. Zhong, A. L'Huillier, C. L. Arnold, and M. Miranda. Compact single-shot d-scan setup for the characterization of few-cycle laser pulses. *Appl. Opt.*, 56(32):9084–9089, 2017.

[86] F. J. Salgado-Remacha, B. Alonso, H. Crespo, C. Cojocaru, J. Trull, R. Romero, M. López-Ripa, P. T. Guerreiro, F. Silva, M. Miranda, A. L'Huillier, C. L. Arnold, and I. J. Sola. Single-shot d-scan technique for ultrashort laser pulse characterization using transverse second-harmonic generation in random nonlinear crystals. *Opt. Lett.*, 45(14):3925–3928, 2020.

[87] M. Czerny and A. F. Turner. Über den astigmatismus bei spiegelspektrometern. *Zeitschrift für Physik*, 61:792–797, 1930.

[88] G. G. Paulus, F. Grasbon, H. Walther, P. Villoresi, M. Nisoli, S. Stagira, E. Priori, and S. De Silvestri. Absolute-phase phenomena in photoionization with few-cycle laser pulses. *Nature*, 414:182, 2001.

[89] M. Schätzel, F. Lindner, G. G. P. H. Walther, E. Goulielmakis, A. baltuska, M. Lezius, and F. Krausz. Long-term stabilization of the carrier-envelope phase of few-cycle laser pulses. *Appl. Phys. B*, 79:1021, 2004.

[90] T. Wittmann, B. Horvath, W. Helml, M. G. Schätzel, X. Gu, A. L. Cavalieri, G. G. Paulus, and R. Kienberger. Single-shot carrier-envelope phase measurement of few-cycle laser pulses. *Nat. Phys.*, 5:357, 2009.

[91] E. Goulielmakis, M. Uiberacker, R. Kienberger, A. Baltuska, V. Yakovlev, A. Scrinzi, T. Westerwalbesloh, U. Kleineberg, U. Heinzmann, M. Drescher, and F. Krausz. Direct measurement of light waves. *Science*, 305(5688):1267–1269, 2004.

[92] S. Keiber, S. Sederberg, A. Schwarz, M. Trubetskov, V. Pervak, F. Krausz, and N. Karpowicz. Electro-optic sampling of near-infrared waveforms. *Nat. Photon.*, 10(3):159–162, 2016.

[93] S. B. Park, K. Kim, W. Cho, S. I. Hwang, I. Ivanov, C. H. Nam, and K. T. Kim. Direct sampling of a light wave in air. *Optica*, 5(4):402–408, 2018.

[94] H. R. Telle, G. Steinmeyer, A. E. Dunlop, J. Stenger, D. H. Sutter, and U. Keller. Carrier-envelope offset phase control: A novel concept for absolute optical frequency measurement and ultrashort pulse generation. *Appl. Phys. B*, 69:327, 1999.

[95] D. J. Jones, S. A. Diddams, J. K. Ranka, A. Stentz, R. S. Windeler, J. L. Hall, and S. T. Cundiff. Carrier-envelope phase control of femtosecond mode-locked lasers and direct optical frequency synthesis. *Science*, 288:635, 2000.

[96] A. Apolonski, A. Poppe, G. Tempea, C. Spielmann, T. Udem, R. Holzwarth, T. W. Hänsch, and F. Krausz. Controlling the phase evolution of few-cycle light pulses. *Phys. Rev. Lett.*, 85:740, 2000.

[97] T. Fuji, J. Rauschenberger, A. Apolonski, V. S. Yakovlev, G. Tempea, T. Udem, C. Gohle, T. W. Hänsch, W. Lehnert, M. Scherer, and F. Krausz. Monolithic carrier-envelope phase-stabilization scheme. *Opt. Lett.*, 30(3):332–334, 2005.

[98] A. Harth, C. Guo, Y.-C. Cheng, A. Losquin, M. Miranda, S. Mikaelsson, C. M. Heyl, O. Prochnow, J. Ahrens, U. Morgner, A. L'Huillier, and C. L. Arnold. Compact 200 kHz HHG source driven by a few-cycle OPCPA. *J. Opt.*, 20(1):014007, 2017.

[99] J. Matyschok, T. Lang, T. Binhammer, O. Prochnow, S. Rausch, M. Schultze, A. Harth, P. Rudawski, C. L. Arnold, A. L'Huillier, et al. Temporal and spatial effects inside a compact and cep stabilized, few-cycle opcpa system at high repetition rates. *Optics Express*, 21(24):29656–29665, 2013.

[100] C.-H. Lu, Y.-J. Tsou, H.-Y. Chen, B.-H. Chen, Y.-C. Cheng, S.-D. Yang, M.-C. Chen, C.-C. Hsu, and A. H. Kung. Generation of intense supercontinuum in condensed media. *Optica*, 1(6):400–406, 2014.

[101] Y.-C. Cheng, C.-H. Lu, Y.-Y. Lin, and A. H. Kung. Supercontinuum generation in a multi-plate medium. *Opt. Express*, 24(7):7224–7231, 2016.

[102] M. Seidel, P. Balla, C. Li, G. Arisholm, L. Winkelmann, I. Hartl, and C. M. Heyl. Factor 30 Pulse Compression by Hybrid Multipass Multiplate Spectral Broadening. *Ultrafast Science*, 2022:9754919–, 2022.

[103] M. Miranda, M. Kotur, P. Rudawski, C. Guo, A. Harth, A. L'Huillier, and C. L. Arnold. Spatiotemporal characterization of ultrashort laser pulses using spatially resolved Fourier transform spectrometry. *Opt. Lett.*, 39(17):5142–5145, 2014.

[104] J. L. Krause, K. J. Schafer, and K. C. Kulander. High-order harmonic generation from atoms and ions in the high intensity regime. *Phys. Rev. Lett.*, **68**:3535, 1992.

[105] K. C. Kulander, K. J. Schafer, and J. L. Krause. Dynamics of short-pulse excitation, ionization and harmonic conversion. In *Super-Intense Laser-Atom Physics*. Plenum Press, New York, 1993.

[106] M. Lewenstein, P. Balcou, M. Ivanov, A. L'Huillier, and P. Corkum. Theory of high-order harmonic generation by low-frequency laser fields. *Phys. Rev. A*, 49:2117, 1994.

[107] G. Farkas and C. Tóth. Proposal for attosecond light pulse generation using laser induced multiple-harmonic conversion processes in rare gases. *Phys. Lett. A*, **168**:447, 1992.

[108] S. E. Harris, J. J. Macklin, and T. W. Hänsch. Atomic scale temporal structure inherent to high-order harmonic generation. *Opt. Commun.*, **100**:487, 1993.

[109] P. B. Corkum, N. H. Burnett, and M. Y. Ivanov. Subfemtosecond pulses. *Opt. Lett.*, 19:1870, 1994.

[110] P. M. Paul, E. Toma, P. Breger, G. Mullot, F. Augé, P. Balcou, H. Muller, and P. Agostini. Observation of a train of attosecond pulses from high harmonic generation. *Science*, 292(5522):1689–1692, 2001.

[111] M. Hentschel, R. Kienberger, C. Spielmann, G. A. Reider, N. Milosevic, T. Brabec, P. Corkum, U. Heinzmann, M. Drescher, and F. Krausz. Attosecond metrology. *Nature*, 414(6863):509–513, 2001.

[112] H. Wikmark, C. Guo, J. Vogelsang, P. W. Smorenburg, H. Coudert-Alteirac, J. Lahl, J. Peschel, P. Rudawski, H. Dacasa, S. Carlström, S. Maclot, M. B. Gaarde, P. Johnsson, C. L. Arnold, and A. L'Huillier. Spatiotemporal coupling of attosecond pulses. *Proceedings of the National Academy of Sciences*, 2019.

[113] K. Miyazaki and H. Takada. High-order harmonic generation in the tunneling regime. *Physical Review A*, 52(4):3007–3021, 1995.

[114] D. R. Austin and J. Biegert. Strong-field approximation for the wavelength scaling of high-harmonic generation. *Physical Review A*, 86:023813, 2012.

[115] C. Guo, A. Harth, S. Carlström, Y.-C. Cheng, S. Mikaelsson, E. Mårsell, C. Heyl, M. Miranda, M. Gisselbrecht, M. B. Gaarde, K. J. Schafer, A. Mikkelsen, J. Mauritsson, C. L. Arnold, and A. L'Huillier. Phase control of attosecond pulses in a train. *J. Phys. B: At., Mol. Opt. Phys.*, 51(3):034006, 2018.

[116] J. Samson and W. Stolte. Precision measurements of the total photoionization cross sections of he, ne, ar, kr, and xe. *Journal of Electron Spectroscopy and Related Phenomena*, pages 265–276, 2002.

[117] M. Ammosov, N. Delone, and V. Krainov. Tunnelling ionization of complex atoms and of atomic ions in an alternating electromagnetic field. *Sov. Phys. JETP*, 64(6):1191–1194, 1986.

[118] S. Kazamias, D. Douillet, F.Weihe, C. Valentin, A. Rousse, S. Sebban, G. Grillon, F. Augé, D. Hulin, and P. Balcou. Global Optimization of High Harmonic Generation. *Phys. Rev. Lett.*, 90:193901, 2003.

[119] M. B. Gaarde, J. L. Tate, and K. J. Schafer. Macroscopic aspects of attosecond pulse generation. *J. Phys. B*, 41:132001, 2008.

[120] C. M. Heyl, C. L. Arnold, A. Couairon, and A. L'Huillier. Introduction to macroscopic power scaling principles for high-order harmonic generation. *J. Phys. B: At., Mol. Opt. Phys.*, 50(1):013001, 2017.

[121] C. M. Heyl, H. Coudert-Alteirac, M. Miranda, M. Louisy, K. Kovacs, V. Tosa, E. Balogh, K. Varjú, A. L'Huillier, A. Couairon, and C. L. Arnold. Scale-invariant nonlinear optics in gases. *Optica*, 3(1):75–81, 2016.

[122] R. Weissenbilder, S. Carlström, L. Rego, C. Guo, C. M. Heyl, P. Smorenburg, E. Constant, C. L. Arnold, and A. L'Huillier. Efficient generation of high-order harmonics in gases, 2022.

[123] A. L. Cavalieri, N. Müller, T. Uphues, V. S. Yakovlev, A. Baltuška, B. Horvath, B. Schmidt, L. Blümel, R. Holzwarth, S. Hendel, M. Drescher, U. Kleineberg, P. M. Echenique, R. Kienberger, F. Krausz, and U. Heinzmann. Attosecond spectroscopy in condensed matter. *Nature*, 449:1029, 2007.

[124] M. Isinger, R. J. Squibb, D. Busto, S. Zhong, A. Harth, D. Kroon, S. Nandi, C. L. Arnold, M. Miranda, J. M. Dahlström, E. Lindroth, R. Feifel, M. Gisselbrecht, and A. L'Huillier. Photoionization in the time and frequency domain. *Science*, 358(6365):893–896, 2017.

[125] R. Kienberger, E. Goulielmakis, M. Uiberacker, A. Baltuška, V. Yakovlev, F. Bammer, A. Scrinzi, T. Westerwalbesloh, U. Kleineberg, U. Heinzmann, M. Drescher, and F. Krausz. Atomic transient recorder. *Nature*, 427:817, 2004.

[126] M. Lavollee. A new detector for measuring three-dimensional momenta of charged particles in coincidence. *Rev. Sci. Instrum.*, 70(7):2968–2974, 1999.

[127] A. Huetz and J. Mazeau. Double photoionization of helium down to 100 mev above threshold. *Phys. Rev. Lett.*, 85:530–533, 2000.

[128] M. Gisselbrecht, A. Huetz, M. Lavollée, T. J. Reddish, and D. P. Seccombe. Optimization of momentum imaging systems using electric and magnetic fields. *Review of Scientific Instruments*, 76(1):013105, 2005.

[129] J. Ullrich, R. Moshammer, A. Dorn, R. Dörner, L. P. H. Schmidt, and H. Schniidt-Böcking. Recoil-ion and electron momentum spectroscopy: reaction-microscopes. *Reports on Progress in Physics*, 66(9):1463–1545, 2003.

[130] R. Dorner, V. Mergel, O. Jagutzki, L. Spielberger, J. Ullrich, R. Moshammer, and H. Schmidt-Bocking. Cold Target Recoil Ion Momentum Spectroscopy: a 'momentum microscope' to view atomic collision dynamics. *Physics Reports*, 330:95–192, 2000.

[131] F. Quéré, Y. Mairesse, and J. Itatani. Temporal characterization of attosecond XUV fields. *J. Mod. Opt.*, 52:339, 2005.

[132] Y.-C. Cheng, S. Mikaelsson, S. Nandi, L. Rämisch, C. Guo, S. Carlström, A. Harth, J. Vogelsang, M. Miranda, C. Arnold, A. L'Huillier, and M. Gisselbrecht. Controlling photoionization using attosecond time-slit interferences. *Proceedings of the National Academy of Sciences*, 117:10727–10732, 2020.

[133] A. Schiffrin, T. Paasch-Colberg, N. Karpowicz, V. Apalkov, D. Gerster, S. Mühlbrandt, M. Korbman, J. Reichert, M. Schultze, S. Holzner, J. V. Barth, R. Kienberger, R. Ernstorfer, V. S. Yakovlev, M. I. Stockman, and F. Krausz. Optical-field-induced current in dielectrics. *Nature*, 493(7430):70–74, 2013.

[134] O. Kwon, T. Paasch-Colberg, V. Apalkov, B.-K. Kim, J.-J. Kim, M. I. Stockman, and D. Kim. Semimetallization of dielectrics in strong optical fields. *Scientific Reports*, 6(1):21272–, 2016.

[135] O. Kwon and D. Kim. Phz current switching in calcium fluoride single crystal. *Appl. Phys. Lett.*, 108(19):191112–, 2016.

[136] T. Paasch-Colberg, S. Y. Kruchinin, O. Saglam, S. Kapser, S. Cabrini, S. Muehlbrandt, J. Reichert, J. V. Barth, R. Ernstorfer, R. Kienberger, V. S. Yakovlev, N. Karpowicz, and A. Schiffrin. Sub-cycle optical control of current in a semiconductor: from the multiphoton to the tunneling regime. *Optica*, 3(12):1358–1361, 2016.

[137] J. B. Khurgin. Optically induced currents in dielectrics and semiconductors as a nonlinear optical effect. *J. Opt. Soc. Am. B*, 33(7):C1–C9, 2016.

[138] L. Lavenu, M. Natile, F. Guichard, X. Délen, M. Hanna, Y. Zaouter, and P. Georges. High-power two-cycle ultrafast source based on hybrid nonlinear compression. *Opt. Express*, 27(3):1958–1967, 2019.

[139] G. Barbiero, H. Wang, M. Graßl, S. Gröbmeyer, D. Kimbaras, M. Neuhaus, V. Pervak, T. Nubbemeyer, H. Fattahi, and M. F. Kling. Efficient nonlinear compression of a thin-disk oscillator to 8.5 fs at 55 W average power. *Opt. Lett.*, 46(21):5304–5307, 2021.

[140] M. Müller, J. Buldt, H. Stark, C. Grebing, and J. Limpert. Multipass cell for high-power few-cycle compression. *Opt. Lett.*, 46(11):2678–2681, 2021.

[141] S. B. Mirov, I. S. Moskalev, S. Vasilyev, V. Smolski, V. V. Fedorov, D. Martyshkin, J. Peppers, M. Mirov, A. Dergachev, and V. Gapontsev. Frontiers of mid-ir lasers based on transition metal doped chalcogenides. *IEEE Journal of Selected Topics in Quantum Electronics*, 24(5):1–29, Sept.-Oct. 2018.

[142] V. E. Leshchenko, B. K. Talbert, Y. H. Lai, S. Li, Y. Tang, S. J. Hageman, G. Smith, P. Agostini, L. F. DiMauro, and C. I. Blaga. High-power few-cycle Cr:ZnSe mid-infrared source for attosecond soft x-ray physics. *Optica*, 7(8):981–988, 2020.

[143] C. Gaida, M. Gebhardt, T. Heuermann, F. Stutzki, C. Jauregui, and J. Limpert. Ultrafast thulium fiber laser system emitting more than 1 kW of average power. *Opt. Lett.*, 43(23):5853–5856, 2018.

[144] P. Gierschke, C. Grebing, M. Abdelaal, M. Lenski, J. Buldt, Z. Wang, T. Heuermann, M. Mueller, M. Gebhardt, J. Rothhardt, and J. Limpert. Nonlinear pulse compression to 51-W average power GW-class 35-fs pulses at 2-µm wavelength in a gas-filled multi-pass cell. *Opt. Lett.*, 47(14):3511–3514, 2022.

[145] M. Gebhardt, T. Heuermann, R. Klas, C. Liu, A. Kirsche, M. Lenski, Z. Wang, C. Gaida, J. E. Antonio-Lopez, A. Schülzgen, R. Amezcua-Correa, J. Rothhardt, and J. Limpert. Bright, high-repetition-rate water window soft x-ray source enabled by nonlinear pulse self-compression in an antiresonant hollow-core fibre. *Light: Science & Applications*, 10(1):36–, 2021.

[146] N. C. Geib, R. Hollinger, E. Haddad, P. Herrmann, F. Légaré, T. Pertsch, C. Spielmann, M. Zürch, and F. Eilenberger. Discrete dispersion scan setup for measuring few-cycle laser pulses in the mid-infrared. *Opt. Lett.*, 45(18):5295–5298, 2020.

[147] F. Nicolai, N. Müller, C. Manzoni, G. Cerullo, and T. Buckup. Acousto-optic modulator based dispersion scan for phase characterization and shaping of femtosecond mid-infrared pulses. *Opt. Express*, 29(13):20970–20980, 2021.

[148] S. Ghimire, A. D. DiChiara, E. Sistrunk, P. Agostini, L. F. DiMauro, and D. A. Reis. Observation of high-order harmonic generation in a bulk crystal. *Nature Physics*, 7(2):138–141, 2010.

[149] G. Hergert, A. Wöste, J. Vogelsang, T. Quenzel, D. Wang, P. Groß, and C. Lienau. Probing transient localized electromagnetic fields using low-energy point-projection electron microscopy. *ACS Photonics*, 8(9):2573–2580, 2021.

[150] Y. Mairesse and F. Quéré. Frequency-resolved optical gating for complete reconstruction of attosecond bursts. *Phys. Rev. A*, 71:011401(R), 2005.

[151] P. D. Keathley, S. Bhardwaj, J. Moses, G. Laurent, and F. X. Kärtner. Volkov transform generalized projection algorithm for attosecond pulse characterization. *New Journal of Physics*, 18(7):073009–, 2016.

[152] C. Heide, T. Boolakee, T. Eckstein, and P. Hommelhoff. Optical current generation in graphene: CEP control vs. w + 2w control. *Nanophotonics*, 10(14):3701–3707, 2021.

[153] V. Hanus, V. Csajbók, Z. Pápa, J. Budai, Z. Márton, G. Z. Kiss, P. Sándor, P. Paul, A. Szeghalmi, Z. Wang, B. Bergues, M. F. Kling, G. Molnár, J. Volk, and P. Dombi. Light-field-driven current control in solids with pJ-level laser pulses at 80 MHz repetition rate. *Optica*, 8(4):570–576, 2021.

Printed by Media-Tryck, Lund 2022 NORDIC SWAN ECOLABEL 3041 0903

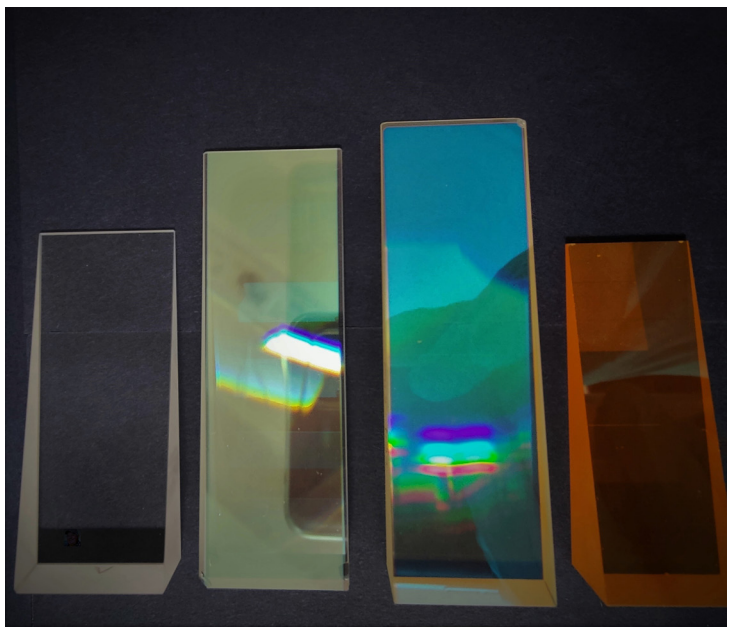

LUND UNIVERSITY
Faculty of Engineering, LTH
Department of Physics
Division of Atomic Physics

ISBN 978-91-8039-315-7
ISSN 0281-2762
Lund Reports on Atomic Physics, LRAP 585 (2022)